Separate Effects of Surface Roughness, Wettability and Porosity on Boiling Heat Transfer and Critical Heat Flux and Optimization of Boiling Surfaces

by

Harrison Fagan O'Hanley

SUBMITTED TO THE DEPARTMENT OF MECHANICAL ENGINEERING
AND THE DEPARTMENT OF NUCLEAR SCIENCE AND ENGINEERING
IN PARTIAL FULFILLMENT OF THE REQUIREMENTS FOR THE DEGREES OF
BACHELOR OF SCIENCE IN MECHANICAL ENGINEERING
AND MASTER OF SCIENCE IN NUCLEAR SCIENCE AND ENGINEERING
AT THE
MASSACHUSETTS INSTITUTE OF TECHNOLOGY
JUNE 2012

Signature of Author

Department of Mechanical Engineering
Department of Nuclear Science and Engineering
May 11, 2012

Certified by

Jacopo Buongiorno
Associate Professor of Nuclear Science and Engineering
Thesis Supervisor

Certified by

Michael Rubner
Professor/Director of Center for Materials Science and Engineering
Thesis Supervisor

Certified by

Robert Cohen
St.Laurent Professor of Chemical Engineering
Thesis Supervisor

Certified by

Lin-Wen Hu
Associate Director, MIT Nuclear Reactor Laboratory
Thesis Supervisor

Certified by

Thomas McKrell
Research Scientist for Nuclear Science and Engineering
Thesis Supervisor

Accepted by

Mujid S. Kazimi
TEPCO Professor of Nuclear Engineering
Chair, Department Committee on Graduate Students

Accepted by

John H. Lienhard V
Samuel C. Collins Professor of Mechanical Engineering
Undergraduate Officer

Separate Effects of Surface Roughness, Wettability and Porosity on Boiling Heat Transfer and Critical Heat Flux and Optimization of Boiling Surfaces

by

Harrison Fagan O'Hanley

Submitted to the Department of Mechanical Engineering
and the Department of Nuclear Science and Engineering
on May 11, 2012, in partial fulfillment of the
requirements for the degrees of
Bachelor of Science in Mechanical Engineering
and
Master of Science in Nuclear Science and Engineering

Abstract

The separate effects of surface wettability, porosity, and roughness on critical heat flux (CHF) and heat transfer coefficient (HTC) were examined using carefully-engineered surfaces. All test surfaces were prepared on nanosmooth indium tin oxide - sapphire heaters and tested in a pool boiling facility in MIT's Reactor Thermal Hydraulics Laboratory. Roughness was controlled through fabrication of micro-posts of diameter $20\mu m$ and height $15\mu m$; intrinsic wettability was controlled through deposition of thin compact coatings made of hydrophilic SiO_2 (typically, $20nm$ thick) and hydrophobic fluorosilane (monolayer thickness); porosity and pore size were controlled through deposition of layer-by-layer coatings made of SiO_2 nanoparticles. The ranges explored were: $0 - 15\mu$ for roughness (Rz), $0 - 135$ degrees for intrinsic wettability, and $0 - 50\%$ and $50nm$ for porosity and pore size, respectively. During testing, the active heaters were imaged with an infrared camera to map the surface temperature profile and locate distinct nucleation sites. It was determined that wettability can play a large role on a porous surface, but has a limited effect on a smooth non-porous surface. Porosity had very pronounced effects on CHF. When coupled with hydrophilicity, a porous structure enhanced CHF by approximately $50\% - 60\%$. However, when combined with a hydrophobic surface, porosity resulted in a reduction of CHF by 97% with respect to the reference surface. Surface roughness did not have an appreciable effect, regardless of the other surface parameters present. Hydrophilic porous surfaces realized a slight HTC enhancement, while the HTC of hydrophobic porous surfaces was greatly reduced. Roughness had little effect on HTC. A second investigation used spot patterning aimed at creating a surface with optimal characteristics for both CHF and HTC. Hydrophobic spots (meant to be preferential nucleation sites) were patterned on a porous hydrophilic surface. The spots indeed were activated as nucleation sites, as recognized via the IR signal. However, CHF and HTC were not enhanced by the spots. In some instances, CHF was actually decreased by the spots, when compared to a homogenous porous hydrophilic surface.

Thesis Supervisor: Jacopo Buongiorno
Title: Associate Professor of Nuclear Science and Engineering

Thesis Supervisor: Michael Rubner
Title: Professor/Director of Center for Materials Science and Engineering

Thesis Supervisor: Robert Cohen
Title: St.Laurent Professor of Chemical Engineering

Thesis Supervisor: Lin-Wen Hu
Title: Associate Director, MIT Nuclear Reactor Laboratory

Thesis Supervisor: Thomas McKrell
Title: Research Scientist for Nuclear Science and Engineering

Acknowledgments

I would first like to thank Professor Jacopo Buongiorno for his guidance and support through this project and others. Since joining his group during my Junior year, I've gained an intricate understanding of thermal hydraulics and acquired a technical and experimental skill set that will serve me through the length of my engineering career. It has been a joy to apply the knowledge gained from my engineering curriculum to pertinent research. Thank you for this tremendous opportunity.

Thank you Dr. Lin Wen Hu for your support and input over the last three years. Your experimental insight has served me on numerous projects and is very much appreciated.

Through countless experiments and the ever-present setbacks, Dr. Thomas McKrell has helped me to develop and execute my tests. Thank for the immense help you provided me in performing my day to day experiments. Moreover, you're technical input on the project was invaluable and your company in the Green Lab was always appreciated.

Thank you Professors Michael Rubner and Robert Cohen. Your cumulative insight into surface nanoengineering enabled the fabrication of the surfaces required for this investigation. Thank you for opening your labs to me and providing guidance along the way.

Thank you Professor Vladimir Bulovic for allowing the use of his lab for heater fabrication.

The MIT Microsystems Technology Laboratory provided much of the equipment required for heater fabrication. In this facility, Kurt Broderick provided the technical knowledge and assistance needed to efficiently and adequately fabricate the necessary features. Thank you for all the time you devoted to helping me.

During my research, numerous other students have offered much appreciated and important help to me. Thank you Jonathan Gilbert for your assistance with the layer by layer deposition process. Hyomin Lee offered keen insight into surface chemical engineering and with lab equipment training. Members of my research group were always valued resources in solving problems during research. Thank you very much Eric Forrest, Vivek Sharma, Rosie Sugrue, Bao Truong and Reza Azizian. Lastly, Bren Phillips served as a truly invaluable mentor for this project. Bren helped me to overcome numerous experimental problems and was always a willing and helpful resource. You're efforts will always be appreciated.

Thank you Carolyn Coyle for your help in running the pool boiling tests. I wish you good luck as you continue this work in the future.

I would like to extend a sincere thank you and my appreciation to the Department of Nuclear Science and Engineering for providing me with the opportunity to carry out this research and develop myself as an engineer.

Additionally, thank you to everyone at Areva for the support of this project and your insight and guidance along the way.

Finally, thank you Mom, Dad, Allie, Gram and Pappy for helping me to get here. To just list everything you all have done to support me over the years would require another entire thesis.

Contents

1 Introduction **17**

1.1 Motivation 17

1.2 Objective 19

2 Background and Prior Research **21**

2.1 Nucleation Theory 21

2.1.1 Bubble Nucleation 21

2.1.2 Bubble Growth 23

2.1.3 Bubble Departure Diameter 25

2.1.4 Bubble Frequency 27

2.1.5 Bubble Coalescence 28

2.2 Surface Characteristics 29

2.2.1 Roughness 29

2.2.2 Porosity 31

2.2.3 Wettability 32

2.3 Pool Boiling Heat Transfer and Critical Heat Flux 33

2.3.1 Pool Boiling Overview 33

2.3.2 Critical Heat Flux 35

2.4 Surface Engineering 38

2.4.1 Surface Roughness and Porosity 39

2.4.2 Nanofluids 40

2.4.3 Surface Chemistry 41

2.5 Conclusions from Prior Research 42

3 Test Matrix **45**

3.1 Separate Effect Investigation 45

3.1.1 Roughness 45

3.1.2 Porosity 46

3.1.3 Wettability 46

3.1.4 Overall Separate Effect Test Matrix 47

3.2 Spot Patterning for Heater Optimization 48

4 Experimental Methods **51**

4.1 ITO-Sapphire Heaters 52

4.2 Surface Fabrication 53

4.2.1 Layer by Layer Deposition 53

4.2.2 Chemical Vapor Deposition of Fluorosilane 57

4.2.3 Ultraviolet Ozone Patterning 58

4.2.4 Electron Beam Physical Vapor Deposition 61

4.2.5 Photolithography 62

4.3 Feature Verification 64

4.3.1 High Resolution Scanning Electron Microscope 64

4.3.2 Contact Angle Measurement 65

4.3.3 Stylus Contact Profilometer 66

4.3.4 Spectroscopic Ellipsometer for Porosity Measurement 67

4.4 Heater Testing 67

4.4.1 Heater Preparation 67

4.4.2 Pool Boiling Facility 68

4.5 Data Reduction 72

4.5.1 IR Signal Calibration 72

4.5.2 IR Signal Analysis 72

4.6 Uncertainty Analysis 74

5 Separate Effect Investigation Preparation, Testing, and Results **77**

5.1 Uncoated Sapphire Surface 79

5.1.1 Surface Analysis 79
5.1.2 PBF Testing and Discussion 81
5.2 Smooth Non-porous Hydrophilic Surface 82
5.2.1 Surface Fabrication 82
5.2.2 Surface Analysis 82
5.2.3 PBF Testing and Discussion 84
5.3 Smooth Non-Porous Hydrophobic Surface 85
5.3.1 Surface Fabrication 85
5.3.2 Surface Analysis 86
5.3.3 PBF Testing and Discussion 88
5.4 Smooth Porous Hydrophilic Surface 89
5.4.1 Surface Fabrication 89
5.4.2 Surface Analysis 90
5.4.3 PBF Testing and Discussion 93
5.5 Smooth Porous Hydrophobic Surface 94
5.5.1 Surface Fabrication 94
5.5.2 Surface Analysis 95
5.5.3 PBF Testing and Discussion 97
5.6 Rough Non-porous Hydrophilic Surface 100
5.6.1 Surface Fabrication 100
5.6.2 Surface Analysis 101
5.6.3 PBF Testing and Discussion 104
5.7 Modified Rough Non-porous Hydrophilic Surface 105
5.7.1 Surface Fabrication 105
5.7.2 PBF Testing and Discussion 105
5.8 Rough Non-porous Hydrophobic Surface 106
5.8.1 Surface Fabrication 106
5.8.2 Surface Analysis 107
5.8.3 PBF Testing and Discussion 109
5.9 Rough Porous Hydrophilic Surface 111

5.9.1 Surface Fabrication 111
5.9.2 Surface Analysis 111
5.9.3 PBF Testing and Discussion 112
5.10 Rough Porous Hydrophobic Surface 114
5.10.1 Surface Fabrication 114
5.10.2 Surface Analysis 114
5.10.3 PBF Testing and Discussion 117
5.11 Surface Parameter Comparisons 123
5.11.1 Effect of Wettability 123
5.11.2 Effect of Porosity 126
5.11.3 Effect of Roughness 132
5.12 Summary and Future Recommendations 135

6 Spot Patterning Heater Preparation, Testing, and Results 137
6.1 Surface Preparation 137
6.2 Surface Analysis 138
6.3 PBF Test Results 138
6.3.1 Effect of Varying Spot Pitch (Patterns A-D) 140
6.3.2 Effect of Varying Spot Size and Dimension Ratio (Patterns E-H) . . . 149
6.4 Summary and Future Recommendations 153

7 Conclusion 155

List of Figures

2-1 Nucleation cavity. 22

2-2 Contact angle. 22

2-3 Mikic equation plot. 24

2-4 Fritz equation plot. 26

2-5 Unidirectional surface roughness and waviness. 29

2-6 Arithmetic average roughness (R_a). 30

2-7 R_z surface roughness. 31

2-8 Cassie and Wenzel wettability regimes. 33

2-9 Characteristic pool boiling curve. 34

2-10 Kandlikar CHF model plot. 37

2-11 Polezhaev CHF model plot. 38

4-1 ITO-Sapphire Heater (all dimensions in millimeters). 52

4-2 Zeiss HMS Programmable Slide Stainer. 54

4-3 LBL process flow. 55

4-4 Harrick Plasma Plasmaflow. 57

4-5 UVO mask Patterns A-D. 59

4-6 UVO mask Patterns E-H. 60

4-7 UVO Mask and Heater Interface. 61

4-8 Sloan 8kV Electron Beam Evaporator. 62

4-9 JEOL NeoScope JCM-5000 SEM 65

4-10 KSV Instruments CAM 101 used for making contact angle measurements. . . 66

4-11 Electrical leads attached to ITO-sapphire heater. 69

4-12 PBF layout. 70
4-13 PBF with IR camera setup. 70
4-14 Thermal circuit accounting for conduction through sapphire substrate. . . . 74

5-1 Uncoated Sapphire Heater Plots 81
5-2 Static contact angle measurement for Smooth Non-porous Hydrophilic surface. 83
5-3 Smooth Non-porous Hydrophilic Plots 84
5-4 Contact angle measurements for Smooth Non-porous Hydrophobic surface. . 87
5-5 Smooth Non-porous Hydrophobic Plots 89
5-6 Static contact angle measurement for Smooth Porous Hydrophilic surface. . . 90
5-7 SEM images of Smooth Porous Hydrophilic heater 92
5-8 Smooth Porous Hydrophilic Plots 93
5-9 Contact angle measurements for Porous Hydrophobic heater. 96
5-10 Smooth Porous Hydrophobic Plots 98
5-11 Surface temperature progression of porous hydrophilic heater. 99
5-12 Annealed ITO 100
5-13 Static contact angle measurements for Rough Non-porous Hydrophilic surface. 102
5-14 Surface profile for Rough Non-porous Hydrophilic heater. 103
5-15 SEM images of post features. 103
5-16 Rough Non-porous Hydrophilic Plots 104
5-17 Modified Rough Non-porous Hydrophilic Plots 106
5-18 Contact angle measurements for Rough Non-porous Hydrophobic surface. . . 108
5-19 Optical microscope images of Rough Non-porous Hydrophobic heater. 108
5-20 Rough Non-porous Hydrophobic Plots 110
5-21 Contact angle measurements for Rough Porous Hydrophilic surface. 112
5-22 SEM image of SiO_2 multilayers conforming to post feature on surface. 113
5-23 Rough Porous Hydrophilic Plots 113
5-24 Contact angle measurements for Rough Porous Hydrophobic surface. 115
5-25 Rough Porous Hydrophobic Plots 116
5-26 Surface temperature progression of Rough Porous Hydrophobic 1 heater. . . 119

5-27 Surface temperature progression of Rough Porous Hydrophobic 2 heater. . . 120
5-28 Vapor cushion growth on Rough Porous Hydrophobic 2 heater at $700\frac{kW}{m^2}$ . . 121
5-29 Surface temperature progression of Rough Porous Hydrophobic 3 heater. . . 122
5-30 Vapor cushion growth on Rough Porous Hydrophobic 3 heater at $359\frac{kW}{m^2}$. . . 123
5-31 Wettability comparison plots: Smooth, Non-porous heaters 124
5-32 Wettability comparison plots: Rough, Non-porous heaters 125
5-33 Wettability comparison plots: Smooth, Porous heaters 127
5-34 Wettability comparison plots: Rough, Porous heaters 128
5-35 Porosity comparison plots: Smooth, Hydrophilic heaters 129
5-36 Porosity comparison plots: Rough, Hydrophilic heaters 129
5-37 Porosity comparison plots: Smooth, Hydrophobic heaters 130
5-38 Porosity comparison plots: Rough, Hydrophobic heaters 131
5-39 Roughness comparison plots: Non-porous, Hydrophilic heaters 132
5-40 Roughness comparison plots: Non-porous, Hydrophobic heaters 133
5-41 Roughness comparison plots: Porous, Hydrophilic heaters 133
5-42 Roughness comparison plots: Porous, Hydrophobic heaters 134

6-1 Uncoated Sapphire and Smooth Porous Hydrophilic plots. 139
6-2 Spot pattern visible at $1554kW/m^2$. 143
6-3 Boiling Curve and Heat Transfer Coefficient for Patterns A-D 144
6-4 Pattern A ($260\mu m$ spot, $0.5mm$ pitch) plots. 145
6-5 Pattern B ($260\mu m$ spot, $0.75mm$ pitch) plots. 145
6-6 Pattern C ($260\mu m$ spot, $1.25mm$ pitch) plots 146
6-7 Pattern D ($260\mu m$ spot, $1.5mm$ pitch) plots. 146
6-8 Boiling Curve and Heat Transfer Coefficient for Patterns E-H. 151
6-9 Pattern E ($90\mu m$ diameter, $0.2mm$ pitch) plots. 151
6-10 Pattern F ($120\mu m$ diameter, $0.75mm$ pitch) plots. 152
6-11 Pattern G ($120\mu m$ diameter, $2mm$ pitch) plots. 152
6-12 Pattern H ($120\mu m$ diameter, $0.2mm$ pitch) plots. 153

List of Tables

3.1 Smooth and Rough heater surface roughness characteristics. 45
3.2 Separate Effect investigation test matrix. 48
3.3 Spot Pattern Test Matrix. 49

4.1 Negative LBL Solution: 0.3wt% SiO_2 nanoparticles of pH 9.0. 54
4.2 Positive LBL Solution: PAH of pH 7.5. 55
4.3 Characteristic heating steps. 71

5.1 Separate Effect investigation CHF values. 78
5.2 Measured surface parameters on fabricated heaters. 79
5.3 Contact angle measurements for Uncoated Sapphire heater. 80
5.4 Roughness measurements for Uncoated Sapphire heater. 80
5.5 CHF Values for Uncoated Sapphire heaters. 81
5.6 Contact angle measurements for Smooth Non-porous Hydrophilic heater. . . 83
5.7 Roughness measurements for Smooth Non-porous Hydrophilic heater. 83
5.8 CHF values for Smooth Non-porous Hydrophilic heaters. 84
5.9 Contact angle measurements for Smooth Non-porous Hydrophobic heater. . . 87
5.10 Roughness measurements for Smooth Non-porous Hydrophobic heater. . . . 88
5.11 CHF Values for Smooth Non-porous Hydrophobic heaters. 88
5.12 Contact angle measurements for Smooth Porous Hydrophilic surface. 90
5.13 Porosity characterization of Smooth Porous Hydrophilic surface. 91
5.14 Confocal roughness measurements of Smooth Porous Hydrophilic heater. . . 91
5.15 Profilometer roughness measurements for Smooth Porous Hydrophilic heater. 92
5.16 CHF values for Smooth Porous Hydrophilic heater. 92

5.17 Effect of porous structure particle size on CHF. 94
5.18 Contact angle measurements for Smooth Porous Hydrophobic heater. 96
5.19 Roughness measurements for Smooth Porous Hydrophobic heater. 97
5.20 CHF and Burnout values for Smooth Porous Hydrophobic heaters. 97
5.21 Contact angle measurements for Rough Non-porous Hydrophilic heater. . . . 101
5.22 Roughness measurements for Rough Non-porous Hydrophilic heater. 102
5.23 CHF values for Rough Non-porous Hydrophilic heaters. 104
5.24 CHF values for Modified Rough Non-porous Hydrophilic heaters. 105
5.25 Contact angle measurements for Rough Non-porous Hydrophobic heater. . . 107
5.26 Roughness measurements of Rough Non-porous Hydrophobic surface. 109
5.27 CHF values for Rough Non-porous Hydrophobic heaters. 109
5.28 Contact angle measurements for Rough Porous Hydrophilic heater. 111
5.29 Roughness measurements for Rough Porous Hydrophilic heater. 112
5.30 CHF values for Rough Porous Hydrophilic surface heaters. 112
5.31 Contact angle measurements for Porous Rough Hydrophobic heater. 115
5.32 Roughness measurements for Rough Porous Hydrophobic heater. 116
5.33 CHF and heater burnout values for Rough Porous Hydrophobic heaters. . . . 116

6.1 Contact angle measurements for spot patterned heaters. 138
6.2 Uncoated sapphire heater and smooth porous hydrophilic reference CHF values. 140
6.3 CHF Values for Patterns A-D. 141
6.4 Theoretical number of nucleation sites for various pitches employed. 142
6.5 Bubble departure diameter to intersite spacing ratios for Patterns A-D. . . . 147
6.6 CHF Values for Patterns E-H. 150

Chapter 1

Introduction

1.1 Motivation

Boiling is a common energy transfer mechanism. Examples of boiling systems can be found in a variety of industries, including nuclear and non-nuclear power generation. Typically, heat is transferred from a source through a surface to a working fluid. The behavior of the liquid at the surface-liquid interface characterizes the system's capability to transfer heat energy. Thus, it is highly desirable to engineer the heat transfer surface to promote efficient boiling and specifically nucleate boiling heat transfer.

While there are many characteristics of a boiling system, two properties are of specific interest: the critical heat flux (CHF) and the heat transfer coefficient (HTC). CHF occurs at the transition from the nucleate boiling regime to the film boiling regime. This shift results in a dramatic reduction in heat flux, causing a rapid increase in surface temperature. This is problematic because increased temperatures can weaken a material by lowering its yield strength and also induce accelerated corrosion. [1] Achievement of CHF often leads to catastrophic failure and thus a thermal hydraulic system must be maintained below this threshold. The HTC characterizes the system's ability to transfer heat by relating heat flux to the temperature difference between the surface and the bulk liquid. Both of these parameters dictate a heat transfer system's capacity and performance.

While these parameters are integral to the function of thermal hydraulic systems, there are still many gaps in the engineering community's understanding of the triggering of CHF

and control of HTC. In many instances, optimization of CHF has largely been a trial and error process. This is primarily a result of the markedly complex nature of the CHF and overall boiling phenomena, where minuscule changes in surface properties or operating conditions can have profound consequences. As a result, there is a need to investigate the effects that individual surface parameters - such as wettability, roughness, and porosity - have on a system's CHF and HTC. Through this characterization, researchers will be better positioned to engineer and optimize boiling surfaces.

Building upon the individual parameter characterization, it is possible to design of nano-scale feature patterns to enhance CHF and HTC. Throughout the twentieth century, a variety of methods were explored for machining and treating transfer surfaces to enhance boiling. Recent boiling optimization techniques have included physical machining, thin film deposition and chemical treatments. Additionally, numerous boiling enhancement technologies have found success in large scale industry applications.

Through this long history of surface engineering for boiling enhancement, the validity of the approach can be inferred. The engineering community has made great strides in controlling the boiling phenomenon. Currently, however, the advent of micro- and nano-scale fabrication techniques - many of which are borrowed from the electronics sector - opens new room for innovation in creating surface patterns to enhance CHF and HTC. Features can be created on a scale more closely to that which is found in nature and exotic patterns can be pursued. Through the use of a variety of nanoengineering techniques, it is possible to control boiling heat transfer in increasingly precise and optimal manners.

The ubiquity of boiling heat transfer systems across numerous industries and engineering applications warrants both the separate effects investigation and surface optimization. The former portion of this project will provide an initial understanding of how specific surface properties affect boiling. This knowledge will provide subsequent researchers with the tools necessary to exploit such parameters in the optimal design of thermal hydraulic systems. Likewise, the latter part of this investigation draws upon the separate effect characterization and serves to further the exploration of the nanoengineering techniques for surface heater optimization.

1.2 Objective

This investigation seeks to better understand the CHF phenomenon and use this knowledge to develop nanoengineered heaters with optimized CHF and heat transfer characteristics. This overall objective is accomplished by:

1. Characterizing the individual effects of surface roughness, wettability, and porosity on CHF and HTC.

2. Using nanoengineered surface feature patterns to enhance both CHF and HTC. These patterns predominantly consist of porous hydrophobic spots of varying diameter, patterned on different pitches. The background surface is nominally porous hydrophilic.

Chapter 2

Background and Prior Research

It is important to first consider the mechanisms by which boiling occurs. The processes of bubble nucleation, growth, and departure all affect the amount of heat than can be removed from a surface. Surface characteristics such as roughness, porosity, and wettability all are thought to affect the nucleation site density, bubble growth rate, departure diameter and frequency, thus ultimately determining the performance of a boiling surface. An understanding of how these parameters are characterized is required before they can be controlled in boiling experiments. Finally, pool boiling itself as an integral phenomenon must be reviewed. Here, numerous correlations for predicting boiling behavior are presented. There are countless other equations to characterize boiling that can be readily found in literature; however, the correlations selected here are believed to give an adequate overview of the relevant trends. Please note, that the nomenclature for all equations presented here is consistent. Variables are introduced at their first appearance.

2.1 Nucleation Theory

2.1.1 Bubble Nucleation

Nucleation is where boiling heat transfer begins and is the process of vapor bubble formation. Bubble nucleation can occur both in the bulk liquid - known as Homogeneous Nucleation - or at the interface between a liquid and the surfaces that contain it - known as Heterogeneous

Nucleation. However, as homogeneous nucleation requires substantial superheat, heterogeneous nucleation is most commonly encountered at lower superheats. [1] Moreover, as this investigation focuses on how boiling is affected by surface conditions, heterogeneous nucleation is the relevant mode of nucleation here. Typically, heterogeneous nucleation occurs in small cavities on the surface, with a characteristic dimension of $0.1\mu m$ to $10\mu m$. [1] Here, vapor is trapped and serves to initiate bubble formation, as seen in Figure 2-1. Because the bubble nucleation process is seeded by stored vapor or air in the cavities, heterogeneous nucleation requires only a few degrees of superheat before the onset of nucleate boiling. [2]

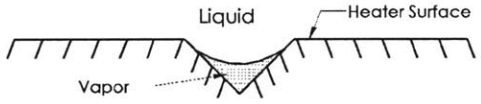

Figure 2-1: Nucleation cavity.

Heterogeneous bubble nucleation can also occur on a smooth surface, in the absence of a cavity. In such a scenario, the energy required for nucleation becomes a function of the contact angle of the liquid on the surface. Contact angle, Θ, is depicted in Figure 2-2. This angle is a function of a surface's wettability and low contact angle corresponds to a high wettability.

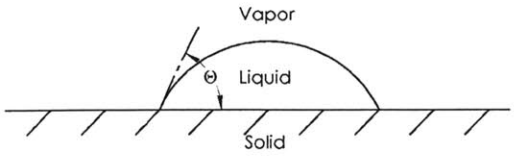

Figure 2-2: Contact angle.

The manner in which water wets a surface is a result of the intrinsic chemical surface chemistry, but also depends on roughness and porosity. Moreover, surface wettability has

complex effects on the heat transfer system. A high wettability can promote the rewetting of the surface, thus delaying CHF. However, higher wettability can also deactivate nucleation sites and consequently decrease the overall heat transfer coefficient. [1,3]

2.1.2 Bubble Growth

Following nucleation, a bubble goes through two different stages of growth: inertia controlled and heat transfer controlled. Inertia controlled growth occurs first and is limited by how quickly the bubble can displace the surrounding liquid. [4] During this period, the bubble radius increases roughly linearly as predicted by *Rayleigh (1917)* [5]:

$$r(t) = \left[\frac{2}{3}\left[\frac{T_f - T_{sat}(P_f)}{T_{sat}(P_f)}\right]\left[\frac{h_{fg}\rho_g}{\rho_f}\right]\right]^{\frac{1}{2}} t \tag{2.1}$$

Where, $r(t)$ is the time dependent bubble radius, T_f is the liquid temperature, $T_{sat}(P_f)$ is the saturation temperature at the corresponding liquid pressure, h_{fg} is the latent heat of vaporization, t is time, and ρ_g and ρ_f are the vapor and liquid densities, respectively. [2]

Heat transfer controlled growth occurs later, when the liquid superheat near the surface has been largely exhausted. In this regime, bubble growth is limited by heat transfer at the vaporization interface. [2,6] Here, bubble radius varies with square root of time, as modeled by *Plesset and Zwick (1954)* [7]:

$$r(t) = \frac{2\Delta T_{sat}(P_f)k_f}{h_{fg}\rho_g}\left[\frac{3t}{\pi\alpha_f}\right]^{\frac{1}{2}} \tag{2.2}$$

Where, k_f is the liquid phase thermal conductivity and α_f is the liquid phase thermal diffusivity.

Mikic et al. (1970) created a model that spans both bubble growth regimes. Here, bubble radius and time are non-dimensionalized, with growth predicted as,

$$r^+ = \frac{2}{3}[(t^+ + 1)^{\frac{3}{2}} - (t^+)^{\frac{3}{2}} - 1] \tag{2.3a}$$

$$r^+ = \frac{r(t)A}{B^2} \tag{2.3b}$$

$$t^+ = \frac{tA^2}{B^2} \tag{2.3c}$$

$$A = \left[\frac{2[T_f - T_{sat}(P_f)]h_{fg}\rho_g}{\rho_f T_{sat}(P_f)}\right]^{\frac{1}{2}} \tag{2.3d}$$

$$B = [\frac{12\alpha_f}{\pi}]^{\frac{1}{2}}[\frac{[T_f - T_{sat}(P_f)]h_{fg}c_{p,f}}{\rho_g h_{fg}}] \tag{2.3e}$$

Where, r^+ is non-dimensional bubble radius, t^+ is non-dimensional time, $c_{p,l}$ is the liquid specific heat capacity. [8] Bubble growth rate can be visualized from the Mikic equation presented in Figure 2-3. For $t^+ << 1$ the Mikic curve approaches the Rayleigh curve, while for $t^+ >> 1$ it approaches the Plesset curve.

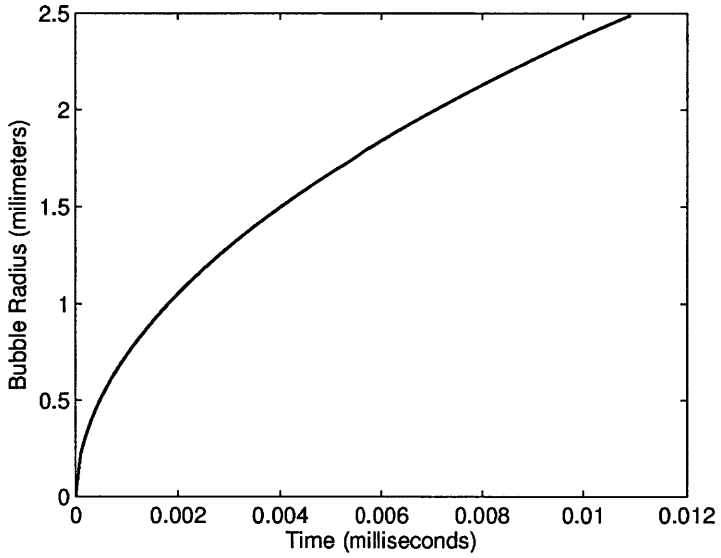

Figure 2-3: Mikic equation for bubble radius growth. Calculated for water at $1atm$ and a $10°C$ superheat.

The Mikic equation provides insight into the behavior of the vapor bubble as it grows on the heat transfer surface. As surface features are designed and spaced on the heater surface, it is important to understand which growth regime the bubble will be in when such features are encountered.

Understanding the bubble growth dynamics in these regimes is important for optimizing surface features to exploit the differences in growth dynamics. As bubbles continually grow

and depart from the surface, an ebullition is established. This process can best be understood through the following steps [2]:

1. As a bubble departs, it removes the surrounding thermal boundary layer. Therefore, the bulk fluid comes into contact with the heater surface.

2. A new thermal boundary layer begins to grow and during this time there is no appreciable bubble growth. This is known as the waiting period.

3. Following the waiting period, when the temperature at the nucleation site reaches the critical superheat required for nucleation of a new bubble, there is a rapid period of inertia controlled bubble growth.

4. The growth rate decreases and bubble growth becomes governed by heat transfer.

5. The bubble departs the surface and the cycle is restarted.

2.1.3 Bubble Departure Diameter

An understanding of the bubble's diameter when it leaves the surface is important for the design of surface features and specifically their relative spacing. As one might expect, the relationship between the size of the bubble and the size of a given surface feature can dramatically affect their interaction. *Fritz (1935)* proposed a correlation for the departure diameter as:

$$d_{departure} = 0.0208\beta \left[\frac{\sigma}{g(\rho_l - \rho_g)}\right]^{\frac{1}{2}} \tag{2.4}$$

Where, $d_{departure}$ is the bubble departure diameter, σ is the surface tension, g is gravitational acceleration, and β is the contact angle of the liquid on the surface in degrees. [9] A dependence of boiling on surface wettability can be witnessed from this correlation, as presented in Figure 2-4.

Alternatively, *Cole and Rosenhow (1969)* predict bubble departure diameter as [10],

$$d_{departure} = 1.5 \times 10^{-4} \left[\frac{\sigma}{g(\rho_l - \rho_g)}\right]^{\frac{1}{2}} Ja^{*\frac{5}{4}} \tag{2.5a}$$

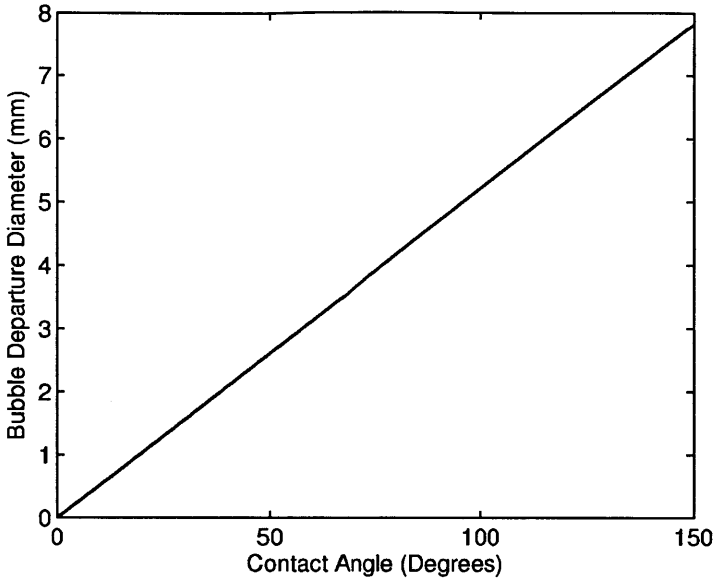

Figure 2-4: Fritz equation for bubble departure diameter.

$$Ja^* = \frac{\rho_l c_{p,l} T_{sat}}{\rho_g h_{fg}} \tag{2.5b}$$

Where $c_{p,l}$ is the specific heat capacity of the liquid. While the *Cole and Rosenhow* correlation does not account for wettability, it is a useful tool for understanding how bubble departure diameter varies with system operating pressure. Other bubble departure diameter models are more complex and solve for diameter by summing inertial, buoyancy, drag and surface tension forces. [11] However, these correlations are an adequate starting point for bubble departure diameter analysis. In this instance, bubble diameter is important in order to position engineered nucleation sites such that adjacent bubbles positively interact (more pertinent to the Spot Patterning portion of this investigation). In other words, it is important to ensure that excessive bubble coalescence, due to tight packing of nucleation sites, does not undermine nano-engineering efforts.

2.1.4 Bubble Frequency

The bubble departure frequency is an important metric in quantifying the capacity of a fluid to remove heat from the surface. Calculated for a given nucleation site, this frequency is dependent on both the bubble growth time, t_g, and the waiting period between bubbles, t_w.

$$f = \frac{1}{t_g + t_w} \tag{2.6}$$

It is apparent that bubble departure frequency is highly coupled to the bubble growth equations presented earlier. Though this is not an exclusive relationship. In fact at low heat fluxes, the waiting period is much longer than the growth period. The waiting period depends on the heat flux, the liquid and surface heat diffusivities and the critical superheat for bubble nucleation, *not* on the growth rate of the bubble. [2] As such, bubble frequency is also a function of a variety of surface and operating conditions. Because bubble departure frequency is easier to observe during experimentation than other bubble characteristics, it is a good metric for inferring the effectiveness of boiling on a given surface.

All nucleation sites on a heater surface are not active simultaneously. Moreover, their relative spacing and size can cause the activation of a given site to influence others. *Calka and Judd (1985)* approached nucleation site activation by taking a ratio of the intersite spacing, a, and the bubble departure diameter, d_d. Through their theory, if $\frac{a}{d_d} < 1$ then the interaction between two sites is attractive. The activation of one site leads to the activation of the other. This occurs because the vapor from the first site reaches and seeds the second site. If $1 < \frac{a}{d_d} < 3$ the interaction between two sites is repulsive. The exact mechanism of deactivation is not entirely understood, but has been experimentally observed. Finally, if $3 < \frac{a}{d_d}$, the two sites operate independently. [12] *Zhang et al. (2003)* also found similar site spacing to drive hydrodynamic between departing bubbles, thermal interactions between nucleations sites and bubble coalescence. [13] Their findings are good reference tools for the spacing of features on engineering surfaces.

2.1.5 Bubble Coalescence

Coalescence can occur between vertically stacked and horizontally adjacent bubbles. This happens both on the heat transfer surface or within the working fluid, well away from the surface. In regards to heat transfer, horizontal bubble coalescence on the heat transfer surface is the primary concern. However, it should be noted that *Buyevich and Webbon (1996)* have examined vertical bubble coalescence and concluded that the formation of a vapor column can inhibit surface rewetting, leading to CHF [14].

For horizontal bubbles, the coalescence criterion simply requires the bubble diameter to be greater than the spacing between nucleation sites. *Bonjour et al (2000)* examined bubble coalescence as a function of site spacing and its effect on the HTC. The researchers consider the influence area of a departing bubble, a notion originally developed by *Han and Griffith (1965)*. [15] When a bubble departs the surface, it also removes a layer of the surrounding superheated liquid with it due to vortex action. The area of influence diameter is accepted to be one to two times as large as the bubble diameter [15]. *Bonjur et al (2008)* examined the spacing of three nucleation sites in a triangular pattern. Optimal heat transfer was achieved at a spacing where the three areas of influence were tangent (in other words the intersite spacing is equal to the area of influence diameter). In this scenario, central liquid region, outside of the areas of influence can also remove with bubble departure. In geometries where the site spacing is smaller, overlapping areas of influence minimize the superheated liquid removed by capillary action. [16] Additionally, an excessively large intersite spacing prevents the removal of the central liquid surrounded by the areas of influence. If the bubble departure diameter can be accurately characterized, nucleation sites on an engineered surface can be spaced to exploit this behavior.

Mukherjee and Dhir (2004) performed numerical simulations, as well as boiling experiments and also found some bubble coalescence to enhance the HTC. During bubble merging, a vapor layer connects the two sites, trapping and removing the underlying liquid layer. Additionally, the contraction of two bubbles following their coalescence drew cool water in towards the heat transfer surface [17]. These analytical and experimental results continue to support the conclusion that some bubble coalescence can be beneficial to a heat transfer

system.

2.2 Surface Characteristics

Surface morphology and chemistry have pronounced effects on CHF and HTC. Specifically, surface roughness, porosity and wettability are suspected to influence boiling behavior. As these three surface characteristics are the primary subject of this investigation, it is important to define these characteristics.

2.2.1 Roughness

Roughness has historically been attributed to have large effects on HTC, made famous by *Berenson's* 1960 study on pool boiling. [4]. Surface roughness is essentially a measure of a surface's texture. It is characterized by vertical (positive or negative) deviations from an ideal, flat surface. [18] The roughness of a surface can be understood from Figure 2-5.

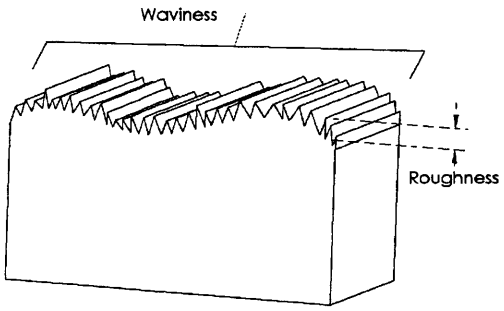

Figure 2-5: Unidirectional surface roughness and waviness.

Surface roughness and waviness is depicted, which can be considered somewhat separate characteristics. [18]. For the purposes of this investigation, only surface roughness is considered. All test specimens in this study have no waviness associated with their surface topography. Additionally, roughness can arise from a variety of surface textures. For simplicity, Figure 2-5 illustrates unidirectional trench type roughness. However, roughness can be a result of multidirectional surface texture, surface extrudes, and divots. There are

numerous methods to define roughness. For example, often utilized in science and industry are:

1. R_a, the arithmetic average of the absolute value of surface feature heights.
2. R_{RMS}, the root mean squared of the arithmetic average.
3. R_z, the average distance from the highest peak to lowest valley of numerous sample lines.

Here, R_a and R_z are used to characterize the roughness of the heater surfaces. The measurement of R_a surface roughness can be performed by taking the cross section of a surface and analyzing the height variation along a horizontal line, as depicted in Figure 2-6.

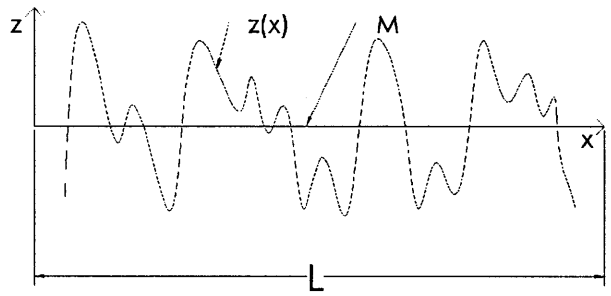

Figure 2-6: Arithmetic average roughness (R_a).

Mathematically, this roughness can be represented as,

$$R_a = \frac{1}{L}\int_0^L |z(x)|dx \tag{2.7}$$

Where, $z(x)$ is defined as the the vertical distance from the mean surface line, M, and L is the length over which the surface roughness is measured. [18]

R_z differs in how it is defined and can be understood from Figure 2-7. Here, roughness is characterized by the average height distance between the five highest peaks and five lowest valleys.

Mathematically, R_z can be calculated as,

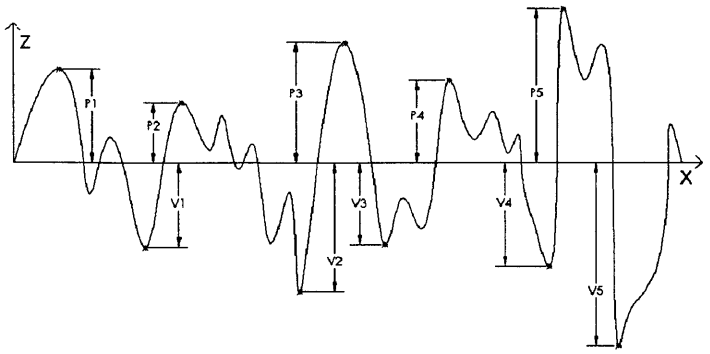

Figure 2-7: R_z surface roughness.

$$R_z = \frac{1}{5}\left[\sum_{i=1}^{5} Pi + \sum_{i=1}^{5} Vi\right] \tag{2.8}$$

For surfaces comprised mainly of extruded features and a lack of valleys, R_z approaches the value of the average feature height. Through both the use of R_a and R_z heater surface roughness can be adequately characterized.

2.2.2 Porosity

Surface porosity can enhance pool boiling heat transfer through a variety of hypothesized mechanisms. For example, porosity can increase the nucleation site density, by creating cavities to seed bubble formation. [19] Moreover, the interconnection of the porous structure allows for transport of liquid between nucleation sites. Therefore, rewetting of nucleation sites is enabled, which can help delay CHF. [20] Finally, surface rewetting is further promoted through capillary action induced by the porous structure. [19] However, a porous layer can also have negative attributes. The porous structure can attract surface contaminant, accelerating fouling of the heat transfer surface. Additionally, the thickness of the layer also adds an additional thermal resistance to the heat transfer system. Therefore, balancing the positive and negative consequences of a porous surface is integral to its inclusion in a heat transfer system.

2.2.3 Wettability

As described in Section 2.1.1, the contact angle is an important parameter in understanding bubble nucleation. A hydrophilic surface attracts water and can improve boiling performance through surface rewetting following bubble departure. Conversely, a hydrophobic surface repels water and can be detrimental to boiling; however, hydrophobicity does promote bubble nucleation. Typically, 90° is considered neutrally wetting, with lesser angles being hydrophilic and greater angles being hydrophobic. Contact angle is primarily a function of surface chemistry, but can also be affected by other surface characteristics. For example, roughness has the effect of making hydrophilic surfaces more hydrophilic and hydrophobic surfaces more hydrophobic.

In assessing wettability, the methods of contact angle measurement must be considered. There are multiple types of contact angle measurements, three of which are of particular importance to boiling. These are the static, advancing, and receding contact angles. The static contact angle is simply the angle between of the surface and the liquid bubble in a stationary setting, as measured 0.5 seconds after contact of the droplet with the surface. The contact angle is measured after $0.5s$ because super hydrophilic surfaces tend to spread liquid very rapidly. Observation of contact angle at a specific time interval adds a level of uniformity to the measurement. The advancing contact angle is the angle that the water makes with the surface as the liquid/vapor/surface contact line is moving forward towards a non-wetted area. Conversely, the receding contact angle is the angle made by the water and the surface as the liquid/vapor/surface contact line moves backwards towards the already wetted area. All three contact angle measurements offer important insight into the behavior of a liquid drop on the heater surface of interest because during bubble growth and departure the bubble base both advances and recedes on the solid surface.

Finally it is important to consider the manner in which liquid wets a surface in the presence of surface roughness or features. Two regimes exist: Cassie and Wenzel. In the Cassie model, a liquid droplet sits atop surface features, as depicted in Figure 2-8a. This is commonly observed with hydrophobic surfaces. Conversely, in the Wenzel regime, the liquid fills the voids between surface features, as illustrated in Figure 2-8b. Hydrophilic surfaces

commonly exist in this regime as the intrinsic wettability attracts water towards the surface. Additionally, it is possible for a water droplet initially in the Cassie regime to transition to the Wenzel regime as a result of external stimuli.

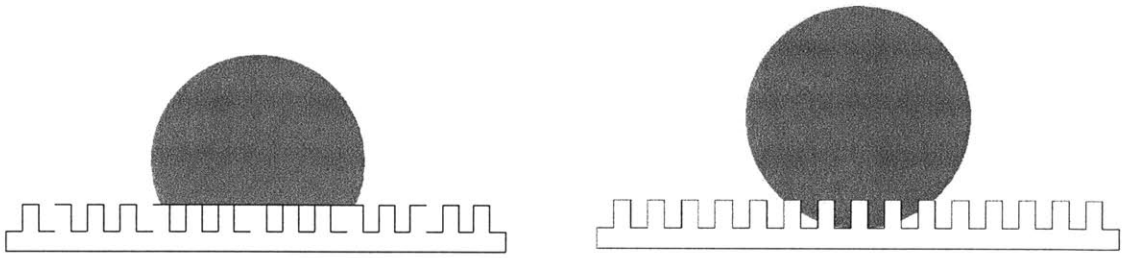

(a) Cassie (b) Wenzel

Figure 2-8: Cassie and Wenzel wettability regimes.

2.3 Pool Boiling Heat Transfer and Critical Heat Flux

2.3.1 Pool Boiling Overview

Beyond understanding bubble nucleation, growth and departure phenomena, pool boiling must also be considered on the macro-scale. The term pool boiling refers to heat being transferred from a surface to liquid macroscopically at rest. Pool boiling is best understood through introduction of a boiling curve, as presented in Figure 2-9. There are many distinct regimes in a boiling curve, each depicting the behavior of the boiling system. At low heat flux, heat is transferred to the liquid via natural convection. In this regime, the temperature of the fluid immediately adjacent to the heater surface increases, thereby lowering its density, causing it to rise due to buoyancy forces. [1] In Figure 2-9, this region is from Point A to Point B.

Increasing heat flux eventually results in the onset of nucleate boiling (Point B), where vapor bubbles forming on the surface remove heat. Nucleate boiling is capable of transferring

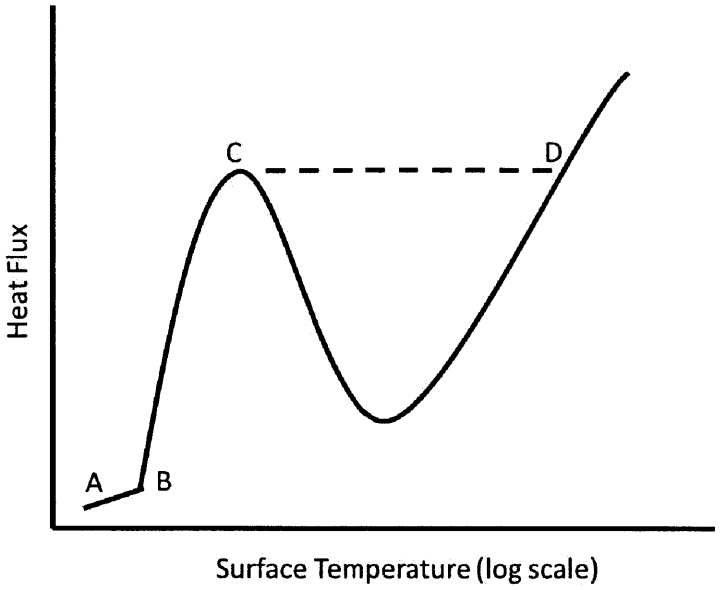

Figure 2-9: Characteristic pool boiling curve.

significant amounts of energy because of the large heat of vaporization required for phase change during bubble formation. [2] As such, the surface temperature does not rise as fast with increasing heat flux in this regime. Eventually, as the heat flux is driven upwards, there is a sharp drop in heat transfer coefficient, occurring at point C; this is known as critical heat flux. [1] If the heat flux remains constant, the system will translate to point D on the boiling curve and enter the film boiling regime. Here, a thin vapor layer exists on the heater surface, through which heat must conduct before being transferred to the liquid. This markedly less efficient heat transfer mechanism results in a rapid rise in heater surface temperature, which often leads to heater burnout. [1]

The heat transfer from the wall to the bulk fluid can be modeled by Newton's law of cooling,

$$q'' = h(T_{wall} - T_{bulk}) \tag{2.9}$$

Where q'' is the heat flux, h is the heat transfer coefficient (HTC), T_{wall} is the wall temperature, and T_{bulk} is the bulk liquid temperature (however in boiling T_{bulk} is always assumed to be T_{sat} even if $T_{bulk} < T_{sat}$). In this relationship, the HTC is a measure of of

boiling performance and is a good way to characterize a heater surface. Often in boiling heat transfer, HTC will exhibit a temperature dependence.

2.3.2 Critical Heat Flux

While the driving factors behind CHF are not completely understood, many strides have been made into characterizing this occurrence. Four main theories on CHF have been proposed to account for this phenomenon:

1. **Hydrodynamic instability.** Vapor release from the surface is achieved in an ordered array of columns. These jets are initiated from a fundamentally unstable vapor layer immediately above the surface. However, was the velocity of the vapor jets increases, they themselves become unstable and breakdown, inhibiting vapor removal from the surface. As a result, the HTC drops and CHF is achieved. [1,2]

2. **Macrolayer consumption model.** This theory models vapor release as mushroom shaped bubbles. CHF is triggered when the macrolayer behind the departing mushroom bubble is totally evaporated, leaving the heater surface completely bare. [2]

3. **Bubble crowding on heater surface.** The prevalence of vapor bubbles on the surface continues to increase until the entire heater is covered with adjacent bubbles. The vapor bubbles eventually coalesce and form a uniform film layer between the heater and the liquid, triggering CHF. [2]

4. **Hot spot heating.** As the surface temperature increases, individual hot spots form. At these points on the heater surface, the temperature reaches a value at which it cannot be adequately rewetted. As more and more of these spots form on the surface, CHF ensues. [2] Though in principle, it is possible for a single irreversible hot spot to form and grow to cover the entire surface, leading to CHF.

These postulates are somewhat contradictory and finding evidence for the conclusive support of a single theory is difficult. *Zuber (1959)* worked with the hydrodynamic instability model and predicts CHF as, [21],

$$q''_{CHF} = K\rho_g h_{fg}\left[\frac{g\sigma(\rho_f - \rho_g)}{\rho_g^2}\right]^{1/4} \tag{2.10}$$

Where, q''_{CHF} is the critical heat flux, K is a dimensionless constant that captures geometry of the boiling surface, h_{fg} is the latent heat of vaporization. While traditionally popular, this model is rooted only in hydrodynamics and does not account for surface characteristics, such as roughness, porosity, or wettability. Many pool boiling investigations have determined there to be an effect of surface characteristics on boiling performance. [4,20,22–24] As such, this correlation is a good starting point, but does not fully capture the boiling phenomenon.

More recently, the inability of a surface to rewet after bubble departure has become the dominant theory behind CHF. [11] Temporary dry spots begin to form on the surface, with the frequency and size of such dry spots increasing, until the critical heat flux (CHF) is reached (Point C in Figure 2-9). At this point, the surface cannot rewet fast enough to replace the vapor lost through nucleation and a thin vapor layer forms immediately above the heater surface.

Other models have been proposed to predict CHF, whilst including the effects of surface characteristics. *Kandlikar (1996)* created a model to predict pool boiling CHF as a function of contact angle and heater orientation.

$$q''_{CHF} = h_{fg}\rho_g^{1/2}\left(\frac{1+cos(\beta)}{16}\right)\left(\frac{2}{\pi}+\frac{\pi}{4}(1+cos(\beta)cos(\phi)\right)^{1/2}(\sigma g(\rho_f-\rho_g))^{1/4} \tag{2.11}$$

Where, β is the receding contact angle of the surface, and ϕ is the heater angular orientation. Figure 2-10 depicts the theoretical dependence of CHF on surface wettability for a horizontally oriented heater ($\phi = 0$.

This model offers more insight into the prediction of CHF, as it captures at least one surface characteristic. However, the effects of roughness and porosity are absent.

Polezhaev and Kovalez (1990) derived a semi-empirical correlation, rooted in the Zuber hydrodynamic instability theory to relate CHF and porosity. For a uniform porous layer, CHF is predicted as [25]:

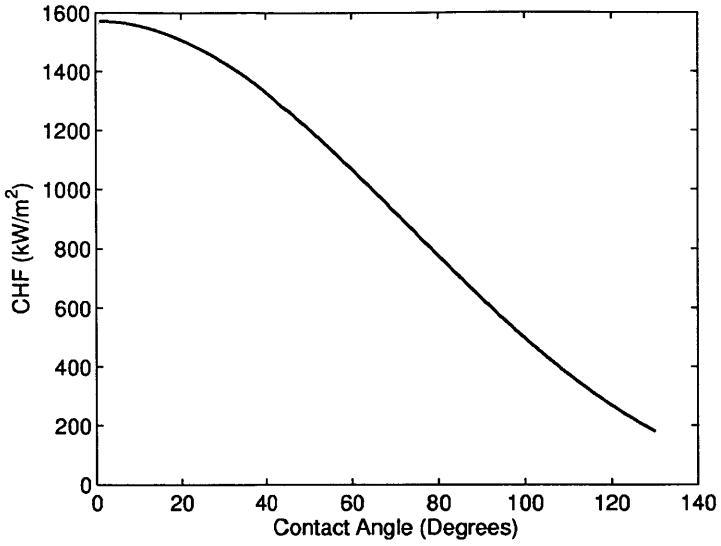

Figure 2-10: Kandlikar model of CHF dependence on wettability. All values for horizontal heater orientation and atmospheric conditions.

$$q''_{CHF} = 0.5\epsilon^{2.28} h_{fg} \left(\frac{\sigma \rho_l \rho_g}{(\rho_f + \rho_g) R_{bg}} \right)^{1/2} \tag{2.12}$$

Where, ϵ is the porosity and R_{bg} is the break through pore radius, which is determined experimentally. However, it can typically be assumed to be half the particle diameter in the surface coating layer. [26] The trends of this correlation can be observed in Figure 2-11.

Predicted CHF increases with increasing porosity, but is inversely proportional to particle diameter. Yet, this correlation does not account for porous layer thickness. Moreover, it may not be appropriate for use on the nanoscale, as the bubble radius will be considerably larger than the characteristic pore size. [26] Additionally, this model largely over predicts the absolute value of CHF. Regardless, like the others, this correlation is a good tool to begin understanding the effects of surface characteristics on pool boiling performance.

While absolute CHF values predicted by the correlations may vary from experimental findings, the trends of the equations offer important insight into the design of heat transfer surfaces. Recognizing the theoretical effect of varying each surface characteristic frames this investigation. However, as this study will show, it will be important to consider *multiple* surface characteristics not just *one* parameter in predicting CHF. Though creating an all-encompassing correlation is not a trivial matter.

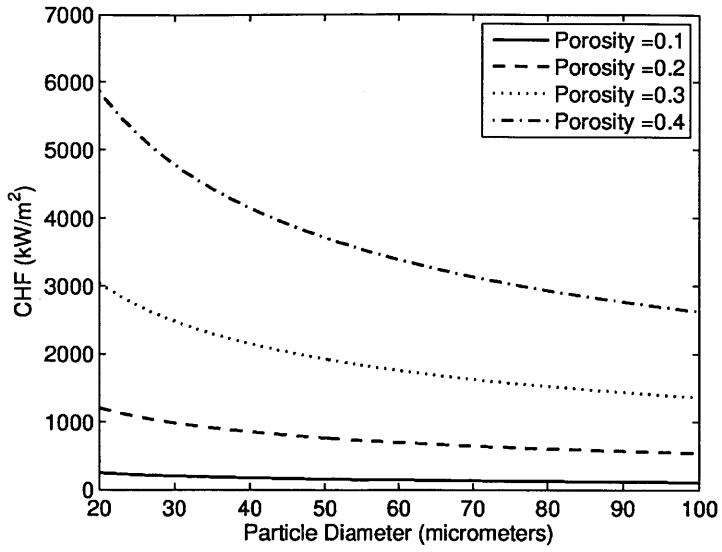

Figure 2-11: Polezhaev model for CHF as a function of particle size and porosity level. Evaluated at atmospheric conditions.

2.4 Surface Engineering

Much research has been conducted into surface engineering for boiling heat transfer improvement. As early as 1962, it was determined that boiling heat transfer could be enhanced by up to 600% through surface roughening [4]. The surface treatment increases the number of nucleation sites, which promotes bubble formation and thus nucleate boiling. Other researchers have characterized the effects of microscale structures. It was determined that micro-roughness, microcavities, and microporosity all have significant ability to enhance nucleate boiling. Specifically, these structures serve to hold a bubble on the surface longer than if it were to form on a smooth surface [27]. Most recently, the effects of nanoscale features have come into focus. Methods include altering the boiling surface chemistry, randomly roughening of a surface, and enginering patterns of cavities. These investigations offer insight into surface wettabillity, as well as bubble departure diameter, departure frequency and coalescense. Cumulatively, these characteristics help to govern the overall heat transfer rate and CHF. Here, a brief overview of previous research in this field is presented.

2.4.1 Surface Roughness and Porosity

Because surface roughening was early identified as a means to enhance boiling heat transfer, this subject has been researched extensively. *Berenson (1960)* used emery paper as well as lapping compound to create surfaces with varying roughness. Additionally, he investigated the effects of roughening procedures, such as rubbing in one or two directions or in circular motions [28]. Through these efforts, it was determined that increasing surface roughness reduces the temperature difference required to transfer a given heat flux [4].

More recently, researchers have painted surfaces with particle containing mixtures to achieve surface roughness. For example, *Chang and You (1997)* individually mixed aluminum, copper, diamond, and silver particles with epoxy to create brushable compounds. Particle sizes ranged from $1\mu m$ to $50\mu m$ and created microstructures, resulting in increased surface porosity. Through this technique, the researchers were able to enhance the overall HTC by 330% and CHF by 100% over an untreated surface with saturated FC-72 [22]. *O'Connor and You (1995)* also employed painting techniques with silver flakes and epoxy. Similar increases in HTC and CHF were realized and attributed to the microstructures ability to quickly heat liquid on a local level as well as promote internal vaporization in the proximity of bubble embryos [29].

Li et al. (2008) used an electrodeposition process to create a well ordered, three dimensional surface layer with both micro and nanoscale features. The copper dendritic structures that were formed were highly interconnected and microporous. The researchers suspect that the nanocavities initiate bubble generation, but the larger macro-scale voids actually serve to promote bubble growth. This surface conditioning resulted in a heat flux seventeen times higher than a plain surface [30].

Ahn et al. (2009) created heater surfaces with vertically oriented carbon tubes, with diameters of $30nm$ and heights of $9\mu m$ and $30\mu m$. A weak dependence of boiling performance on carbon nanotube height was found. However, the taller carbon nanotubes were able to realize a 40% CHF enhancement, compared to a bare silicon surface. The researchers hypothesize that the boiling enhancement stems from increased heat transfer surface area, greater liquid-solid contact, and a pinning of the liquid-vapor contact line, which may alter

bubble nucleation profiles. [31]

Furberg et al. (2009) deposited nano and microporous copper structures on stainless steel heat exchanger plates. At low heat fluxes, the researchers were able to realize a ten times HTC improvement using R-134a as a test medium. The overall HTC during the experiment was enhanced by 100%. [20]. Here, the researchers were able to clearly identify the advantages of a porous heat transfer surface.

Similarly, *Chen et al. (2009)* patterned silicon and copper nanowire arrays on heater surfaces, and achieved both CHF and HTC enhancement of 100%. This enhancement is attributed to a high nucleate site density, superhydrophilicity, and capillary pumping action stemming from the natural structure of the nanowires. [23]

2.4.2 Nanofluids

While this investigation does not employ nanofluids explicitly, the following studies still offer important insight into the engineering of boiling surface. Many studies have been conducted using nanofluids as a boiling medium. Consisting of a base fluid and dispersed nanoparticles, nanofluids offer potential to enhance CHF. Numerous investigations have established that CHF enhancement results from nanoparticles being deposited on the heater surface. [32–35] For example, *Kim et al. (2006)* deposited nanoparticles on heater surfaces during pool boiling with TiO_2-water and Al_2O_3-water nanofluids. Subsequently, pool boiling tests were performed using the predeposited surfaces, but with pure water. CHF enhancement was recorded over pure water boiling on clean surfaces, thus indicating the effect of nanoparticles deposited on the surface. [32] It has been further established that the nanoparticles serve to improve the wettability and capillarity of the heating surface, which could drive CHF enhancement. [33]

Kwark et al. (2010) performed similar nanoparticle deposition tests during pool boiling. It was confirmed that the surface coatings are constantly being modified during nanofluid boiling and that there is a dependence of boiling performance on nanoparticle coating thickness. [34] Additionally, similar tests were performed with both water and ethanol nanofluids. More significant enhancement was seen with ethanol and this is attributed to the smaller bubble departure diameter of bubbles boiling in ethanol (due to surface tension). [34]

Kim et al. (2007) modeled the system of deposited nanoparticles as a thin absorption layer, which helps to describe how the nanoparticles alter the surface wettability. [35] That nanofluids can enhance CHF through surface deposition of nanoparticles opens up much space for heater surface engineering.

Ahn et al. (2010) created artificial micro and nanostructures that mimicked those created naturally during pool boiling with nanofluids through nanoparticle deposition. Here, the researchers were able to conclude that the micro and nanostructures enhanced CHF not only by increasing wettability, but also liquid spreading. The researchers developed a model to predict liquid spreading and found that the tested surface with the highest degree of liquid spreading to also had the greatest CHF value. [36]

2.4.3 Surface Chemistry

Through surface chemical treatments, many researchers have been able to control the wettability of boiling surfaces. *Phillips (2011)* explored the effect of porous hydrophobic and hydrophilic heater surfaces, as well as patterns of hydrophobic and hydrophilic spots. These patterns were created through a layer by layer (LBL) dipping process in a nanoparticle solution. Hydrophilic heater surfaces promoted rewetting during boiling, thereby enhancing CHF by around 100% [24]. Patterns of hydrophobic spots on a hydrophilic heater were designed to create distinct nucleation sites. The spot diameters were $160\mu m$ and $260\mu m$ on $1mm$ and $2mm$ hexagonal pitches. However, such patterns did not significantly increase the HTC and resulted in CHF values lower than purely hydrophilic surfaces [24].

Betz et al. (2010) created similar patterns of both hydrophobic spots on hydrophilic surfaces (hydrophilic network) and hydrophilic spots on hydrophobic surfaces (hydrophobic network). In this experiment, spot spacing varied between $50\mu m$ and $200\mu m$, with the spot diameter ranging between 40% and 60% of the spacing dimension [37]. Hydrophobic networks resulted in the highest enhancement of HTC, but in some instances reduced CHF. Hydrophilic networks improved the HTC moderately, but also enhanced CHF. Overall, this study found such spot patterns to enhance CHF and HTC by 65% and 100%, respectively over a nominally hydrophilic surface [37].

Phan et al. (2009) examined the influence on nucleate boiling heat transfer by varying

water contact angles from 10° to 110° through nanoscale surface topography and chemistry. It was found that hydrophilic surfaces can increase the bubble departure diameter and reduce the departure frequency. For contact angles between 45° and 90°, the HTC was found to decrease. However, for contact angles less than 45°, the HTC increased. Therefore it is hypothesized that optimal contact angles for HTC are 0° and 90°. Conversely, hydrophobic surfaces require less superheat to initiate bubble growth, but it can be more difficult for a bubble to finally detach from the surface. Additionally, it was found that bubbles on hydrophobic surfaces can move around and coalesce with bubbles from adjacent sites, which ultimately can lead to a vapor blanket covering the heat transfer surface. [38]

2.5 Conclusions from Prior Research

Insight gained from this literature review guided the design of the heat transfer surfaces in this investigation. In summary, the important conclusions are:

1. Surface roughness and porosity can enhance the performance of a boiling surface. However, it is important to investigate each parameter's effect on boiling individually. In particular, some surfaces considered rough, may in fact be benefiting primarily from a degree of porosity.

2. Porosity can have profound effects on HTC and CHF, largely a result of the interconnection of nucleations sites.

3. Hydrophilic surfaces can promote rewetting and thereby delay CHF.

4. Hydrophobic surfaces can be unstable, enabling lateral bubble movement, which can create a vapor blanket on the surface.

5. A high degree of liquid spreading on a surface can help to inhibit CHF.

6. Particles deposited on a surface can enhance wettability.

7. The intersite spacing of nucleation sites is an important parameter in governing the individual site activation and bubble frequency.

8. Some bubble coalescence can enhance a boiling surface by removing the trapped liquid between departing bubbles. However, too much coalescence can be detrimental to the system. Again, the intersite spacing dictates the behavior of the coalescence.

Chapter 3

Test Matrix

3.1 Separate Effect Investigation

As identified through literature review, it is well understood that roughness, porosity, and wettability all affect the performance of a heater surface. However, the exact extent to which each characteristic influences boiling is not known. In this investigation, each surface parameter is individually varied, allowing the separate effects to be isolated. Furthermore, combinations of these surface parameters are also examined, providing insight into the coupled affects of the surface features.

3.1.1 Roughness

Two categories of heater roughness are considered: Rough and Smooth. The respective roughness characteristics are defined in Table 3.1.

By fabricating rough and smooth heaters, it is possible to determine the effect surface roughness has on HTC and CHF. Primarily, the focus here is on whether or not surface rough-

Surface	$R_a(\mu m)$	$R_z(\mu m)$
Smooth	< 0.1	< 1
Rough	> 1	≈ 15

Table 3.1: Smooth and Rough heater surface roughness characteristics.

ness is present, not examining the effect of varying the magnitude of the surface roughness (though this is a good space for future work). Therefore, only these two categories of surface roughness are considered.

As received, the heater surfaces are nanosmooth. To induce surface roughness, small posts are fabricated on the surface of the heater. These features are $20\mu m$ in diameter, $15 - 20\mu m$ tall. The posts are spaced on a hexagonal pitch of $500\mu m$, which is sized large enough to avoid inducing capillary effects. While capillary wicking can be beneficial to CHF, this investigation seeks to understand the effects of roughness independent of the wicking phenomenon. Posts of a similar design have been employed with success in the past by *Troung (2011)* to investigate roughness effects. [26]

3.1.2 Porosity

As with roughness, porosity is considered in a binary context. Heater surfaces are either non-porous or porous. Porosity is created by depositing nanospheres on the surface. These spheres closely pack, naturally resulting in a porosity in the range of 50% to 60% of the total volume. The particle diameter used to create the porous layer is $50nm$ and the characterisitic pore size is on thesame order of magnitude. This pore size was selected, as it was previously identified by *Phillips (2011)* as a particularly well performing heater surface.

It is important to recognize that the fabrication of a porous layer on the heater surface can also induce roughness. While this roughness can be appreciable when compared to the nanosmooth, as received ITO-Sapphire heater, it is orders of magnitude less than the roughness imparted by the post features. As such, all heater surfaces with an $R_a < 0.1\mu m$ will be considered Smooth in the context of this investigation.

3.1.3 Wettability

Finally, two regimes of wettability are also investigated: hydrophobic and hydrophilic. In this investigation, hydrophobic is defined by a contact angle of greater than 110°, with hydrophilic being a contact angle less than 10°. In some test cases, the level of hydrophobicity or hydrophilicity may exceed the stated value. This stems from the fact that contact angle

is a function not just of wettability, but also porosity and roughness. For example, porosity has the effect of increasing the contact angle of hydrophobic surfaces, while decreasing the contact angle of hydrophilic surfaces. As such, limits are set for hydrophobic and hydrophilic thresholds. However, the contact angle for each heater surface is characterized and imaged before heater testing.

3.1.4 Overall Separate Effect Test Matrix

The overall test matrix of heater surfaces for the Separate Effect investigation is presented in Table 3.2. By examining all combinations of different surface parameters, it is possible to understand how different traits can have compounding effects on HTC and CHF. The attributes for each heater surface presented in Table 3.2 are target values. Measurements of each characteristic are made on the actual heater surfaces. Additionally, for each surface configuration, three nominally identical heaters are fabricated and tested.

Additionally, a modified Rough Non-porous Hydrophilic heater, with a different post pitch is fabricated and tested. This is somewhat separate for the main investigation and intended to investigate how the roughness would affect boiling at elevated pressures. For clarity, this modified test case is not included in the Test Matrix table. In the modified case, the pitch on which the posts are patterned is $1.98mm$. This increased pitch is designed to mimic the relative the relative dimensions of bubbles in a system pressurized at $5bar$ and the nominal pitch of $0.5mm$. In other words, the relationship between the bubble departure diameter at atmospheric conditions and the modified pitch ($1.98mm$) is identical to the relationship between bubbles departing the surface at $5bar$ and the standard post pitch ($0.5mm$). The *Cole and Rosenhow* correlation is used to predict the bubble departure diameters. This offers insight into how the roughness condition might affect a boiling system at elevated pressures.

Pattern	Roughness	Porosity	Wettability
	R_a and $R_z(\mu m)$	Volume Fraction (dimensionless)	Static Contact Angle (degrees)
Uncoated Heater (reference)	$R_a < 0.1$, $R_z < 1$	0	$60° - 70°$
Smooth Non-porous Hydrophilic	$R_a < 0.1$, $R_z < 1$	0	$< 10°$
Smooth Non-porous Hydrophobic	$R_a < 0.1$, $R_z < 1$	0	$> 110°$
Smooth Porous Hydrophilic	$R_a < 0.1$, $R_z < 1$	$50 - 60$	$< 10°$
Smooth Porous Hydrophobic	$R_a < 0.1$, $R_z < 1$	$50 - 60$	$> 110°$
Rough Non-porous Hydrophilic	$R_a > 1$, $R_z \approx 15$	0	$< 10°$
Rough Non-porous Hydrophobic	$R_a > 1$, $R_z \approx 15$	0	$> 110°$
Rough Porous Hydrophilic	$R_a > 1$, $R_z \approx 15$	$50 - 60$	$< 10°$
Rough Porous Hydrophobic	$R_a > 1$, $R_z \approx 15$	$50 - 60$	$> 110°$

Table 3.2: Separate Effect investigation test matrix.

3.2 Spot Patterning for Heater Optimization

Previous research has indicated that hydrophilic surfaces can promote rewetting and enhance CHF. Additionally, it is suspected hydrophobic spots patterned on the nominally hydrophilic heater can serve as individual nucleation sites during boiling, thereby enhancing the HTC. [24] To examine this phenomena, hydrophilic heaters, with hydrophobic spots patterned on a hexagonal pitch are generated. Additionally, to further enhance hydrophilicity and hydrophobicity, porosity is engineered into the heater surfaces, with pore sizes on the order of $50nm$. Spot size and pitch are varied to examine the effect of these dimensions on HTC and CHF. For each pattern, three nominally identical heaters were fabricated and tested to ensure repeatability. The complete spot pattern text matrix is presented in Table 3.3

Patterns A-D are intended to investigate the effect of varying spot pitch on CHF and HTC. Previously, *Phillips (2011)* examined similar spot patterns with $260\mu m$ spots on $2mm$

Pattern	Nominal Spot Diameter (μm)	Pitch (mm)
A	260	0.5
B	260	0.75
C	260	1.25
D	260	1.5
E	90	0.2
F	120	0.75
G	120	2
H	120	0.2

Table 3.3: Spot Pattern Test Matrix.

and $1mm$ pitches. Therefore, $260\mu m$ spot size was selected to complement this prior investigation. During fabrication, the final spot diameter is somewhat reduced from this nominal value. The value of $260\mu m$ was selected by *Phillips (2011)* to achieve a final diameter of around $200\mu m$. [24] However in practice it is been determined that the final spot size is closer to $180\mu m$ after all fabrication is complete. For simplicity, all spot patterns are referred to by their nominal value (e.g. $260\mu m$).

An important consideration in designing the test matrix is the possibility of bubble coalescence during boiling. With a few degrees of wall superheat, the bubble departure diameter is around $1mm$, under atmospheric conditions. Assuming nucleation is centered on the patterned nucleation spots, the vapor bubble will extend from the center of the site by half the departure diameter ($\frac{d_departure}{2}$). Therefore, the criterion for bubble coalescence requires that the intersite spacing (pitch) be equal to the bubble departure diameter, which in this case is considered to be $1mm$.

The spot pitches were selected such that the coalescence threshold was crossed. This allows for insight into the effect of bubble coalesce on the spot pattern performance. Patterns A and B should induce bubble coalescence, while Patterns C and D are spaced wide enough to avoid this effect.

Patterns E-F investigate varying the spot diameter as well as the ratio between spot diameter and pitch. Patterns F and G have pitches of $0.75mm$ and $2mm$, respectively. These pitches were investigated with $260\mu m$ diameter spots in Pattern B and by *Phillips (2011)*. This allows for a direct comparison of the performance of patterns with similar pitches, but varying spot sizes. The spot pitches were again selected such that they straddled the bubble

coalescence threshold. The sizing of Patterns E and H was motivated by *Betz's* 2010 work with similar style spot patterning, described in Section 2.4.3. Here, the relationship between spot diameter and pitch was directly considered. In Pattern E, the spot diameter is 45% of the spot pitch, while Pattern H the spot diameter is 60% of the spot pitch. The objective of Pattern H is to allow a comparison with Patterns F and G (given similar spot diameter), with a drastically reduced pitch. Pattern E allows for comparison with other patterns in terms of diameter to pitch ratio.

Through this test matrix, the effects of both spot diameter and pitch are to be characterized. This will offer insight into the ability to engineer distinct nucleation sites on a boiling surface through manipulation of surface chemistry.

Chapter 4

Experimental Methods

The objective of this project is to investigate the effect various surface treatments and patterns have on HTC and CHF. Heater surfaces must be fabricated with desired features. Next, the surface patterns must be inspected appropriately to confirm the existence and nature of the fabricated features. Finally, the heater must be tested to characterize the surface's boiling performance. Thus, there are three fundamental aspects to the experimental methodology:

1. Surface fabrication
2. Feature verification
3. Heater testing

Given the delicate nature of micro and nanoengineering techniques, it is important that verification methods are employed to examine surface features. Often small, and natural, variations in fabrication procedure can drastically alter the end product. Therefore, care is taken to fully understand all aspects of the heater surface before its boiling performance is tested. Here, the different techniques used to process the heaters are described, framing the overall investigation.

4.1 ITO-Sapphire Heaters

Indium tin oxide-sapphire (ITO-sapphire) heaters are the test bed for this investigation. Supplied by Diamond Coatings, these heaters have been used extensively in MIT's Reactor Thermal Hydraulics Laboratory and are a robust platform for examining surface features. [24] The heater substrate is a $50.8mm$ square sapphire wafer, with a thickness of $0.25mm$. The surface of the heater is polished to a nano-smooth level. Centered on one side of the heater, a $2cm$ wide and approximately $700nm$ thick layer of ITO is deposited across the length of the heater. Two silver electrodes are deposited on the ITO film. Each silver pad begins at the edge of the heater and extends inwards $20.4cm$, with a width of $2cm$. The silver thickness is approximately $20 - 25\mu m$. A diagram of the heater dimensions can be seen in Figure 4-1.

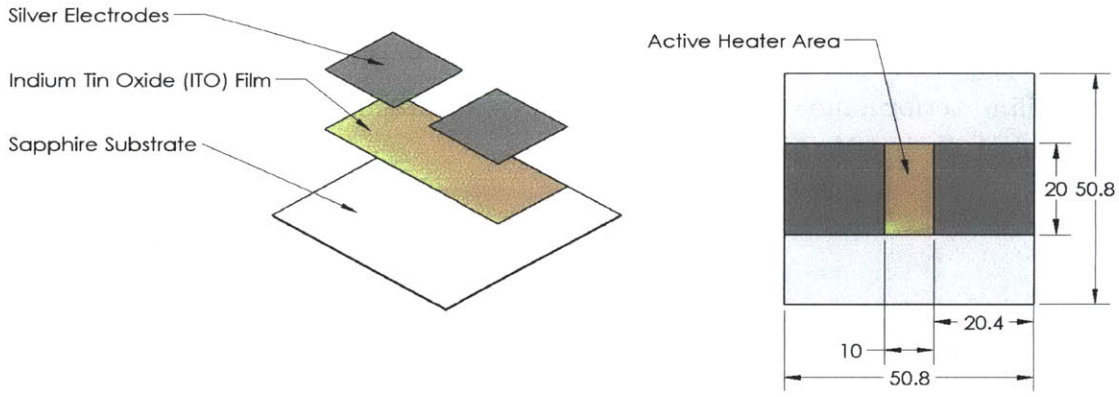

Figure 4-1: ITO-Sapphire Heater (all dimensions in millimeters).

The conductive ITO film and silver pads serve as a resistive heating element and electrode attachment points, respectively. Electrodes are attached to the silver pads with a conductive epoxy to provide power for resistive heating. The center area (2cm x 1cm) of ITO film is the actual active heater area. The resistivity of the active heater area is $10\frac{\Omega}{cm^2}$. Surface features are patterned on the opposite (non-ITO/silver) side of the sapphire substrate. This orientation isolates the electrodes from the water bath, thereby preventing corrosion.

4.2 Surface Fabrication

Numerous methods are employed to customize the heater surfaces. In some instances, a fabrication technique has the effect of altering a single characteristic of the heater surface (e.g. roughness). However, many procedures affect multiple properties of the heater surface. For example, as described below, the method employed to fabricate porosity is accompanied with intrinsic hydrophilicity. In some cases, extra steps must be taken to modify and account for these characteristics. While this is somewhat inconvenient, other factors, such as the simplicity and affordability, justify this coupling. It is therefore simplest to explain the heater fabrication in the context of the different machining operations.

4.2.1 Layer by Layer Deposition

Layer by layer deposition (LBL) is a process in which a single thin layer of nanoparticles is deposited on a substrate surface. A robust recipe for creating LBL coatings using silica (SiO_2) nanoparticles was established by Professors Michael Rubner and Robert Cohen in MIT's Center for Materials Science and Engineering and Department of Chemical Engineering. [39–41] Originally, designed for anti-fogging applications, these coatings have proved durable under boiling conditions. LBL coatings are created by alternatively dipping a substrate in positively and negatively charged solutions. The difference in charge causes particles in the solution to diffuse onto the substrate surface, creating what is known as a bilayer. Dipping operations are carried out on a Zeiss HMS Programmable Slide Stainer.

The negative LBL solution is prepared with intrinsically hydrophilic SiO_2 nanoparticles (Polysciences Silica Microspheres). The diameter of the SiO_2 particles can vary, but here $50nm$ particles are used. As received, these nanoparticles are in an aqueous solution of around 5.9wt%, though the exact concentration varies by production lot. The LBL nanoparticle solution calls for a concentration of 0.03wt% SiO_2 nanoparticles in a pH 9.0 buffer. Therefore, the stock nanoparticles are diluted in a laboratory made buffer solution of deionized water and a mixture of boric acid, KCL and NaOH. Additionally, NaCl is added to bring the solution to a concentration of 0.1M NaCl. This helps create an ionic interface during the adsorption process. An overivew of the chemical mixture for the SiO_2 nanoparticle solution

Figure 4-2: Zeiss HMS Programmable Slide Stainer.

is presented in Table 4.1. Typically one liter batches of nanoparticle solution are mixed for each LBL process. The nanoparticle solution is placed on a stir plate for at least one hour, with care taken to ensure that all the NaCl had dissolved.

Component	**Quantity**	**Purpose**
Deionized H_2O	1 L	Dilution
SiO_2 nanoparticles	Quantity required for 0.03wt%, depending on stock lot concentration	Source of SiO_2 nanoparticles
Boric acid	3.1 g/L	pH 9.0 Buffer
KCL	3.7 g/L	
NaOH	0.86 g/L	
NaCl	5.845 g/L	Aid absorption

Table 4.1: Negative LBL Solution: 0.3wt% SiO_2 nanoparticles of pH 9.0.

For the positive LBL solution, a poly(allylamine) hydrochloride (PAH) solution is prepared to a concentration of $10^{-2}M$ PAH (Aldrich OAH 283223). Additionally the pH of the solution was then adjusted to 7.5 using 1M NaOH. Again, typically one liter of solution was prepared for each LBL process. The PAH solution was mixed on a stir plate for at least thirty minutes.

Component	Quantity	Purpose
Deionized H_2O	1 L	Dilution
PAH	0.9370 g/L	Supply of positive polymer
1M NaOH solution	Quantity required to achieve solution pH 7.5	pH adjustment

Table 4.2: Positive LBL Solution: PAH of pH 7.5.

First the substrate is dipped into the positive PAH solution for ten minutes. After this first coating, the substrate is rinsed in three successive deionized water baths for two minutes, one minute and one minute, respectively. Next, the substrate is dipped in the negative solution for ten minutes. The oppositely charged particles are attracted and diffuse onto the substrate surface. The substrate is subsequently rinsed in three separate deionized water baths following the same rinsing times indicated above. At this point, one bilayer is complete. This process is illustrated in Figure 4-3.

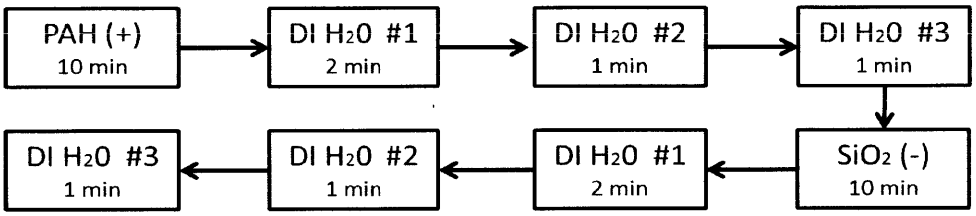

Figure 4-3: LBL process flow.

The complete process is simply repeated for the desired number of particle layers. It is important to note that the thickness of each layer is a function of the particle size and the pH. As particles diffuse onto the surface, the process is self regulating as the surface charge is brought to equilibrium with that of the bath. Therefore, layer characteristics are easily adjusted by altering the chemical composition of the baths. In this arrangement, immersion time in the baths does not play a crucial role in determining layer thickness. The substrate must simply be immersed long enough such that all possible particle diffusion onto the surface has occurred. [39–41]

During layer by layer deposition, the approximately spherical particles assemble in a loose packed fashion. The packing of the particles is around 50% of the total volume. [42] As this

packing is similar for spherical particles of all sizes, the level of porosity is approximately constant regardless of particle size. However, the actual pore size correlates with the particle diameter. For example, a multi-layer surface fabricated with $50nm$ diameter particles will have pores with a characteristic dimension around $50nm$. While this layer achieves the benefits associated with porosity, it does not induce significant roughness onto the heater surface. Most simply, the roughness of this porous layer can be considered to also be on the order of $50nm$. As one would expect, The coating thickness scales with diameter of the nanoparticles and the number of multi-layers deposited. The positive polymer solutioon (PAH) has a negligible thickness in comparision to the nanoparticles and are thus not considered to contribute to the overall layer thickness. [41] Finally, it is important to note that as the SiO_2 nanoparticles are intrinsicially hydrophilic due to their chemical composition, the resulting bilayer surface is also hydrophilic.

Following the LBL process, the bilayers can be calcinated at 550° for one hour to enhance durability and remove some of the polymer layers. The high temperature effectively sinters the nanoparticles together and to the substrate, forming a substantially stronger surface. Removal of the polymer layers leaves behind only the nanoparticle matrix, which can help to improve the wettability of bilayer surfaces fabricated with intrinsically hydrophilic particles. [43]

In some instances, calcination is not possible, as the high temperatures may damage the underlying substrate. Such is the case with the silver electrode pads on the ITO-sapphire heaters. The LBL coatings can also be cleaned with an oxygen-plasma treatment. A Harrick Plasma Plasmaflo is used on the highest power setting, under a $150mTorr$ vacuum for two minutes.

Immediately following plasma treatment, the static contact angle of the heater surface is essentially zero. However, as the primary effects of the plasma treatment process wear off, the contact angle stabilizes around 10°. Because the high energy hydrophilic surfaces tend to absorb contaminants, the heaters are kept in a sealed container until pool boiling testing. Moreover, testing is completed within one week of LBL deposition.

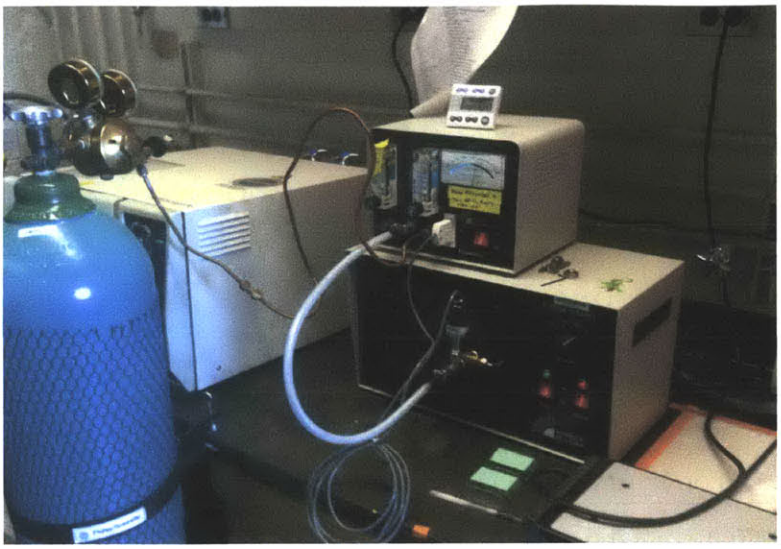

Figure 4-4: Harrick Plasma Plasmaflow.

4.2.2 Chemical Vapor Deposition of Fluorosilane

In order to fabricate a hydrophobic coating, a chemical vapor deposition (CVD) process is employed using 1H,1H,2H,2H-perfluorodecyltriethoxysilane, commonly known as fluorosilane. Fluorosilane is obtained in liquid form. Approximately $5mL$ of fluorosilane are placed in a small open vial, which is in turn placed in a larger poly-tetrafluoroethylene (PTFE) container. The PTFE container is sealed and placed in an oven at 140° for thirty minutes to preheat the fluorosilane and remove any moisture, which can interfer with CVD. The PTFE container is removed from the oven and the substrate to be coated is placed in the PTFE container with the open vial of fluorosilane. For porous surfaces, the container is sealed and placed back in the oven at 140° for another thirty minutes. Non-porous surfaces require longer exposure times to achieve a uniform fluorosilane coating. Non-porous surfaces are placed in the sealed PTFE container and exposed to 140° for eight hours.

The boiling point of fluorosilane is between 103° and 106°. [44] Therefore, the temperatures in the oven are adequate to vaporize the fluorosilane and allow it to deposit on the substrate surface. However, it is important that the surface chemistry be appropriate for binding with fluorosilane. For example, surfaces of SiO_2 are particularly well suited for adhesion with fluorosilane. Surfaces comprised of a material unsuited for fluorosilane treatment

are coated with a thin layer of SiO_2first to prepare them for fluorosilane adhesion. Unlike the LBL process, fluorosilane deposition is not controlled by surface charge. Therefore, multiple fluorosilane layers may be deposited, but their overall thickness is generally negligible in comparison with other surface features (e.g. $50nm$ particles). [45]

4.2.3 Ultraviolet Ozone Patterning

Completely hydrophilic or hydrophobic surfaces can be fabricated with the LBL and CVD processes previously described. However, often it is desirable to create surfaces that have wettability patterns. For example, to have a nominally hydrophilic surface, with hydrophobic spots. One way to create such a surface is through ultraviolet ozone (UVO) patterning. Like plasma cleaning, UVO is a common cleaning procedure to prepare substrates for surface fabrication processes. [46] A typical UVO apparatus emits ultraviolet (UV) light with a wavelength of $184.9nm$, which breaks down oxygen into atomic oxygen. A second wavelength of UV light, this one at $253.7nm$ breaks down ozone by photodisassociation. Highly reactive atomic oxygen oxidize organic materials from the substrate surface. As a result, atomic oxygen is constantly generated, while ozone is continuously created and broken down. [47–49] Through these processes, volatile species can be destroyed on the surface of a substrate.

This technique can be further customized with the use of a patterned mask. If only specific portions of the substrate are exposed to UVO, the resulting effect on the substrate surface will follow a similar pattern as the mask. [50,51] A thin layer of fluorosilane deposited across the entire heater surface can be subsequently patterned with a mask and UVO exposure. A mask is created with the desired fluorosilane pattern opaque to UV light (a positive mask). This effectively protects those regions from the UVO exposure. The remainder of the mask is transparent to UV light, thus permitting the removal of the fluorosilane from the heater surface in those regions. For this process to be successful, it is important that the mask be made of a material that has a high transmission of UV light in the critical wavelengths described previously. Fused quartz silica has better than 90% transmittance for the $184.9nm$ and $253.7nm$ wavelengths. [24] Masks for UVO exposure were fabricated by Advance Reproductions using $2.3mm$ thick fused quartz silica, with the desired pattern printed in a layer of $110nm$ thick chrome. As UVO has the effect of removing the underlying

fluorosilane, these UVO masks are positives, with mask features representitive of the final desired features. The masks used for UVO patterning are presented in Figures 4-5 and 4-6.

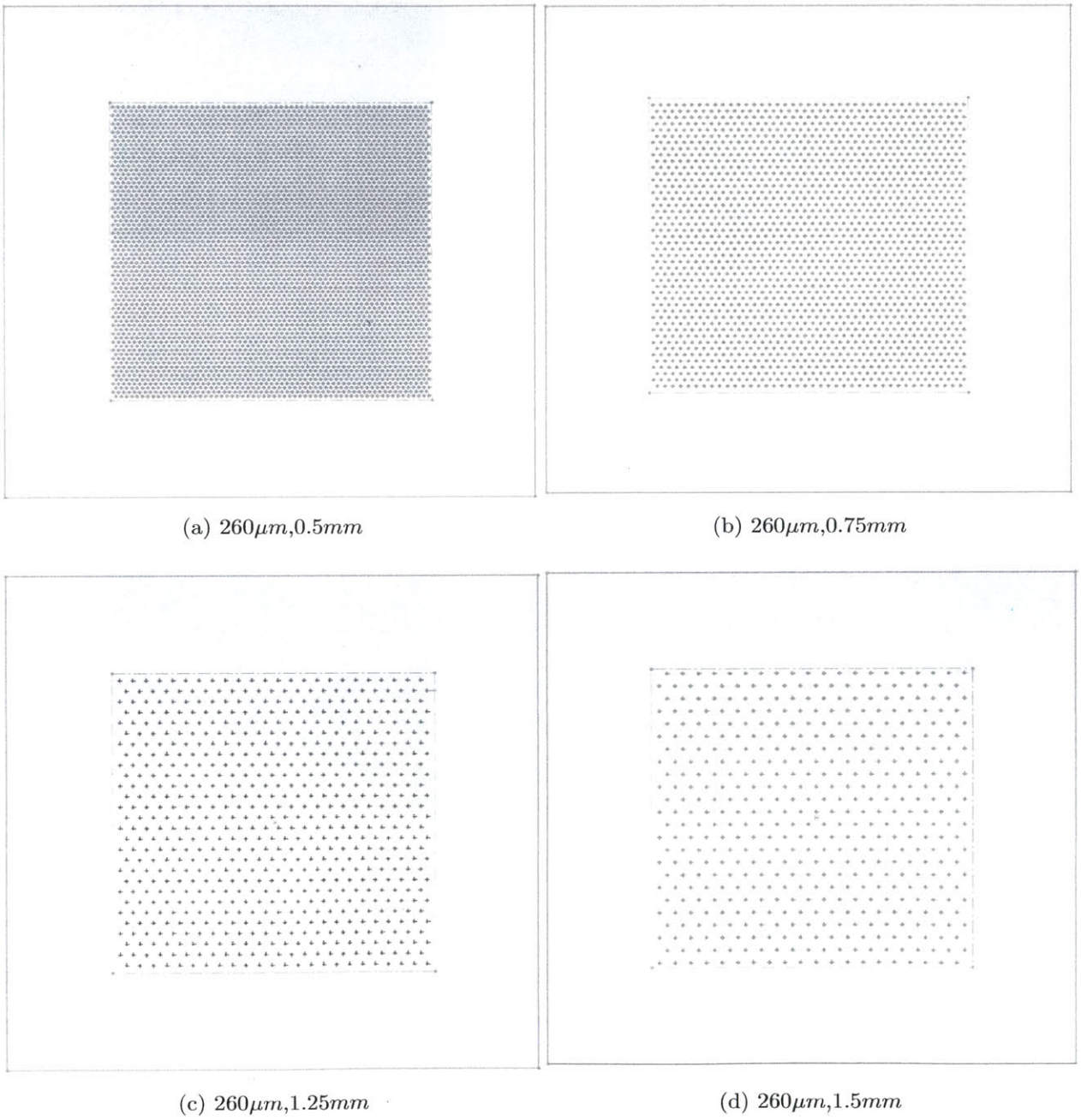

(a) $260\mu m$,$0.5mm$

(b) $260\mu m$,$0.75mm$

(c) $260\mu m$,$1.25mm$

(d) $260\mu m$,$1.5mm$

Figure 4-5: Patterns A-D. Fused quartz with patterned chrome masks for spot patterning. Dimensions presented in the form: spot diameter, pitch

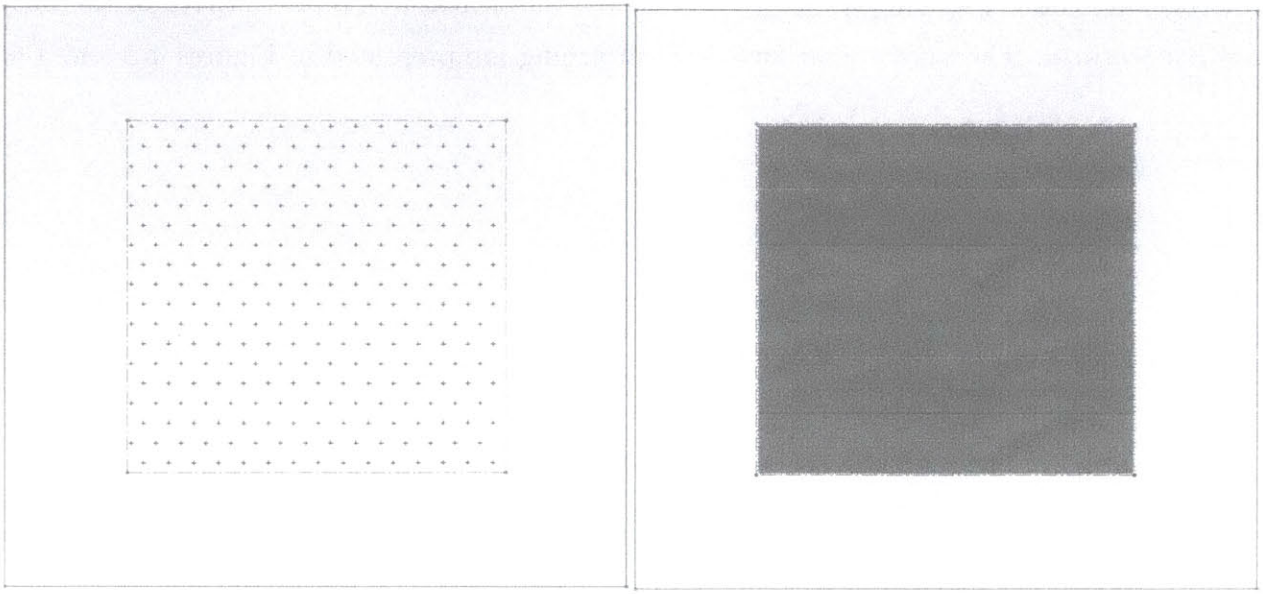

(a) $120\mu m$,$2mm$

(b) $90\mu m$,$200\mu m$

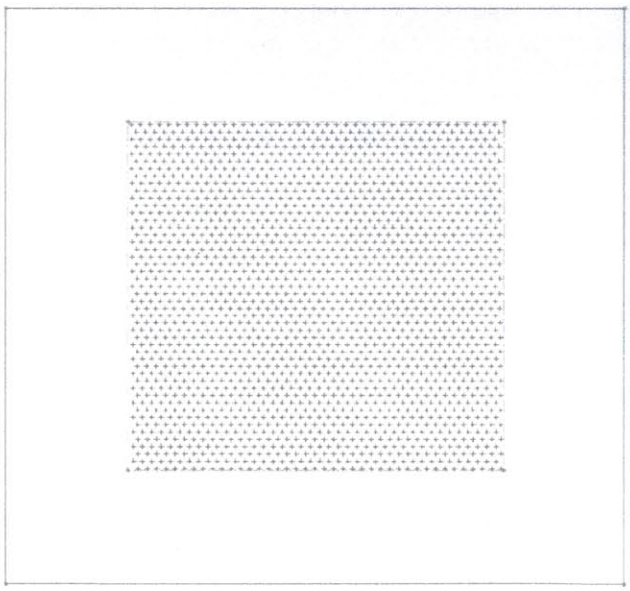

(c) $120\mu m$,$0.75mm$

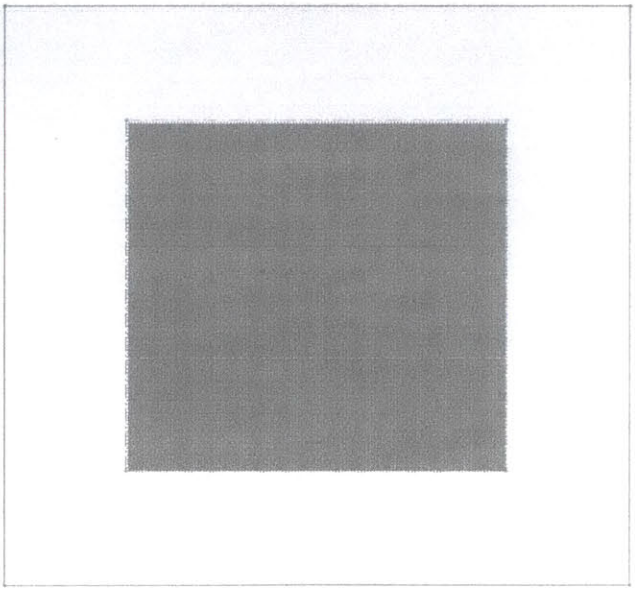

(d) $120\mu m$,$200\mu m$

Figure 4-6: Patterns E-H. Fused quartz with patterned chrome masks for spot patterning. Dimensions presented in the form: spot diameter, pitch.

As illustrated in Figure 4-7 the mask rests on top of the heater substrate, such that the chrome features are on the bottom of the mask are in direct contact with the heater surface. The gap created by the raised chrome features permits the removal of fluorosilane from the

unpatterned areas of the heater. During exposure, the mask is typically placed about $2mm$ from the UV light source.

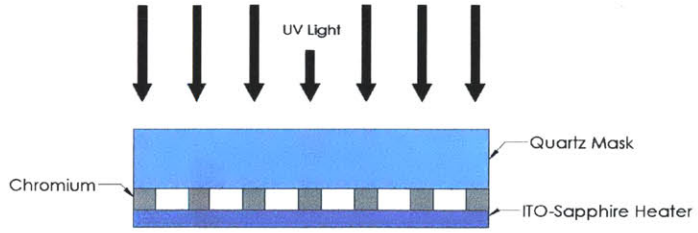

Figure 4-7: UVO Mask and Heater Interface.

4.2.4 Electron Beam Physical Vapor Deposition

Electron Beam Physical Vapor Deposition (EB-PVD) is a deposition method, in which an electron beam is used to vaporize a material, enabling it to coat a substrate surface. The material to be deposited is held in a crucible in the bottom of a vacuum chamber. Through the principle of thermionic emission of free electrons, a stream is generated through the heating of a metal filament. This stream is subsequently accelerated and directed into a beam in an electrostatic field. [52–54] Secondary electric and magnetic fields are used to further focus and manipulate the beam. With the electron beam focused on the material ingot in the crucible, the material evaporates into a vapor plume, filling the inside of the chamber. [54] The substrate to be coated is held at the top of the chamber, with the side of interest facing downwards at the vapor plume. The material vapor condenses on the substrate surface (and all other surfaces within the chamber), thereby creating a thin film coating. By adjusting the power of the electron beam, and thereby the rate of material vaporization, deposition rate can be controlled. [55] The entire process is carried out under a high vacuum on the order of $10^{-5}torr$. A Sloan 8kV Electron-Beam Evaporator in the MIT Microsystems Technology Laboratory's Exploratory Materials Laboratory (EML) was used.

Typical deposition rates ranged from $1Å/s$ to $1.5Å/s$.

Figure 4-8: Sloan 8kV Electron Beam Evaporator.

4.2.5 Photolithography

Post features - used to control roughness - are created on heater surfaces through a photomasking process using the light sensitive photoresist SU-8. Commercially available in a variety of viscosities, SU-8 is epoxy based photoresist, well suited for high aspect ratio features with near vertical sidewalls. [56] The viscosity grade SU-8 2015 was used in this investigation. Different viscosity SU-8 will result in different layer thicknesses during spinning and charts of film thickness as a function of spin speed and duration are available from vendors.

First, the substrate is dehydrated by placing it on a hot plate at $150°C$ for a minimum of ten minutes. Next, the substrate surface is coated with SU-8 via a spinning process. During coating, SU-8 is deposited on the substrate with a pipette and care must be taken to prevent bubble formation in the photoresist layer. Substrates are held on a vacuum chuck. Spinning begins at $500RPM$ and ramps to at $3000RPM$ over ten seconds. It is then held at $3000RMP$ for thirty seconds. The soft start followed by a ramp to the target speed prevents shearing of the photoresist layer, which can alter the layer thickness. The layer thickness created during this initial coating will be the resulting height of the final post features.

Next, the substrate is soft baked, typically at $95°C$ for four minutes, on a hot place. The photoresist side is placed facing upwards and it is important that there is uniform contact between the entire back surface of the substrate and the hot plate. This will ensure even heat transfer through the substrate, curing the entire photoresist layer equally.

Following the soft bake phase, the substrate is masked and exposed. This step creates the actual feature pattern on the heater surface. SU-8 is a negative photoresist, implying that exposure to UV light in the $300nm$ to $400nm$ wavelength range will cause the the photoresist to cure. Therefore, a negative mask is employed. A soda lime glass mask is used and made nominally opaque by a chromium coating. The desired post locations are transparent locations in the coating. A Karl Suss MA4 mask aligner in the EML is utilized for the exposure process. The photomask is held in the machine via vacuum suction and the substrate is placed directly below it, with the photoresist coated side facing upwards. The machine is operated in hard contact mode, meaning that that substrate is forced into contact with the mask via an air jet prior to exposure. This minimizes shadowing effects during exposure. UV light exposure lasts for approximately thirty seconds, during which, a strong acid is formed in the exposed photoresist regions. [56]

After exposure, the substrate is post baked on a hot plate at $95°C$ for four minutes. Post exposure baking allows for acid-catalyzed thermal cross-linking of the photoresist regions exposed during the previous step. The cross-linked epoxy regions are quite durable, permanent features. [56] Again, it is critical for there to be uniform contact between the substrate surface in the hot plate.

Finally, the unexposed photoresist must be stripped from the substrate surface. The heater is placed back on a vacuum chuck and spun at low speeds (around $500RPM$). A propylene glycol monomethyl ether acetate (PM acetate) developer is sprayed onto the spinning substrate, removing the unexposed SU-8. Additionally, intermittent sprays of isopropenyl help to carry the photoresist off the surface.

In summary, the post fabrication process is as follows:

1. Dehydrate heater on hot plate at 150° for at least ten minutes.

2. Deposit SU-8 2015 on center of heater surface using pipette.

3. Spin starting at $500RPM$ and ramp up to 3000 RPM over ten seconds. Then maintain $3000RPM$ for thirty seconds.

4. Prebake at 95° on hot plate for three minutes.

5. Expose in mask aligner using a hard contact against the mask for thirty seconds at $200\frac{200mJ}{cm^2}$.

6. Post-bake at 95° on hot plate for three minutes.

7. Develop using PM-Acetate and isopropenyl, while spinning at $500RPM$ (usually for around forty to fifty seconds).

The remaining features have the height of the initial SU-8 layer thickness and the dimension and spacing of the mask pattern.

4.3 Feature Verification

Following fabrication, heater surfaces must be analyzed to confirm the desired surface characteristics. Of specific interest is the characterization of the roughness, porosity, wettability, and topography of any surface features. Additionally, different imaging techniques are useful for gaining insight into the exact nature of heater surface. The characterization techniques described are largely non-destructive and are typically employed prior to pool boiling testing. In some instances, the heater surface is characterized after a period of boiling in order to verify the integrity of the surface features through the pool boiling test regime.

4.3.1 High Resolution Scanning Electron Microscope

Surface features are inspected using a JEOL NeoScope JCM-5000 scanning electron microscope (SEM) in the MIT MTL, which can be seen in Figure 4-9.

The SEM allows for visualization of surface features such as microposts and microspheres. The unit is operated in low voltage (5kV) and low current modes. Because the substrates and features being imaged are not conductive, a thin layer ($\approx 10nm - 20nm$) of gold is deposited on the surface via a sputtering process. This layer is kept thin to ensure it conforms

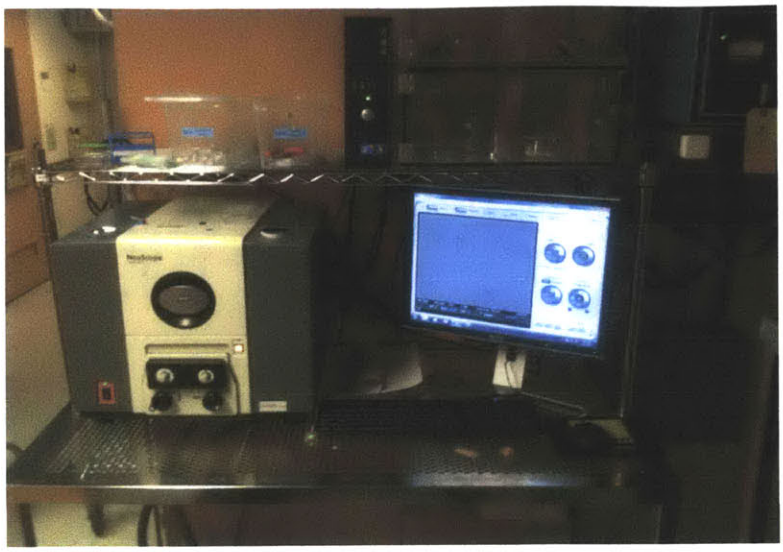

Figure 4-9: JEOL NeoScope JCM-5000 Scanning Electron Microscope used for feature identification.

to the underlying topography and does not fill in any pores. The upper gold layer is electrically connected to the SEM with a thin strip of electrically conductive carbon tape. These observation surfaces are not tested in the PBF, but rather are prepared only for imaging.

4.3.2 Contact Angle Measurement

Contact angle measurements are made using a KSV Instruments CAM 101, as seen in Figure 4-10. The sample is held in front of a light source and imaged with a CCD camera, which is connected to a computer with an image analysis software. The static contact angle is measured by depositing a single water droplet on a heater surface with syringe, during which around 100 frames are captured at a rate of 48 frames per second. During video analysis, the point at which the droplet first engages the surface is determined and video is subsequently moved ahead 0.5 seconds. At this point, the software package is used to determine the angle made between the surface and the bubble. Two measurements are made; one on for each side of the bubble. These angles should be in good agreement and the average of the two is reported. At least five static contact angle measurements are taken at different areas on the surface.

The advancing contact angle is measured by inserting the syringe needing into a static

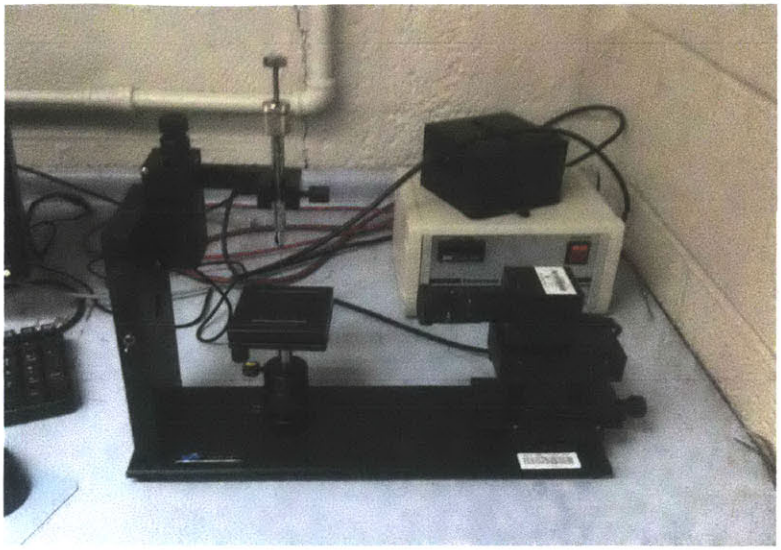

Figure 4-10: KSV Instruments CAM 101 used for making contact angle measurements.

droplet already on the surface and adding water until the vapor/liquid/surface contact line begins to move. The advancing contact angle is the angle made by the surface and the bubble immediately before the contact line moves. The receding contact angle is measured by also inserting a syringe needle into a static droplet already on the surface. However, in this case, water is removed until the vapor/liquid/surface contact line moves inward. The receding contact angle is measured immediately before the contact line begins to move.

4.3.3 Stylus Contact Profilometer

The Dektak 150 Surface Profiler is a stylus profilometer, which scans a stylus probe along a surface to measure roughness and characterize surface features. The stylus is placed in contact with the heater surface and then scanned in a straight line to capture surface characteristics. Any surface topography will cause a vertical displacement of the stylus, which is registered by the data acquisition software. The stylus tip is a hemisphere with a radius of $12.5\mu m$ and a vertical resolution of 1Å. [57] A typical scan length is $2mm$. For each heater at least five scans are recorded at different locations to accurately characterize the surface.

From these scans, the Dektak 150 calculates a variety of surface parameters, including different roughness values. For each surface, the average feature height, R_a roughness and R_z roughness are reported. R_z roughness is calculated as specified by Deutsche Institut fuer

Normung (German Institute for Standardization) standard DIN 4768/1. [57]

4.3.4 Spectroscopic Ellipsometer for Porosity Measurement

Spectroscopic ellipsometry is a method for measuring the polarization of many different wavelengths of light after reflection off of a surface. From these measurements, it is possible to determine the thickness and refractive index of a surface coating. Additionally, spectroscopic ellipsometry can offer insight into the porosity of a surface. This is accomplished by filling the pores with different mediums and comparing the refractive indices of the measurements made with different mediums. [24, 42] For example, two often utilized mediums are air and ethanol. A measurement is first made with the porous surface in the ambient environment. Next, the pores are flooded with ethanol, and the measurement is repeated. Using the rule of mixtures, the volume fraction of the pores can be calculated as [42],

$$p = \frac{n_{surface,ethanol} - n_{surface,air}}{n_{ethanol} - n_{air}} \tag{4.1}$$

Where, p is the porosity, $n_{surface,ethanol}$ and $n_{surface,air}$ are the refractive indices of the surface in ethanol and air, and $n_{ethanol}$ and n_{air} are the refractive indices of pure ethanol and air, respectively. Typically, when analyzing a porous surface, the optical properties at $620nm$ wavelength were used. Measurements are made on a J.A. Woolam Co. INC model XLS-100, located in the MIT Institute for Soldier Technologies.

4.4 Heater Testing

4.4.1 Heater Preparation

Prior to mounting a heater in the Pool Boiling Facility (PBF), it must be prepared with electric leads. To prevent corrosion of the electrodes, the ITO-Sapphire heater is mounted in the PBF with the electrode pads facing downwards, thus isolated from the water bath. As such, the active portion of the heater is the $1cm$ by $2cm$ region bounded by the silver pads, on the bare sapphire side of the heater.

First, the active heater region on the ITO side of the heater (non-boiling) is thoroughly cleaned, with any deposited thin film removed. During testing, the submerged heater surface is imaged through this backside surface. Therefore, cleanliness is important for optical clarity. Cleaning is performed with deionized water and ethanol rinses and gentle scrubbing with clean cotton swabs. The heater is dried in a stream of ultra-pure nitrogen. Additionally, any thin film covering the silver pads is removed with a cotton swab. Later electric leads are attached to the silver electrode pads with a conductive silver epoxy. Any film or debris on the silver pads can inhibit the mechanical bond between the epoxy and the silver pad, causing the leads to detach during testing.

Once the back side of the ITO-sapphire heater has been cleaned, the heater is mounted on the end of a borosilicate square tube, with the non-ITO (patterned) side of the heater facing into the tube. Prior to assembly, the square tubing is also cleansed with deionized water. The borosilicate square tube (Vitrocom S-145) is a $45mm$ square tube with $2mm$ wall thickness, and is cut to approximately $152mm(6in)$. While the borosilicate tube is held in a custom made assembly jig, the heater is adhered to the end of the tube with silicone sealant, forming a watertight joint. The purpose of the borosilicate tube is to create an isolation cell for the deionized water test fluid, separating it form the surrounding isothermal bath. Thus, the heater surface is protected from any contaminants which many be present within the PBF.

Finally, 16 AWG wire electric leads are adhered to the silver electrode pads with a silver filled epoxy. While the wire lead is held in place by the assembly jig, silver epoxy is precision deposited with a syringe. It is important that epoxy not spill onto the active heater area, as it can degrade the optical quality of the imaging during testing. The epoxy is allowed to cure for twenty four hours before the test is initiated. Two heater leads epoxied to the ITO-sapphire heater are presented in Figure 4-11 (note, this heater is not on the borosilicate tube).

4.4.2 Pool Boiling Facility

Located in MIT's Reactor Thermal Hydraulics Laboratory, the PBF has been utilized by prior investigations, benchmarking its performance. [24,58] A schematic detailing the system

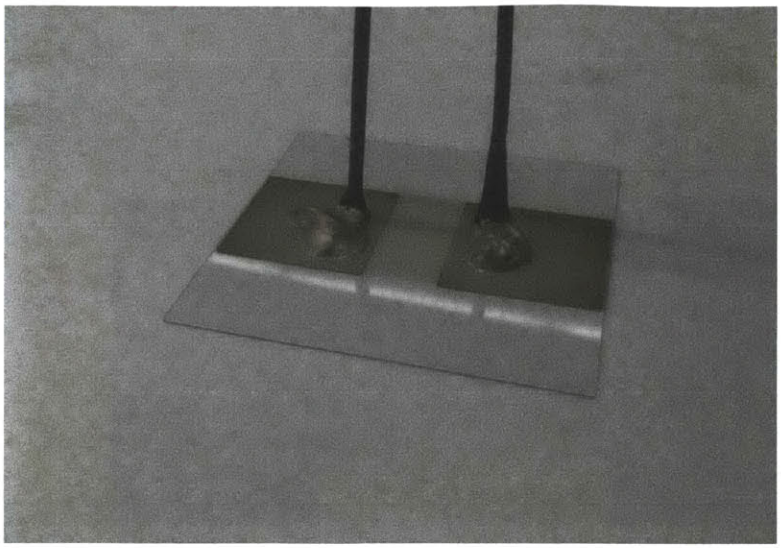

Figure 4-11: Electrical leads attached to ITO-sapphire heater.

layout can be see in Figure 4-12. The aluminum facility consists of an outer isothermal bath and an inner bath. However, the water surrounding the actual heater surface is further isolated from these two baths by the borosilicate tubing. In the center of the inner bath bottom is a square through hole, directly above which the ITO-sapphire heater is mounted.

A custom cut square silicone gel gasket is placed on the heater, around the wire leads. The entire heater unit (ITO-sapphire heater, wire leads, borosilicate tube, and silicone gasket) is lowered into the PBF. The wire leads are routed out the bottom of the PBF, with the silicone gasket forming a watertight seal between the ITO-sapphire heater and the PBF floor. The inner most isolation cell is filled with deionized water. A thin sheet of Viton is placed on top of the borosilicate tube to prevent water loss from splashing during boiling (though this sheet is well vented to the ambient environment). A plastic bracket and two long bolts are used to secure the borosilicate tube in place, gently compressing the silicon gasket on the PBF floor.

The outer isothermal baths are filled with regular water (approximately 3 gallons) and brought to saturation using a 1500W cartridge style heater. The electric leads from the heater are connected to a power supply (Electronic Measurements Inc. TCR Power Supply). A data acquisition system (Agilent Technologies 34980A) is also connected to the circuit to monitor power input and thus calculate heat flux. Voltage is monitored directly and current

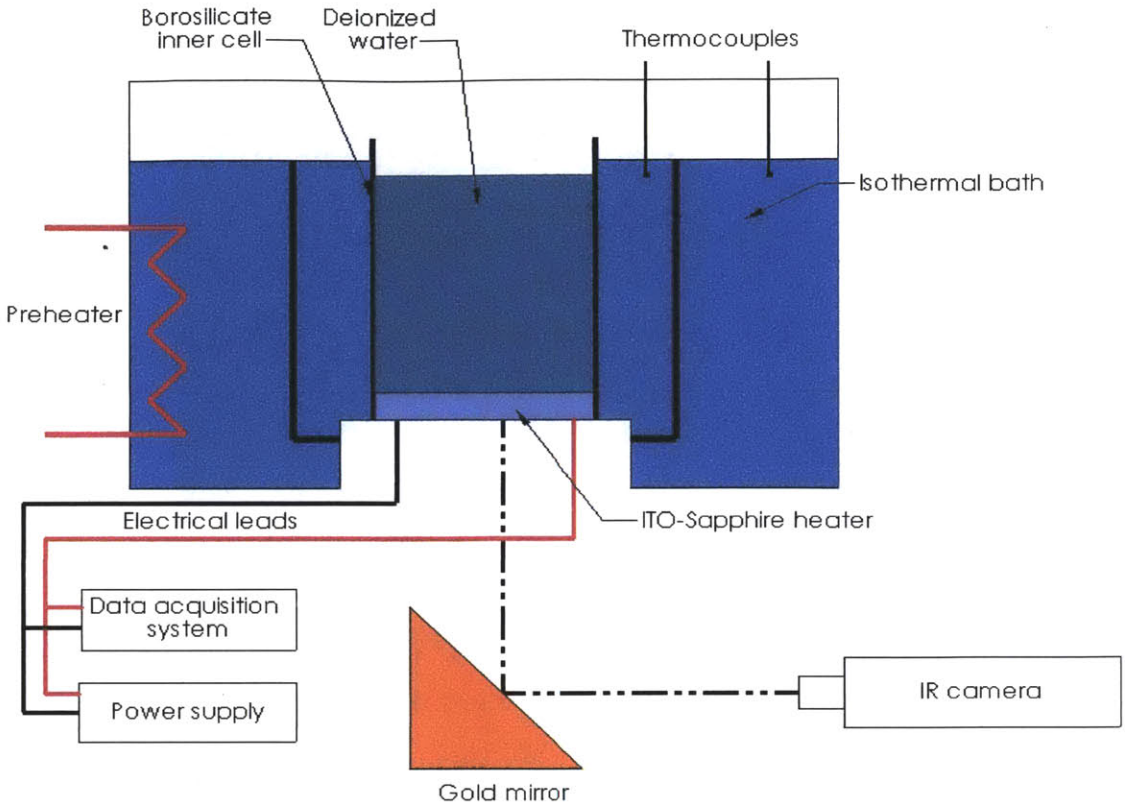

Figure 4-12: PBF layout. Note, some minor components (e.g. gaskets) have been omitted for clarity.

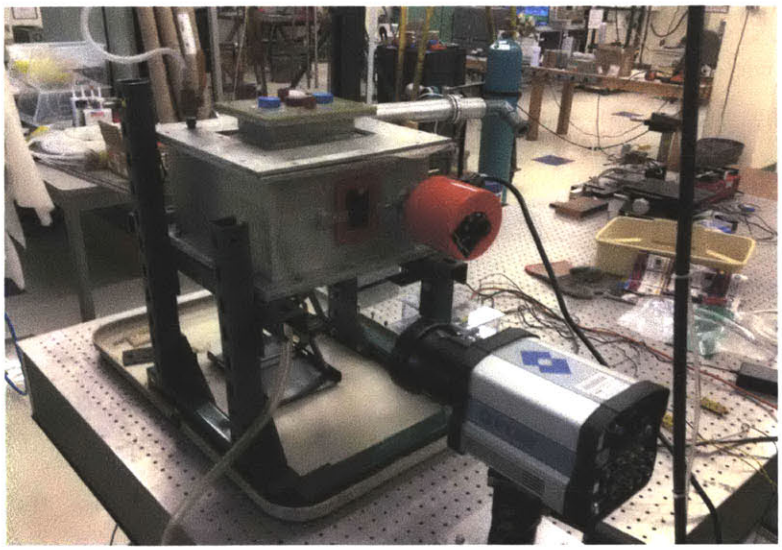

Figure 4-13: PBF with IR camera setup.

is measured with a shunt resistor, allowing power to be calculated. Knowledge of the active heater's area further allows for the determination of heat flux.

$$q'' = \frac{P}{A_{activeheater}} = \frac{V \times I}{A_{activeheater}} \tag{4.2}$$

Where q'' is the heat flux, P is power, V is voltage, I is current, and $A_{activeheater}$ is the area of the active heater. Additionally, the data acquisition system has thermocouple inputs to monitor the bulk water temperature in the bath.

Located directly beneath the heater is a 45° gold mirror on a scissor stage. To the side of the PBF is a FLIR SC6000 infrared (IR) camera, which allows for the temperature measurement over the entire active heater. The gold mirror allows the side mounted IR camera to image the heater surface from beneath. The ITO film is not IR-transparent and thus the surface temperature profile on the back side of the sapphire (non-water side) is registered by the IR camera (assuming negligible temperature gradient through the thin ITO layer). As such, the temperature on the heater surface in contact with the water is calculated to account for the temperature gradient in the appreciably thick sapphire. While the IR videos have some loss of clarity due to imaging through the ITO film, they adequately register the behavior of any patterns on the surface and offer insight into their performance. Typically, 2000 frames are captured at $1000hz$ in a given IR capture. A MATLAB script is used to determine the average spatial and temporal temperature of the heater surface from the video. IR data is collected at different heat fluxes and the combination of the power supplied and the IR temperature data is used to to construct a boiling curve. The heat flux is continuously increased in discrete steps until the achievement of CHF, at which point the heater typically fails catastrophically. A characteristic heating scheme, demonstrating the heat flux steps can be seen in Table 4.3. Each heater is only used for a single test.

Start→0→0.5→1→2→5→7.5→10→12→15→20→25→30→40→50→60→70→80→90↓
↓700←600←500←470←430←400←370←330←300←270←230←200←170←130←100
800→900→1000→1100→1150→1200→1250→1300→**...CHF**

Table 4.3: Characteristic heating steps. Note: heat flux steps reduce in size as anticipated CHF is approached. All values in $\frac{kW}{m^2}$.

4.5 Data Reduction

4.5.1 IR Signal Calibration

During PBF testing, a K-type thermocouple is adhered to the bottom center (ITO side) of the active heater area. Additionally, an area of the active heater, not covered by the thermocouple or adhesive tape is imaged with the IR camera. Starting while the surface and water bath are heating up at around $95°C$, thermocouple and IR measurements are simultaneously taken at discrete intervals. The thermocouple measures the surface temperature in degrees Celsius, while the number of pixel counts in a selected region is registered by the IR camera and its accompanying ExamineIR software. This is continued to a surface temperature of around $115°C$. From this series of measurements, it is possible to linearly relate the number of pixel counts with surface temperature, with a conversion ratio, CR. This relationship takes the form,

$$T_{lower} = CR \times (Counts) + offset \tag{4.3}$$

The offset is simply the y-intercept for the this linear relationship. Once this calibration is obtained, the thermocouple is removed from the surface, to allow IR imaging of the entire active heater area. This calibration step is performed periodically to ensure accurate data reduction.

4.5.2 IR Signal Analysis

Following the PBF testing, for each heater, there is an IR video at each discrete heat flux measured. During a given test thirty to forty measurements are taken. The exact number varies from surface to surface, depending on CHF. The videos are exported in the Flexible Image Transport System (FITS) format. This file type allows the videos to be loaded into MATLAB, where they are analyzed.

Using a MATLAB routine, known as the FITS Analyzer and developed by *Phillips 2011*, the average surface temperature can be determined at each heat flux step. The user selects the bounds of the active heater area in the user interface of the FITS Analyzer. This area

is clearly discernible from the surrounding heater based on the sharp temperature contrast. Once the active heater area is selected, the program iterates through all the IR videos collected for a given heater. In each instance, the program determines the average number of counts, both spatially across the active heater area and temporally through the IR video. The end result is an average count value for each heat flux.

A separate MATLAB routine is used calculate the surface temperature at each heat flux level. First, the count values from the FITS Analyzer are converted to temperature values. The slope of this linear relationship is already defined by the conversion ratio. The offset of this equation is determined by evaluating this relationship at a heat flux of $0\frac{kW}{m^2}$. As no power is flowing through the heater, the surface temperature is assumed to be equal to the equilibrium temperature of the bath. The equilibrium temperature, $T_{equilibrium}$, is the bath temperature achieved by the cartridge preheater. Here, the equilibrium temperature was about $99.5°C$. Therefore, the offset value is determined as,

$$offset = T_{equilibrium} - CR \times (Counts_{at0\frac{kW}{m^2}}) \tag{4.4}$$

With the offset determined, it is then possible to calculate the temperature of the bottom ITO surface using Equation 4.3. It is then necessary to calculate the temperature of the sapphire boiling surface by considering the heat conduction through the substrate.

Considering the sapphire as a thermal circuit, the temperature profile through the substrate can be determined through a simple heat conduction consideration. Here, the thermal resistance of the ITO layer is considered negligible because of its relatively small thickness compared to the sapphire (for reference, the temperature drop across the ITO layer at $1500\frac{kW}{m^2}$ is just $0.012°C$). The thermal circuit of the sapphire heater is presented in Figure 4-14, where $R_{sapphire}$ is thermal resistance of the sapphire, $t_{sapphire}$ is the thickness of the sapphire, T_{lower} is the temperature on the ITO side of the heater, and T_{upper} is the temperature on the upper sapphire side of the heater.

The thermal resistance of the sapphire can be calculated using the sapphire thermal conductivity, $k_{sapphire}$, as

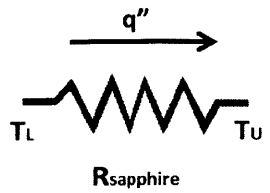

Figure 4-14: Thermal circuit accounting for conduction through sapphire substrate.

$$R_{sapphire} = \frac{t_{sapphire}}{k_{sapphire}} \tag{4.5}$$

Where $t_{sapphire}$ is the thickness of the sapphire heater and $k_{sapphire}$ is the sapphire thermal conductivity. The upper and lower temperatures of the sapphire heater can be related using the heat flux, q'' and the thermal resistance as,

$$T_{upper} = T_{lower} - q'' \times R \tag{4.6}$$

Therefore, the MATLAB program calculates the sapphire (wetted) side surface temperature at a given heat flux as,

$$T_{upper} = CR \times (Counts) + offset - q'' \frac{t_{sapphire}}{k_{sapphire}} \tag{4.7}$$

The resulting average upper surface temperatures are plotted against the heat flux values to create boiling curves for each heater surface.

4.6 Uncertainty Analysis

As with any experimental apparatus, it is important to consider the uncertainty in the system. Fortunately, the PBF has been utilized by numerous previous ingestions, which have characterized the measurement uncertainty. *Gerardi (2009)* determined the heat flux uncertainty for the facility to be less than 2%. [58] This calculation remains valid for this investigation as the methodologies are similar. Additionally, *Gerardi (2009)* determined the effect of radial conduction in the heater to be negligible. [58]

Phillips subsequently characterized the uncertainty associated with the temperature mea-

surement. As described previously, the temperature is measured on the bottom of the sapphire heater, but boiling occurs at the top. The temperature profile is calculated through the heater, where variance in heater thickness can affect results. The thermocouple measurement uncertainty is 0.75%, as cited by the manufacturer. [59] The reported uncertainty for the temperature measurement of the SC6000 IR camera is 2%. [60] *Phillips (2011)* characterized the tolerance of the sapphire thickness and used the method of error propogation for multiplication of uncorrelated variables to obtain an uncertainty value. He established that at $175°C$, the temperature error is approximately 2.8%. [24] Full derivations for the uncertainty error of the PBF and data reduction can be found in. [24, 58]

Chapter 5

Separate Effect Investigation Preparation, Testing, and Results

The Separate Effect investigation provides keen insight into the effect of surface characteristics on CHF and HTC. The results allow comparisons to be drawn between heaters and for the isolation of the effect of specific surface features. As a baseline reference, the results of each heater surface can also be compared to the performance of an Uncoated Sapphire heater.

Before considering the performance of each specific heater surface, it is useful to present the overall CHF performance of all heater surfaces. This allows for a macro-understanding of their relative performance. CHF values for all heaters tested are presented in Table 5.1. For most heaters, CHF was determined to be the highest stable heat flux before catastrophic heater burnout. However, in the case of the smooth and rough hydrophobic porous heaters, the transition to film boiling occurred at extremely low heat flux. This allowed the heater to continue to operate in the film boiling regime for a substantial range of heat flux before heater burnout. In these cases, CHF and heater burnout must be distinguished, as indicated in Table 5.1. Additionally, measurements of the as fabricated surface parameters are presented in Table 5.2.

Pattern	CHF ($\frac{kW}{m^2}$)	Average CHF ($\frac{kW}{m^2}$)	St. Dev
Uncoated Heater 1	873	920	8.3%
Uncoated Heater 2	1032		
Uncoated Heater 2	920		
Uncoated Heater 3	986		
Uncoated Heater 4	799		
Uncoated Heater 5	885		
Uncoated Heater 6	947		
Smooth Non-porous Hydrophilic 1	1013	1009	10.3%
Smooth Non-porous Hydrophilic 2	904		
Smooth Non-porous Hydrophilic 3	1111		
Smooth Non-porous Hydrophobic 1	1114	968	17.8%
Smooth Non-porous Hydrophobic 2	791		
Smooth Non-porous Hydrophobic 3	1086		
Smooth Non-porous Hydrophobic 4	1082		
Smooth Non-porous Hydrophobic 5	769		
Smooth Porous Hydrophilic 1	1800	1617	10.9%
Smooth Porous Hydrophilic 2	1605		
Smooth Porous Hydrophilic 3	1446		
Smooth Porous Hydrophobic 1	38 (38)	34	11.8%
Smooth Porous Hydrophobic 2	30 (65)		
Smooth Porous Hydrophobic 3	35 (47)		
Rough Non-porous Hydrophilic 1	1007	1063	5.5%
Rough Non-porous Hydrophilic 2	1123		
Rough Non-porous Hydrophilic 3	1059		
Rough Non-porous Hydrophilic (1.98mm post pitch) 1	1049	1022	3.6%
Rough Non-porous Hydrophilic (1.98mm post pitch) 2	996		
Rough Non-porous Hydrophobic 1	1172	1067	15.3%
Rough Non-porous Hydrophobic 2	1150		
Rough Non-porous Hydrophobic 3	879		
Rough Porous Hydrophilic 1	1594	1590	7.0%
Rough Porous Hydrophilic 2	1700		
Rough Porous Hydrophilic 3	1478		
Rough Porous Hydrophobic 1	20-40 (815)	–	–
Rough Porous Hydrophobic 2	40-60 (700)		
Rough Porous Hydrophobic 3	20-40 (359)		

Table 5.1: CHF values for Separate Effect investigation. Note, values in parenthesis indicate heater burnout heat flux, if different from local CHF. For the Rough Porous Hydrophobic heaters, determination of CHF was somewhat subjective and thus a range of suspected CHF is presented.

Pattern	Roughness (μm)		Porosity (vol%)	Contact Angle (degrees)		
	R_a	R_z		Static	Adv.	Rec.
Uncoated Heater (reference)	0.0033	0.00954	0%	74.7	81.7	47.7
Smooth Non-porous Hydrophilic	0.00416	0.02506	0%	< 5	-	-
Smooth Non-porous Hydrophobic	0.00596	0.03569	0%	111.6	130.9	81.3
Smooth Porous Hydrophilic	0.07	0.91	49%	< 5	-	-
Smooth Porous Hydrophobic	0.07	0.91	49%	137.5	160.3	97.5
Rough Non-porous Hydrophilic	2.66	14.96	0%	< 5	-	-
Rough Non-porous Hydrophobic	2.59	15.22	0%	112.6	132.3	85.8
Rough Porous Hydrophilic	2.23	14.08	49%	5	-	-
Rough Porous Hydrophobic	1.96	13.25	49%	139.8	149.4	103.6

Table 5.2: Measured surface parameters on fabricated heaters.

5.1 Uncoated Sapphire Surface

5.1.1 Surface Analysis

As received, the ITO-sapphire heaters are nano-smooth, non-porous, and have a average static contact angle of 74.7°. The uncoated heater was tested such that the active heater area was on the bare sapphire side. This provides a good baseline reference case, against which other heater surfaces can be compared. The advancing, receding, and static contact angles of the uncoated heater were measured and are compiled in Table 5.3.

Roughness measurements were made with the Dektak stylus profilometer. The average roughness was measured to be $R_a = 0.00330 \mu m$ and $R_z = 0.00954$ and a list of profilometer measurements is presented in Table 5.4. From these results, it is clear that the as received heaters are extremely smooth surfaces.

Measurement	Contact Angle (Degrees)	Average Contact Angle (Degrees)	Standard Deviation
Static 1	83.7	74.7	8.55%
Static 2	68.8		
Static 3	66.6		
Static 4	75.1		
Static 5	79.4		
Advancing 1	78.5	81.7	6.66%
Advancing 2	79.0		
Advancing 3	74.9		
Advancing 4	88.1		
Advancing 5	88.2		
Receding 1	42.9	47.4	5.73%
Receding 2	43.8		
Receding 3	58.4		
Receding 4	44.3		
Receding 5	47.8		

Table 5.3: Contact angle measurements for Uncoated Sapphire heater.

Scan	$R_a(\mu m)$	$R_z(\mu m)$
Scan 1	0.00392	0.0084
Scan 2	0.00389	0.01275
Scan 3	0.0025	0.00849
Scan 4	0.00302	0.00816
Scan 5	0.00317	0.0099
Average	0.00330	0.00954
St. Dev	18.36%	20.12%

Table 5.4: Roughness measurements for Uncoated Sapphire heater.

5.1.2 PBF Testing and Discussion

Pattern	CHF ($\frac{kW}{m^2}$)	Average CHF ($\frac{kW}{m^2}$)	St. Dev
Uncoated Heater 1	873	920	8.3%
Uncoated Heater 2	1032		
Uncoated Heater 3	920		
Uncoated Heater 4	986		
Uncoated Heater 5	799		
Uncoated Heater 6	885		
Uncoated Heater 7	947		

Table 5.5: CHF Values for Uncoated Sapphire heaters.

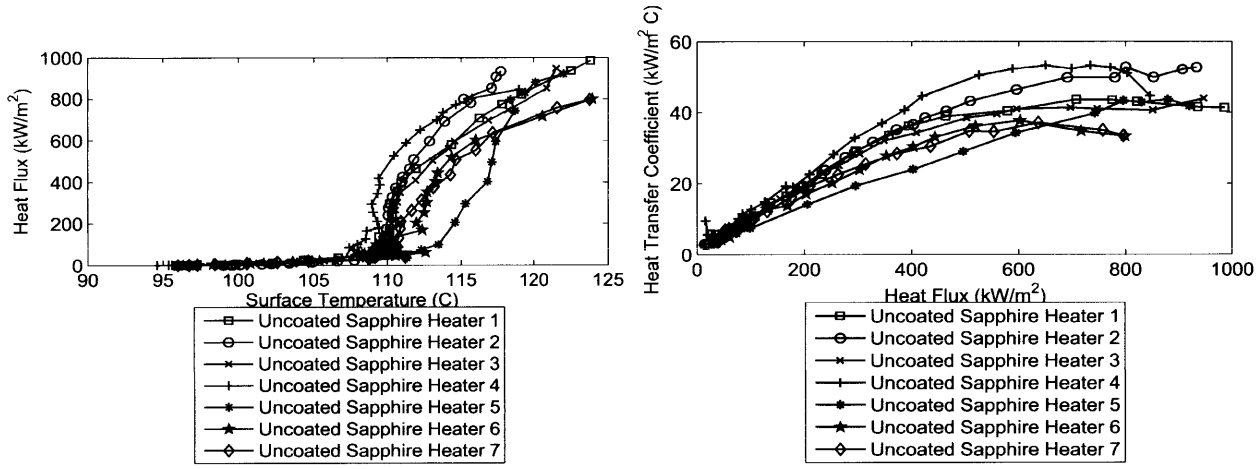

(a) Boiling Curve

(b) Heat Transfer Coefficient

Figure 5-1: Boiling Curve and Heat Transfer Coefficient for Uncoated Sapphire Heater.

Previously, *Phillips (2011)* tested the benchmark performance of five Uncoated Sapphire heaters (Heaters 3-7). Here, two additional heaters (Heaters 1 and 2) were tested to ensure agreement with previously acquired data. The average CHF value for the Uncoated Sapphire heaters was $920\frac{kW}{m^2}$ with a standard deviation of 8.3%. The boiling curves created by the Uncoated Sapphire heaters provides a common reference against which to compare the performance of the subsequent heater surfaces. The boiling behavior of the Uncoated Sapphire heater can be visualized from Figure 5-1.

A few perspectives can be gained from the benchmark testing of the Uncoated Sapphire heaters. First, the CHF and boiling curve results of this investigation are in agreement with

those of *Phillip's* work. This confirms the ability to draw comparisons of tests completed in the two projects (as should be true, given that procedures and experimental apparatus utilized are similar). Additionally, the variability in the boiling curves and CHF values offers insight into the natural variability of the PBF and test procedure. In any boiling process, there will be a partly stochastic process. Testing multiple Uncoated Sapphire heaters offers an understanding of this natural variability, which can be used as a reference when analyzing the performance of patterned surfaces. However overall, the boiling curves were grouped relatively tightly. Additionally, a standard deviation of 8.3% for the CHF values implies a repeatable testing procedure.

5.2 Smooth Non-porous Hydrophilic Surface

5.2.1 Surface Fabrication

The only surface preparation required for the Smooth Non-porous Hydrophilic heaters was to deposit a thin hydrophilic layer on the surface. Using the electron beam procedure described in Section 4.2.4, a $20nm$ layer of intrinsically hydrophilic SiO_2 was deposited at an average rate of $1.3AA/s$. The SiO_2 layer deposited by this vapor deposition technique conforms to the surface topology and induced no further roughness or porosity than that already present on the underlying surface.

In summary, the fabrication process for the Smooth Non-porous Hydrophilic heaters was a single step:

1. Deposit $20nm$ thick SiO_2 layer via electron beam.

5.2.2 Surface Analysis

The resulting hydrophilic surface was highly wetting, with a static contact angle of less than $5°$ after $0.5s$ Because of the super hydrophilicity of this surface, it was not possible to characterize the advancing and receding contact angles. The results of the static contact angle measurements are presented in Table 5.6 and can be visualized in Figure 5-2.

Measurement	Contact Angle (Degrees)
Static 1	$< 5°$
Static 2	$< 5°$
Static 3	$< 5°$
Static 4	$< 5°$
Static 5	$< 5°$

Table 5.6: Contact angle measurements for Smooth Non-porous Hydrophilic heater.

Figure 5-2: Static contact angle measurement for Smooth Non-porous Hydrophilic surface.

The surface roughness of these heaters was characterized with the Dektak Surface Profiler. Five scans, each $2mm$ long, were made and the results of these measurements are presented in Table 5.7. On average, R_a and R_z were found to be $0.00416\mu m$ and $0.02506\mu m$, respectively. Clearly, even after SiO_2 deposition, this surface is still extremely smooth. In comparison to the rough surfaces later tested, the R_a and R_z values of this surface are three orders of magnitude less.

Scan	$R_a(\mu m)$	$R_z(\mu m)$
Scan 1	0.00383	0.02420
Scan 2	0.00405	0.03327
Scan 3	0.00413	0.02358
Scan 4	0.00429	0.02333
Scan 5	0.00449	0.02109
Average	0.00416	0.02509
St. Dev	5.98%	18.81%

Table 5.7: Roughness measurements for Smooth Non-porous Hydrophilic heater.

5.2.3 PBF Testing and Discussion

Pattern	CHF ($\frac{kW}{m^2}$)	Average CHF ($\frac{kW}{m^2}$)	St. Dev
Smooth Non-porous Hydrophilic 1	1013	1009	10.3%
Smooth Non-porous Hydrophilic 2	904		
Smooth Non-porous Hydrophilic 3	1111		

Table 5.8: CHF values for Smooth Non-porous Hydrophilic heaters.

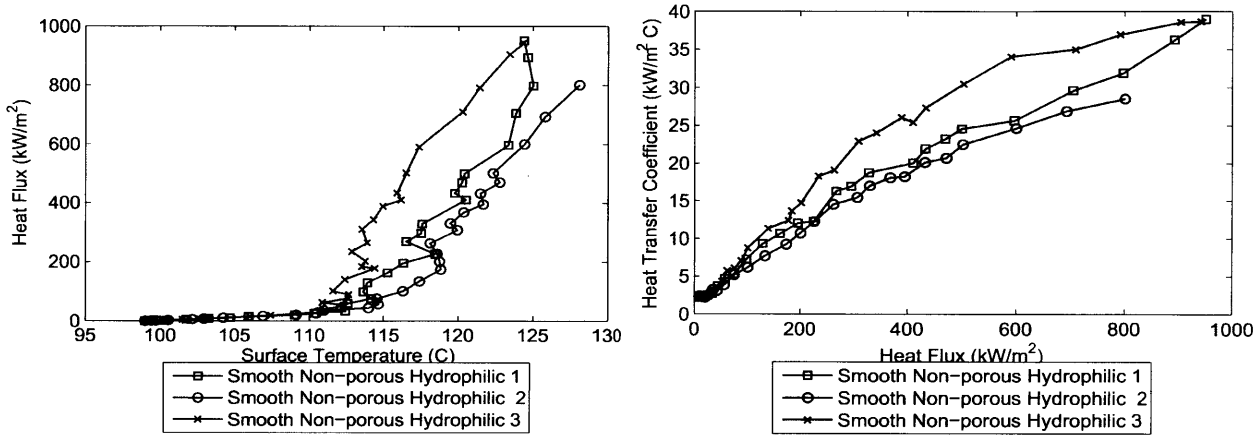

(a) Boiling Curve

(b) Heat Transfer Coefficient

Figure 5-3: Boiling Curve and Heat Transfer Coefficient for Smooth Non-porous Hydrophilic heaters.

While the Smooth Non-porous Hydrophilic surface had a significantly higher wettability than an Uncoated Sapphire heater, this surface did not realize significant CHF or HTC improvement. The average CHF value was $1099\frac{kW}{m^2}$ with a standard deviation of 10.25%. The boiling curves for this surface are presented in Figure 5-3. Initially, the lack of improvement over an Uncoated Sapphire heater was suspicious. It was hypothesized that the hydrophilic coating was being lost during pool boiling. However, static contact angle measurements of heater surfaces after pool boiling were around $15° - 20°$. That the surface was still hydrophilic confirmed that the SiO_2 layer was intact. Some loss of hydrophilicity is expected during testing as the surface was inevitibly contaminated as compared to its state after fabrication in a cleanroom. Additionally, a similar, thin SiO_2 layer was used by *Troung (2011)* in boiling experiments, which provides further validation that this type of material

layer can remain intact during testing.

Therefore, the hydrophilic coating had little effect on this smooth non-porous surface. This is surprising, given the popularity of hydrophilicity as a CHF enhancing mechanism. However, it seems that the extreme smoothness and lack of porosity dwarfed the potential benefits of the hydrophilic coating. With an extremely smooth surface, there was a distinct lack of nucleation sites on the heater surface. While the hydrophilic coating could help to rewet the surface, it seems that the lack of nucleation sites inhibited CHF enhancement. This is an important caveat to the traditional understanding of the effect of surface wettability on boiling performance. However, these test results should not lead one to conclude that hydrophilicity does not enhance CHF. Rather, the important understanding from these tests is that extremely smooth and non-porous surfaces are minimally affected by intrinsic wettability in terms of CHF.

5.3 Smooth Non-Porous Hydrophobic Surface

5.3.1 Surface Fabrication

No surface features were patterned on these heaters. Rather, only the intrinsic wettability was altered. A hydrophobic surface was created with a fluorosilane CVD process. However, as fluorosilane does not adhere well to bare sapphire, a thin SiO_2 layer was deposited first. The OH- groups of the SiO_2 layer provide binding sites for fluorosilane. Additionally, the fluorosilane CVD exposure time was increased to eight hours for these heaters. While shorter exposure times (on the order of thirty minutes) are adequate for fluorosilane deposition on porous surfaces, longer times are required for smooth surfaces. The wettability of the surface is highly sensitive to defects in the fluorosilane layer and long exposure ensures a uniform deposition. For reference, the static contact angle of this surface after a thirty minute fluorosilane exposure was only 97.1°. After eight hours of exposure, the static contact angle was increased to 111.6°. This level of hydrophobicity approaches the limit capable for a non-porous surface. Though others have been able to achieve contact angles as high as 130° on a smooth non-porous surface, the exotic techniques employed were not applicable to use

on the ITO-sapphire heaters. [61, 62] While this level of hydrophobicity is not at the level of the Smooth Porous Hydrophobic Surface (static contact angle of 137.5°), it still allows for approximate comparison between the surfaces. Additionally, this level of hydrophobicity provides a stark contrast to that of the Smooth Non-Porous Hydrophilic heater (static contact angle of $< 5°$).

In summary, the chronological fabrication steps for the Smooth Non-porous Hydrophobic heaters were:

1. Deposit $20nm$ thick SiO_2 layer via EB-PVD at a deposition rate of approximately $1.3Å/s$.

2. Deposit fluorosilane layer via CVD at $140°C$ for eight hours.

Because of suspected non-uniformity issues with the fluorosilane deposition on a smooth surface, additional heaters were fabricated and tested. A total of five Smooth Non-porous Hydrophobic heaters were examined, with all surfaces characterized and inspected to ensure that the surface characteristics met the specified standards.

5.3.2 Surface Analysis

The average static, advancing, and receding contact angles were measured to be 111.6°, 130.9°, and 81.3°, respectively. A summary of all contact angle measurements made on this heater surface can be see in Table 5.9. Images of the water droplets during the different contact angle measurements can be seen in Figure 5-4.

Surface roughness measurements were made with the Dektak Surface Profiler. The average R_a and R_z values were determined to be $0.00596\mu m$ and $.03569\mu m$, respectively. The results of the five surface profile scans made are presented in Table 5.10. While there is a higher standard deviation for these values, the absolute roughness values are still on the order of Angstroms and orders of magnitude below those of the rough series of heater surfaces. The increased variability in the surface scans is likely a result of slight non-uniformities in the fluorosilane coating.

Measurement	Contact Angle (Degrees)	Average Contact Angle (Degrees)	Standard Deviation
Static 1	108.6	111.6	1.78%
Static 2	111.6		
Static 3	110.2		
Static 4	113.3		
Static 5	114.1		
Advancing 1	137.6	130.9	2.78%
Advancing 2	131.1		
Advancing 3	126.8		
Advancing 4	129.1		
Advancing 5	129.8		
Receding 1	76.1	81.3	4.10%
Receding 2	80.1		
Receding 3	85.4		
Receding 4	84.9		
Receding 5	79.4		

Table 5.9: Contact angle measurements for Smooth Non-porous Hydrophobic heater.

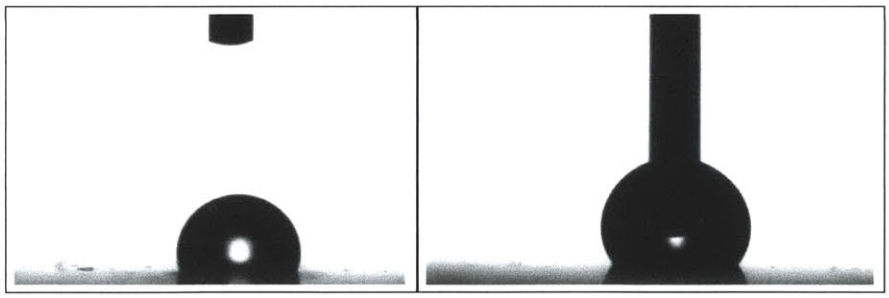

(a) Static Contact Angle (b) Advancing Contact Angle

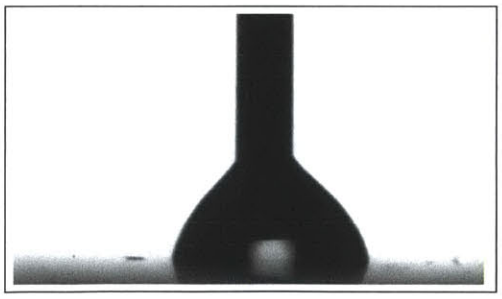

(c) Receding Contact Angle

Figure 5-4: Contact angle measurements for Smooth Non-porous Hydrophobic surface.

Scan	R_a(Å)	R_z(Å)
Scan 1	0.00459	0.02119
Scan 2	0.00511	0.01434
Scan 3	0.00523	0.0287
Scan 4	0.00683	0.06029
Scan 5	0.00803	0.05393
Average	0.00596	0.03569
St. Dev	23.99%	56.96%

Table 5.10: Roughness measurements for Smooth Non-porous Hydrophobic heater.

5.3.3 PBF Testing and Discussion

Pattern	CHF ($\frac{kW}{m^2}$)	Average CHF ($\frac{kW}{m^2}$)	St. Dev
Smooth Non-porous Hydrophobic 1	1114	968	17.8%
Smooth Non-porous Hydrophobic 2	791		
Smooth Non-porous Hydrophobic 3	1086		
Smooth Non-porous Hydrophobic 4	1082		
Smooth Non-porous Hydrophobic 5	769		

Table 5.11: CHF Values for Smooth Non-porous Hydrophobic heaters.

The Smooth Non-porous Hydrophobic heaters had CHF values also similar to the Uncoated Sapphire surfaces. The average Smooth Non-porous Hydrophobic CHF value was $968\frac{kW}{m^2}$, with a standard deviation of 17.8%. It was suspected that the hydrophobic coating would have detrimental CHF effects, as it inhibits liquid rewetting. As with the Smooth Non-porous Hydrophilic surfaces, here it was feared that the surface coating was being lost during pool boiling. However, contact angle measurements of heater surfaces after pool boing were in the range of $90° - 100°$. This confirms that hydrophoic fluorosilane coating was still intact on the surface. Additionally, the fluorosilane coating has been utilized by numerous other investigations with success in the past to create a hydrophobic surface. Five heaters were created and tested for this surface, as there was some concern about repeatability of the fluorosilane deposition on the smooth surface. However, as the boiling curves in Figure 5-5 illsutrate, all of the fabricated heaters performed in a relativley similar manner.

Again, the wettability transformation of the smooth, non-porous surface did not have a significant effect on the heaters' performance. It seems that the extreme smoothness

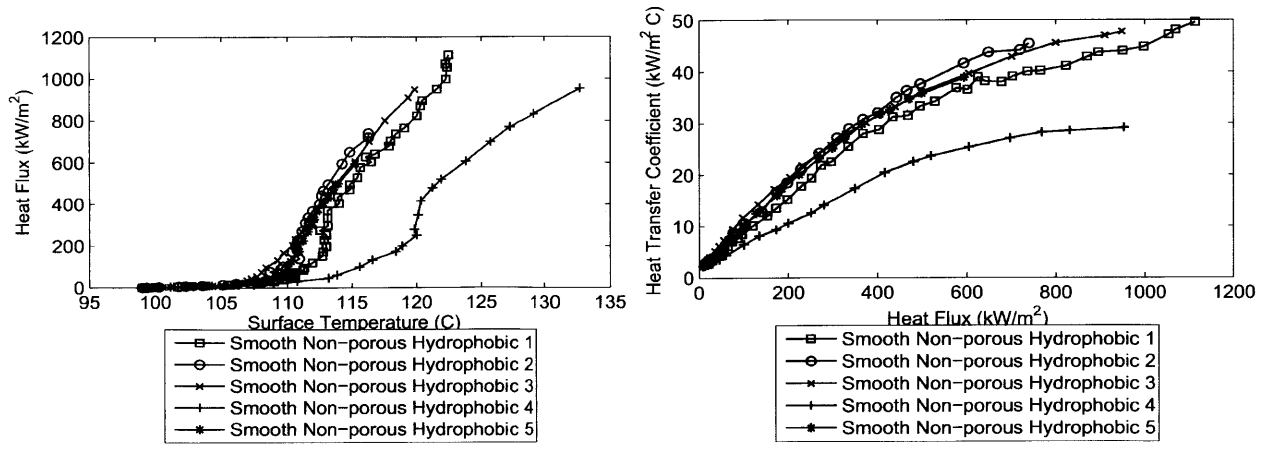

(a) Boiling Curve

(b) Heat Transfer Coefficient

Figure 5-5: Boiling Curve and Heat Transfer Coefficient for Smooth Non-porous Hydrophobic heaters.

and non-porosity again override the wettability affects. As is shown with subsequent tests, wettability does affect surfaces when porosity is present. Here, however, increasing the intrinsic hydropobicity of the surface alone had little effect.

5.4 Smooth Porous Hydrophilic Surface

5.4.1 Surface Fabrication

Porosity and hydrophilicity were created through the LBL procedure outlined in Section 4.2.1. SiO_2 particles with a diameter of $50nm$ were used and fifty bilayers were deposited. The porous hydrophilic surfaces are particularly susceptible to attracting surface contaminants from the ambient environment. Therefore, following the LBL deposition, the heaters were plasma cleaned. After this process, the LBL heaters were kept in a sealed container until mounted in the PBF for testing.

In summary, the chronological fabrication steps for the Smooth Porous Hydrophilic heaters were:

1. LBL deposition with $50nm$ SiO_2 particles for fifty layers.

2. Plasma cleaning.

5.4.2 Surface Analysis

The contact angle of the Smooth Porous Hydrophilic surface was measured twenty four hours after plasma cleaning and immediately before PBF testing. Plasma cleaning will temporarily transform any surface to hydrophilic, though this effect is short lasted. As a result, it is important to delay contact angle measurement until all temporary surface chemistry transformation has expired. This ensures that the contact angle measured is actually representative of the intrinsic wettability of the surface. The average static contact angle for this surface was measured to be $< 5°$, implying a super hydrophilicity.

Measurement	Contact Angle (Degrees)
Static 1	$< 5°$
Static 2	$< 5°$
Static 3	$< 5°$
Static 4	$< 5°$
Static 5	$< 5°$

Table 5.12: Contact angle measurements for Smooth Porous Hydrophilic surface.

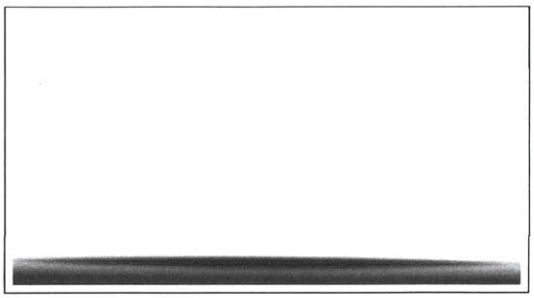

Figure 5-6: Static contact angle measurement for Smooth Porous Hydrophilic surface.

Phillips (2011) measured the thickness and porosity of an identical LBL surface using the spectroscopic ellipsometry technique described in Section 4.3.4. His characterization is presented in Table 5.13. [24]

The Smooth Porous Hydrophilic surfaces created in this investigation are identical to those measured by *Phillips* and his measurements are applicable to the surfaces tested here. The average porosity of the layer is 49%.

Similarly, *Phillips (2011)* used a confocal microscope to determine the roughness of this

Attribute	Value
Total Thickness (nm)	1360
Thickness of Each Multilayer (nm)	27
Thickness Standard Deviation	0.90%
Porosity	0.49
Porosity Standard Deviation	6%

Table 5.13: *Phillips'* porosity characterization of Smooth Porous Hydrophilic surface. [24].

type of heater surface. In these measurements, a full area of $128\mu mx128\mu m$ and a local characteristic spot of $30\mu mx30\mu m$ were imaged. The results of this analysis is presented in Table 5.14.

Attribute	Value
Global SRa (μm)	0.07
Local SRa (μm)	0.06
Global SRz (μm)	0.91
Local SRz (μm)	0.65

Table 5.14: *Phillips'* roughness measurements of Smooth Porous Hydrophilic surface. [24].

While the roughness resulting from the SiO_2 nanoparticles is appreciable compared to Uncoated Sapphire or any of the non-porous surfaces, it is still orders of magnitude less than the roughness imparted by the post features. As such, these heaters are still considered to be smooth in the terms of this investigation.

In addition to the roughness characterization by confocal microscope, this surface roughness was also analyzed with a stylus profilometer. The profilometer tip has a radius of $12.5\mu m$, which is larger than the anticipated pore size. Therefore, some aliasing occurred in this measurement. However, the results still offer an adequate upper limit of roughness and are in relatively good agreement with the confocal microscope measurements.

Finally, SEM images acquired by *Phillips (2011)* confirm the presence and packing of the SiO_2 nanoparticles. As seen in Figure 5-7, a distinct porous structure is created by the particles. [24]

Scan	$R_a(\mu m)$	$R_z(\mu m)$
Scan 1	0.14877	0.97651
Scan 2	0.16392	0.92705
Scan 3	0.13006	0.65539
Scan 4	0.10605	0.66749
Scan 5	0.13073	0.68364
Average	0.13591	0.78202
St. Dev	16.05%	19.98%

Table 5.15: Profilometer roughness measurements for Smooth Porous Hydrophilic heater.

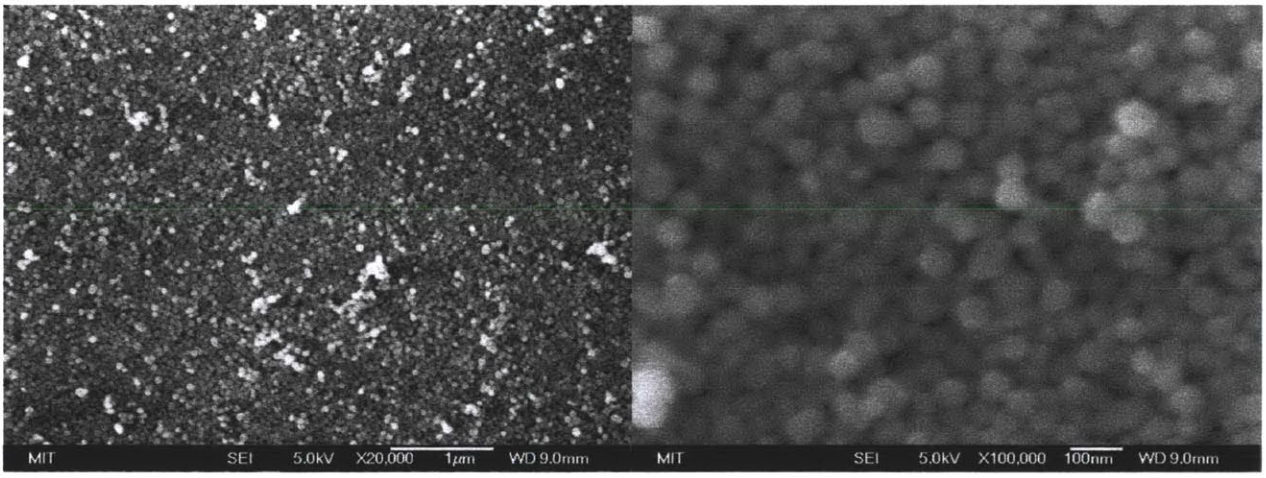

(a) 20,000X (b) 100,000X

Figure 5-7: SEM images of Smooth Porous Hydrophilic surface (acquired by *Phillips (2011)*) [24]

Pattern	CHF ($\frac{kW}{m^2}$)	Average CHF ($\frac{kW}{m^2}$)	St. Dev
Smooth Porous Hydrophilic 1	1800	1617	10.9%
Smooth Porous Hydrophilic 2	1605		
Smooth Porous Hydrophilic 3	1446		

Table 5.16: CHF values for Smooth Porous Hydrophilic heater.

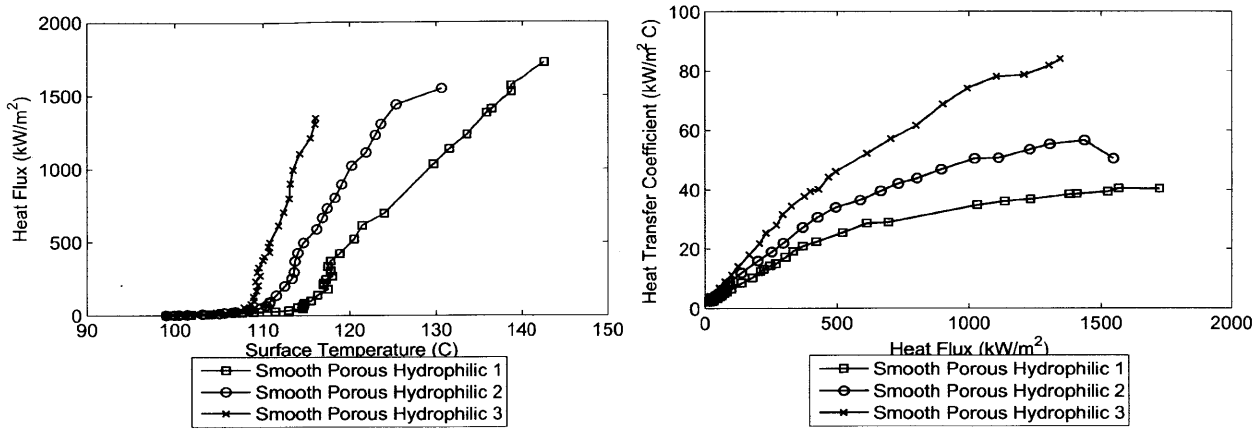

(a) Boiling Curve

(b) Heat Transfer Coefficient

Figure 5-8: Boiling Curve and Heat Transfer Coefficient for Smooth Porous Hydrophilic heaters

5.4.3 PBF Testing and Discussion

The Smooth Porous Hydrophilic heaters had the highest CHF values among all heater surfaces tested. The average CHF was $1617\frac{kW}{m^2}$ with a standard deviation of 10.9%. It seems that the combination of porosity and hydrophilicty is a very effective mechanism to enhance CHF. Interestingly, the HTC was not significantly heightened and more direct HTC comparisions are presented in Section 5.11. Additionally, while the CHF values were grouped as tightly as most other results in this investigation, the boiling curves for this surface are somewhat spread out. The three heaters tested were all fabricated simultaneously under identical conditions. This implies that there is a degree of variablility in the performance of a porous hydrophilic surface. This may be a result of naturally varying levels of pore interconnectedness on the surfaces. The pores and the pathways that connect them are created naturally by spherical packing during the LBL process. The manner in which the SiO_2 spheres assemble cannot be controlled. While the overall level of porosity remains around 50% for these surfaces, it might be the case that certain heaters have more efficient or prevalent pathways conencting the pores. This could result in more enhanced boiling performance and account for the variability in the Smooth Porous Hydrophilic boiling curves.

Regardless, this heater surface was particularly well performing and should be considered for more in-depth investigation and application. *Philips (2011)* tested similar surfaces and

also varied the pore size by using SiO_2 particles with different diameters ($7nm - 100nm$). [24] A summary of these results is presented in Table 5.17.

Pattern	CHF	Average CHF ($\frac{kW}{m^2}$)	St. Dev
7nm SiO_2 Particles 3	1107	1096	1%
7nm SiO_2 Particles 4	1085		
50nm SiO_2 Particles 1	1650	1583	5%
50nm SiO_2 Particles 2	1600		
50nm SiO_2 Particles 3	1500		
100nm SiO_2 Particles 2	1342	1382	6%
100nm SiO_2 Particles 4	1400		
100nm SiO_2 Particles 5	1490		
100nm SiO_2 Particles 6	1297		
20/50nm SiO_2 Particles 1	1640	1587	4%
20/50nm SiO_2 Particles 2	1600		
20/50nm SiO_2 Particles 3	1522		

Table 5.17: *Phillips' (2011)* CHF results after varying the particle size of Smooth Porous Hydrophilic Surfaces. The 20/50nm surface was comprised of a mixture of 20nm and 50nm SiO_2 particles. [24]

He found that pore size did not significantly affect CHF; however the surfaces with $50nm$ particles were slightly better performing than those with larger and smaller particles. The next steps for investigating a porous hydrophilic boiling surface are to consider surfaces with multiple layers of different pore sizes. Perhaps, small particles (nanoscale) could be used near the substrate to create high capillary wicking action and larger particles (microscale) could be deposited on top, to create nucleation sites on the same order of magnitude as is typically found in nature. Additionally, it will be important to consider mechanisms by which to make a more durable porous hydrophilic surface ready for deployment in industry.

5.5 Smooth Porous Hydrophobic Surface

5.5.1 Surface Fabrication

The fabrication of the Smooth Porous Hydrophobic heaters was similar to that of the Smooth Porous Hydrophilic heaters, with an extra wettability altering step at the end of the process. To induce porosity, the ITO-sapphire heaters were first prepared via an LBL process with

fifty layers of $50nm$ SiO_2 particles. However, as indicated previously, this results in an intrinsically hydrophilic surface. Therefore, the resulting surface was coated with a layer of fluorosilane via the CVD process described in Section 4.2.2. Because the porous surface is conducive to accepting the fluorosilane deposition, an exposure time of thirty minutes was adequate for uniform surface coverage. The fluorosilane monolayer conforms tightly to the surface, thus preserving the porosity of the LBL layer, while making the surface hydrophobic.

In summary, the chronological fabrication steps for the Smooth Porous Hydrophobic heater were:

1. LBL deposition with $50nm$ SiO_2 particles for fifty layers.

2. CVD of fluorosilane for thirty minutes.

5.5.2 Surface Analysis

Multiple static, advancing, and receding contact angle measurements were made on the porous hydrophobic surface. The porous hydrophobic surface exhibited the highest contact angle of the surfaces tested, with an average static contact angle of 137.5°. Additionally, the average advancing and receding contact angles were 160.3° and 97.5°, respectively. The results of these measurements are presented in Table 5.18, along with images of each type of contact angle measurement in Figure 5-9. This increase in contact angle can be attributed to the Cassie effect working in combination with the intrinsic hydrophobicity of the surface.

The fluorosilane deposited on the heater surface forms a near monolayer on the surface, as established in [24,45]. This layer conforms to the underlying porosity created by the LBL coating. As such, the porosity of the surface remains intact and near a value of around 50% by volume, as measured by *Phillips (2011)* for surfaces identical to the Smooth Porous Hydrophilic heaters. Likewise, the roughnes is not affected by the conformal hydrophobic coating.

To be certain, surface roughness was also characterized with the surface profilometer and the results are presented in Table 5.19.

Measurement	Contact Angle (Degrees)	Average Contact Angle (Degrees)	Standard Deviation
Static 1	136.4	137.5	1.69%
Static 2	141.9		
Static 3	137.6		
Static 4	136.2		
Static 5	135.3		
Advancing 1	165.9	160.3	3.59%
Advancing 2	149.6		
Advancing 3	161.5		
Advancing 4	160.1		
Advancing 5	164.6		
Receding 1	98.2	97.5	8.31%
Receding 2	87.3		
Receding 3	108.0		
Receding 4	104.5		
Receding 5	89.4		

Table 5.18: Contact angle measurements for Smooth Porous Hydrophobic heater.

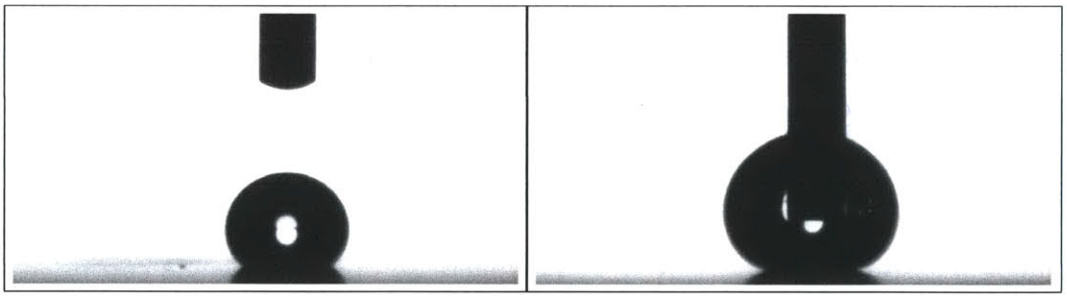

(a) Static Contact Angle

(b) Advancing Contact Angle

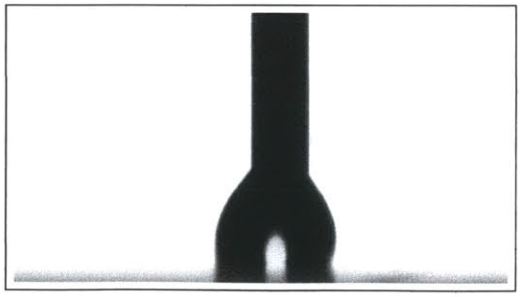

(c) Receding Contact Angle

Figure 5-9: Contact angle measurements for Porous Hydrophobic heater.

Scan	$R_a(\mu m)$	$R_z(\mu m)$
Scan 1	0.119	0.7849
Scan 2	0.11103	0.65729
Scan 3	0.11601	0.64717
Scan 4	0.12214	0.88606
Scan 5	0.11673	0.65548
Average	0.11698	0.72618
St. Dev	3.50%	14.61%

Table 5.19: Roughness measurements for Smooth Porous Hydrophobic heater.

5.5.3 PBF Testing and Discussion

Pattern	CHF ($\frac{kW}{m^2}$)	Burnout($\frac{kW}{m^2}$)	Average CHF ($\frac{kW}{m^2}$)	St. Dev
Smooth Porous Hydrophobic 1	38	38	34	11.8%
Smooth Porous Hydrophobic 2	30	65		
Smooth Porous Hydrophobic 3	35	47		

Table 5.20: CHF and Burnout values for Smooth Porous Hydrophobic heaters.

With the lowest CHF value by an order of magnitude compared to other surfaces, the porous hydrophobic heater surface is interesting because of its *inability* to transfer heat. As the heat flux was increased into these heaters, the traditional nucleate boiling regime was not present. Low heat fluxes below around $5\frac{kW}{m^2}$ resulted in the typical natural convection heat transfer expected. However, at around $15\frac{kW}{m^2}$, two to three large vapor bubbles began for form on the surface. Substantially larger than a typical bubble departing from the surface, these formations were approximately $4mm - 5mm$ in diameter. These large vapor cushions merged and by $30\frac{kW}{m^2}$ a single vapor cushion covered most of the heater surface, which can essentially be considered film boiling. Large vapor bubbles were released from the top of this cushion. Interestingly, the liquid-vapor interface on the heater surface did not move during the ebullition cycle, which results in a lack of time dependent behavior visible in the IR videos of the heater. Because of this unique boiling curve, the degassing procedure for

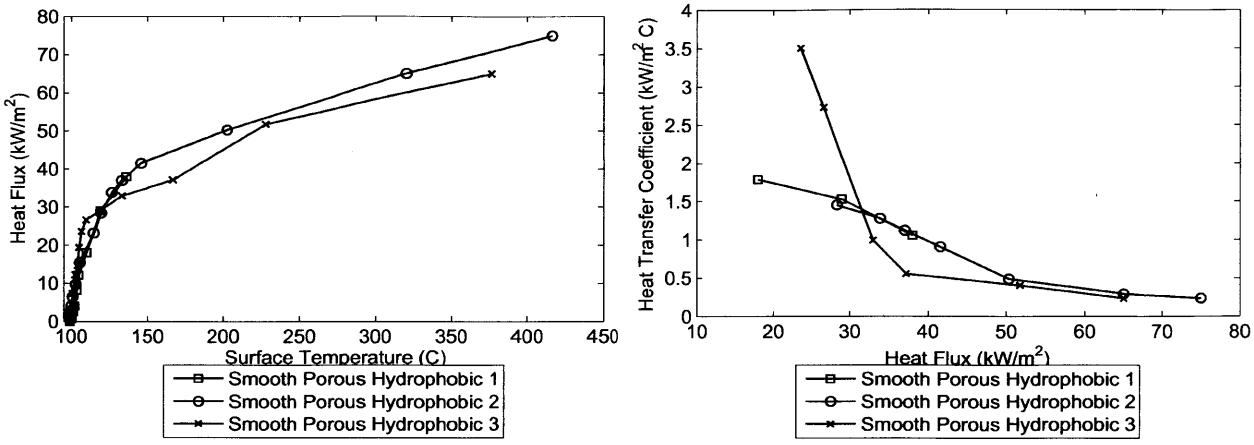

(a) Boiling Curve

(b) Heat Transfer Coefficient

Figure 5-10: Boiling Curve and Heat Transfer Coefficient for Smooth Porous Hydrophobic heaters.

these heaters was amended to heating at $20\frac{kW}{m^2}$ for thirty minutes prior to PBF testing. The progression of the surface temperature profile and the formation of a vapor cushion can be visualized in Figure 5-11. Because of the very limited time dependence in the IR signal, each image is a good representation of the surface temperature profile for the corresponding heat flux.

From the IR signal, it is clear that the boiling surfaces suffer from an inability to rewet, which leads to the growth of the vapor formation on the heater surface. This lends support to the hot spot CHF theory.

Because the transition to film boiling occurred at such a low heat flux, CHF for these heaters did not result in catastrophic heater failure. As such, CHF was considered to be the point at which film boiling dominated the entire heater surface. However, all heaters were able to be driving significantly past CHF offering further insight into the performance of the porous hydrophobic heater surface. In these tests, the surface temperature of the ITO-sapphire increased to quite high levels around $400°C$. In some instances the ITO-sapphire heater eventually cracked, likely because of the thermal stress. While in other tests, the ITO layer of the heater annealed under the high temperature, altering its IR (but not optical) appearance, as can be seen in Figure 5-12. In these cases, the experiment was terminated. *Gerardi (2009)* identified that ITO undergoes a restructuring around $200°C$, which is likely

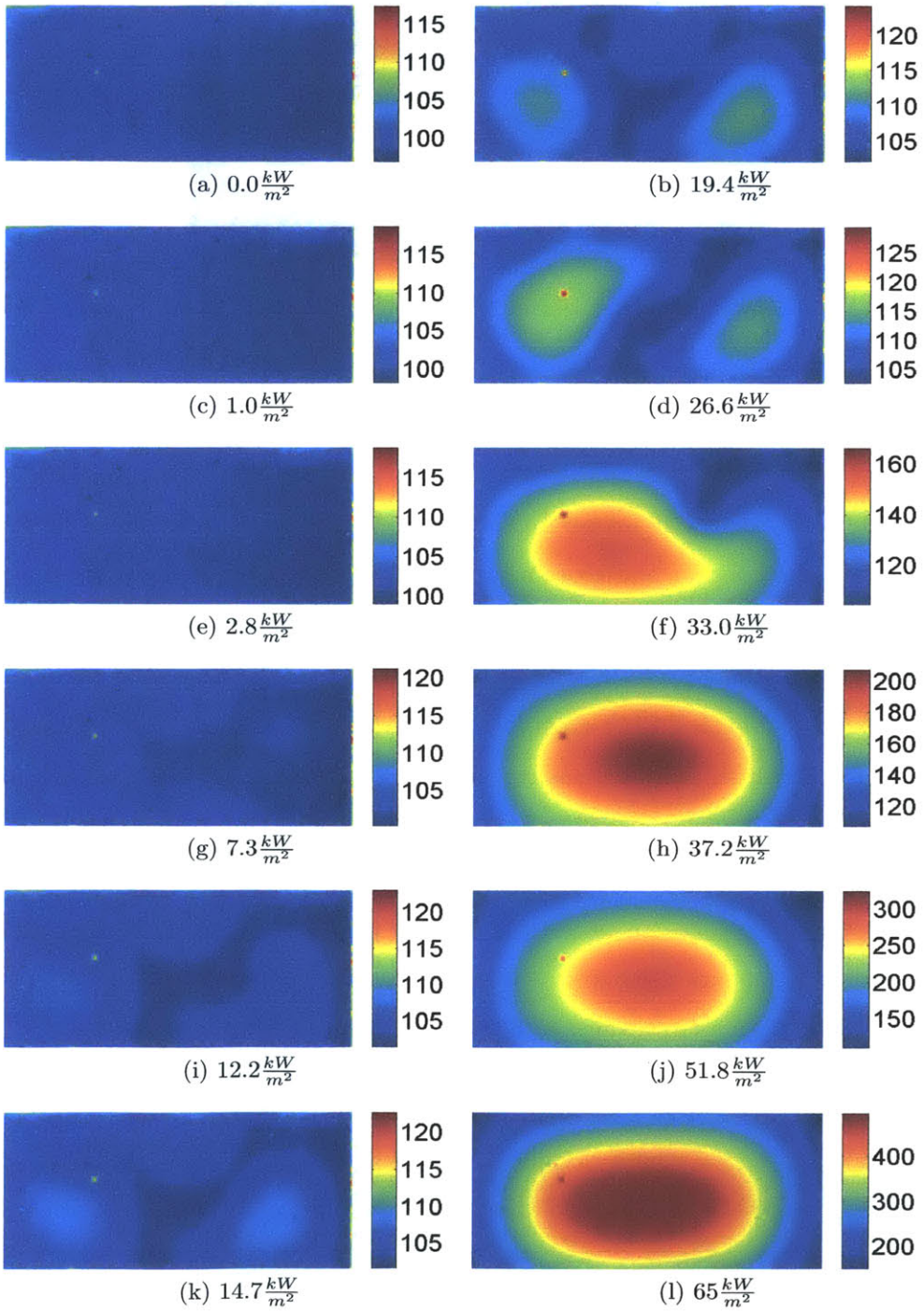

(a) $0.0\frac{kW}{m^2}$ (b) $19.4\frac{kW}{m^2}$

(c) $1.0\frac{kW}{m^2}$ (d) $26.6\frac{kW}{m^2}$

(e) $2.8\frac{kW}{m^2}$ (f) $33.0\frac{kW}{m^2}$

(g) $7.3\frac{kW}{m^2}$ (h) $37.2\frac{kW}{m^2}$

(i) $12.2\frac{kW}{m^2}$ (j) $51.8\frac{kW}{m^2}$

(k) $14.7\frac{kW}{m^2}$ (l) $65\frac{kW}{m^2}$

Figure 5-11: Surface temperature progression of porous hydrophilic heater.

annealing and the result of the IR property change. [58]

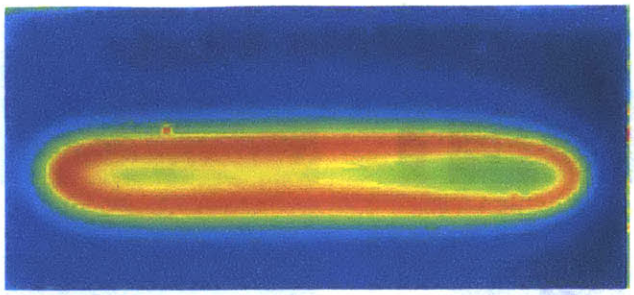

Figure 5-12: Annealed ITO. Note, color difference does not represent temperature profile in this figure, but rather IR opacity. Entire surface is at $99°C$.

Overall, the porous hydrophobic heater presents interesting insight into the separate effects on boiling. While porosity further enhance CHF in the case of hydrophilic heaters, it has the opposite effect for the hydrophobic heaters. As has been established, porosity helps to further increase the contact angle of an already hydrophobic surface. Therefore, there is clearly a large barrier to the rewetting of this heater surface during boiling. As such, there is an extremely early transition to film boiling, with the nucleate boiling regime almost entirely skipped. It is also possible that the porosity of the surface helps to promote and maintain the vapor layer on the heater surface by provide pathways for vapor to move from one location to another. While a surface with these characteristics is not well suited for typical applications requiring high heat transfer and CHF, there may still be uses for a porous hydrophobic coating. Because film boiling can be established with such a low heat flux, such a surface could be used in an application where a vapor layer is desired, perhaps for either insulation or drag reduction purposes. However, the further engineering and deployment of this surface is beyond the scope of this investigation.

5.6 Rough Non-porous Hydrophilic Surface

5.6.1 Surface Fabrication

The first step for the creation of all rough heaters was the fabrication of the post features. Posts with a diameter of $20\mu m$, height of $15\mu m - 20\mu m$ and spaced on a hexagonal pitch of

0.5 mm pitch were created with the photolithography procedure outlined in Section 4.2.5. In order to ensure that all heaters with surface roughness were identical, these heater were batch processed, with all posts created under the same operating conditions. While the photolithography process results in post extrusions from the surface no porosity is induced on the heater surface. Moreover, the regions not covered by the SU-8 posts remains smooth bare sapphire. For the Rough Non-porous Hydrophilic surface, following post fabrication, a $20nm$ thick layer of SiO_2 was deposited on the heater surface via EB-PVD. The SiO_2 vapor uniformly covered the heater surface, conforming to the topography of the posts and transforming the surface to hydrophilic.

In summary, the chronological fabrication steps for the Rough Non-porous Hydrophilic heaters were:

1. Fabricate surface posts via photolithography process.

2. Deposit SiO_2 via EB-PVD.

5.6.2 Surface Analysis

The static contact angle was measured after the standard $0.5s$ to be $< 5°$, as seen in Figure 5-13. The advancing and receding contact angles were not measured, as the surface was extremely well wetting, making such measurements not possible and of little utility. It is important to note that the wettability of this Rough Non-porous Hydrophilic heater is identical to that of the Smooth Non-porous Hydrophilic surface. This indicates that the post structures fabricated on the heater are spaced such that they do not affect the interaction between the water droplet and the heater surface, as expected.

Measurement	Contact Angle (Degrees)
Static 1	$< 5°$
Static 2	$< 5°$
Static 3	$< 5°$
Static 4	$< 5°$
Static 5	$< 5°$

Table 5.21: Contact angle measurements for Rough Non-porous Hydrophilic heater.

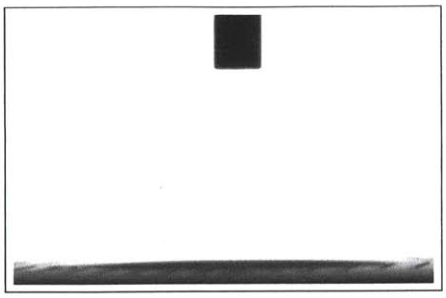

Figure 5-13: Static contact angle measurements for Rough Non-porous Hydrophilic surface.

The surface roughness was characterized with five $2000\mu m$ scans with the stylus profilometer. The tested surface was determined to have an average feature height of $15.53\mu m$, with posts spaced $0.5mm$, apart, as designed. This resulted in average roughness values of $R_a = 2.66\mu m$ and $R_z = 15.27\mu m$. The results of all five scans are presented in Table 5.22.

Scan	$R_a(\mu m)$	$R_z(\mu m)$
Scan 1	2.63251	14.5382
Scan 2	2.78835	14.39037
Scan 3	2.56666	14.29553
Scan 4	2.68372	14.7946
Scan 5	2.66471	16.80592
Average	2.66719	14.96492
St. Dev	3.04%	6.99%

Table 5.22: Roughness measurements for Rough Non-porous Hydrophilic heater.

The profile of the post features can be observed from the profilometer trace presented in Figure 5-14. This trace corresponds to Scan 5 in Table 5.22. Here, the post height and spacing can be readily understood.

SEM images were captured of the surface post features. The non-conductive post features were coated with a thin gold layer to enhance imaging. The SEM was operated at low current and low voltage ($5kV$) settings. Figures 5-15a and 5-15b help to characterize the geometry of the posts. As can be seen from the images, the final diameter of the posts is slightly larger ($25\mu m$) than the target diameter ($20\mu m$). However, the posts are spaced wide enough that the experiment is insensitive to small diametrical fluctuations in the posts. The pitch spacing of the posts was confirmed to be near the target of $0.5mm$.

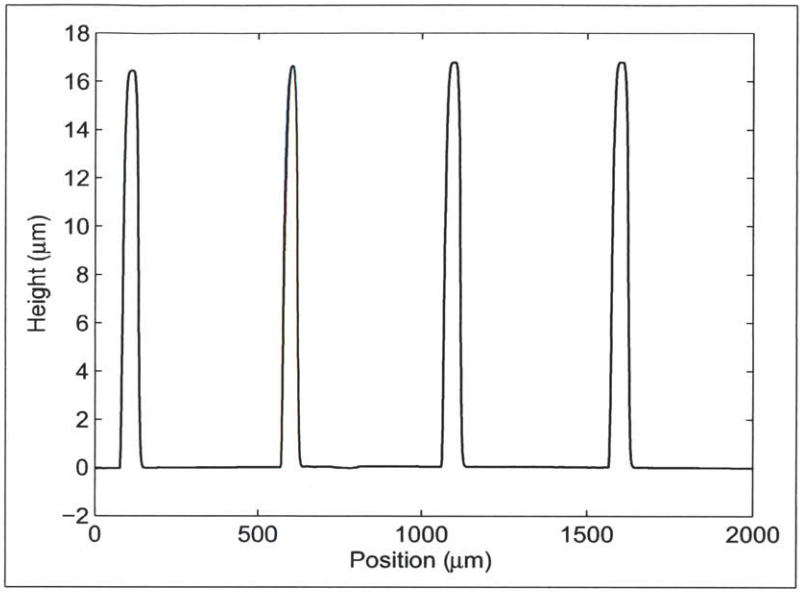

Figure 5-14: Surface profile for Rough Non-porous Hydrophilic heater.

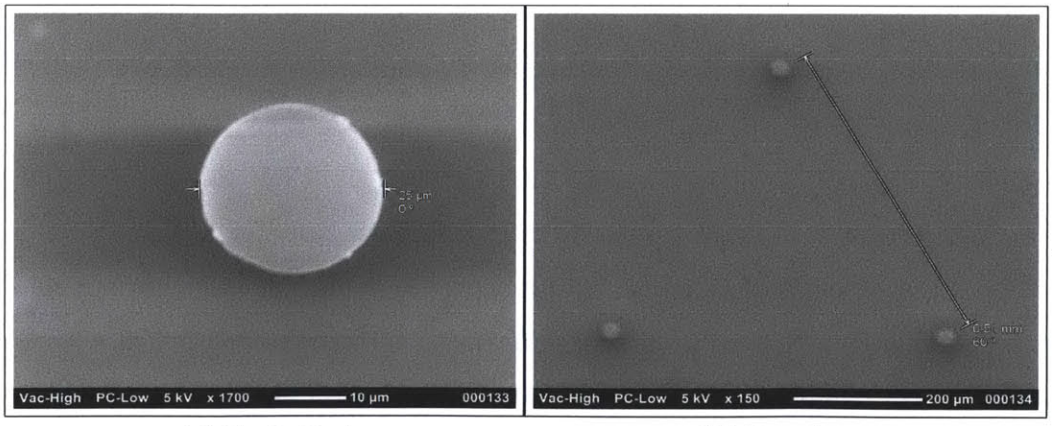

(a) Single Post (b) Post Array

Figure 5-15: SEM images of post features.

5.6.3 PBF Testing and Discussion

Pattern	CHF ($\frac{kW}{m^2}$)	Average CHF ($\frac{kW}{m^2}$)	St. Dev
Rough Non-porous Hydrophilic 1	1007	1063	5.5%
Rough Non-porous Hydrophilic 2	1123		
Rough Non-porous Hydrophilic 3	1059		

Table 5.23: CHF values for Rough Non-porous Hydrophilic heaters.

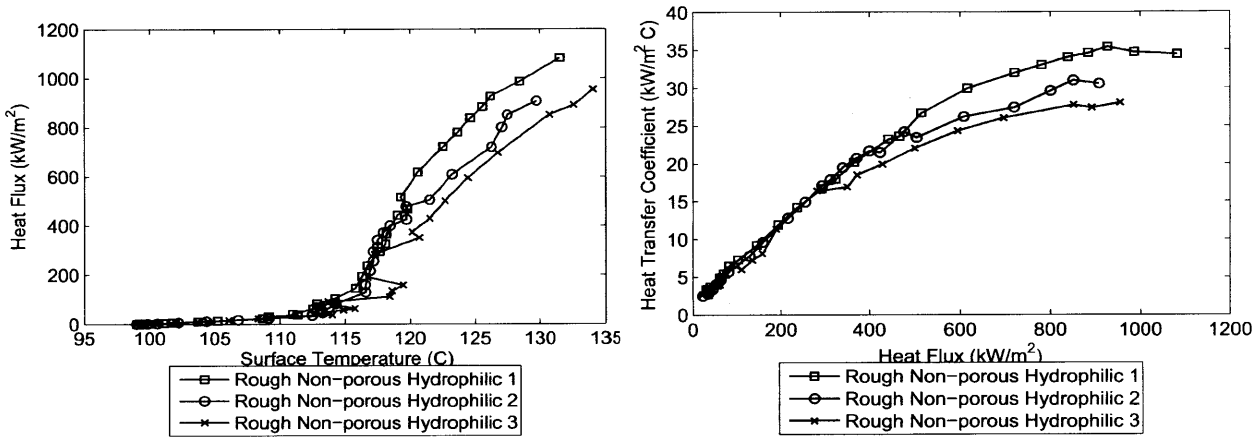

(a) Boiling Curve

(b) Heat Transfer Coefficient

Figure 5-16: Boiling Curve and Heat Transfer Coefficient for Rough Non-porous Hydrophilic heaters

The Rough Non-Porous Hydrophilic heaters had an average CHF of $1063\frac{kW}{m^2}$ with a standard deviation of 5.5%. The roughness induced by the post features did not have a significant effect on CHF, as attested to by the fact that the CHF value for this heater was nearly identical to that of its smooth counterpart (Smooth Non-Porous Hydrophilic heater, average CHF = $1009\frac{kW}{m^2}$). Additionally, the superposition of roughness and hydrophilicty did not combine to create a significantly better performing surface (as was the case with porosity and hydrophilicty). The boiling curves and CHF values for the heaters tested in this surface series were tightly grouped, showing repeatability. These results shed interesting light on the common perception of the importance of surface roughness on boiling performance. As is clearly evident from these results, roughness had no appreciable affect on a non-porous hydrophilic surface. More explicity comparisons of this heater surface's performance with

others is made in Section 5.11.

5.7 Modified Rough Non-porous Hydrophilic Surface

5.7.1 Surface Fabrication

Posts with a diameter of $20\mu m$, height of $15\mu m - 20\mu m$ and spaced on a hexagonal pitch of 1.98 mm pitch were created with the photolithography procedure outlined in Section 4.2.5. Following post fabrication, a $20nm$ thick layer of SiO_2 was deposited on the heater surface via EB-PVD. The SiO_2 vapor uniformly covered the heater surface, conforming to the topography of the posts and transforming the surface to hydrophilic.

In summary, the chronological fabrication steps for the Rough Non-porous Hydrophilic heaters were:

1. Fabricate surface posts via photolithography process.

2. Deposit SiO_2 via EB-PVD.

5.7.2 PBF Testing and Discussion

Pattern	CHF ($\frac{kW}{m^2}$)	Average CHF ($\frac{kW}{m^2}$)	St. Dev
Rough Non-porous Hydrophilic (1.98mm post pitch) 1	1049	1022	3.6%
Rough Non-porous Hydrophilic (1.98mm post pitch) 2	996		

Table 5.24: CHF values for Modified Rough Non-porous Hydrophilic heaters.

The Modified Rough Non-porous Hydrophilic heaters had an average CHF of $1022\frac{kW}{m^2}$ with a standard deviation of 3.6%. The more widely spaced posts did not significantly change the CHF values of the heaters. The results of these test were very similar to the standard Rough Non-porous hydrophilic heaters, as was expected. These findings imply that the roughness imparted in this experiment would similarly effect CHF at elevated presures ($5bar$, as tested here).

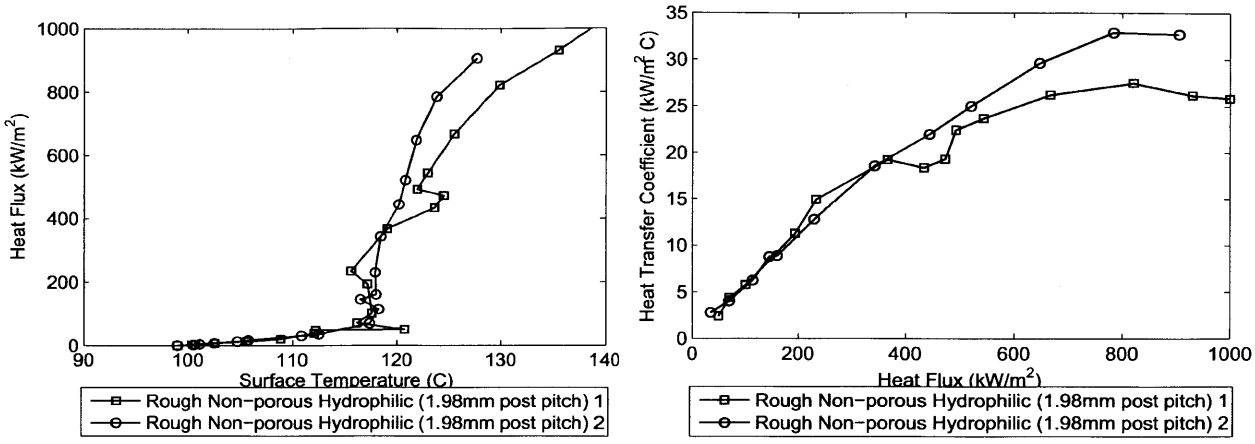

(a) Boiling Curve

(b) Heat Transfer Coefficient

Figure 5-17: Boiling Curve and Heat Transfer Coefficient for Modified Rough Non-porous Hydrophilic heaters (1.98mm post pitch).

5.8 Rough Non-porous Hydrophobic Surface

5.8.1 Surface Fabrication

The fabrication of the Rough Non-porous Hydrophobic surface was identical to the Rough Non-porous Hydrophilic surface, with the inclusion of a hydrophobizing fluorosilane CVD at the end of the process. First, posts with a diameter of $20\mu m$, height of $15\mu m - 20\mu m$ and spaced on a hexagonal pitch of 0.5 mm pitch were fabricated. Next, a $20nm$ layer of SiO_2 was deposited. In this instance, this layer is not used for its hydrophilicity, but rather for its OH- groups, which provide binding sites for hydrophobic fluorosilane. Finally, the heater was exposed to fluorosilane for eight hours, allowing the surface to be coated and transformed to hydrophobic. As with the Smooth Non-porous Hydrophobic surface, the longer fluorosilane exposure was utilized to create a uniform coating in the lack of porosity. The fluorosilane exposure temperature of $140°C$ is below the melting point of SU-8, allowing the post features to remain intact.

In summary, the chronological fabrication steps for the Rough Non-porous Hydrophobic heaters were:

1. Fabricate surface posts via photolithography process.

2. Deposit SiO_2 via EB-PVD.

3. Deposit fluorosilane via CVD using long, eight hour exposure.

5.8.2 Surface Analysis

The average static, advancing and receding contact angles of the Rough Non-porous Hydrophobic heater were measured to be 112.6°, 132.3°, and 85.7°, respectively. The complete set of contact angle measurements made on this heater surface is presented in Table 5.25.

Measurement	Contact Angle (Degrees)	Average Contact Angle (Degrees)	Standard Deviation
Static 1	112.7	112.6	1.50%
Static 2	113.0		
Static 3	115.3		
Static 4	111.9		
Static 5	110.1		
Advancing 1	135.0	132.3	2.39%
Advancing 2	135.1		
Advancing 3	130.9		
Advancing 4	131.6		
Advancing 5	129.0		
Receding 1	84.9	85.8	3.82%
Receding 2	92.0		
Receding 3	82.6		
Receding 4	83.4		
Receding 5	85.7		

Table 5.25: Contact angle measurements for Rough Non-porous Hydrophobic heater.

After fluorosilane deposition, the surfaces were examined under an optical microscope to confirm the integrity of the post features. These images are presented in Figures 5-19a and 5-19b. The orange tint is a result of the fluorosilane coating. Additionally, multiple contaminants on the surface can be seen in Figure 5-19b; these were deposited during the CVD fluorosilane process. While steps are taken to clean all equipment used, a degree of surface contamination is inevitable (the laboratory where CVD is carried out is not a "clean room"). Surface contamination can be a leading inhibitor of achieving high contact angle for hydrophobic surfaces.

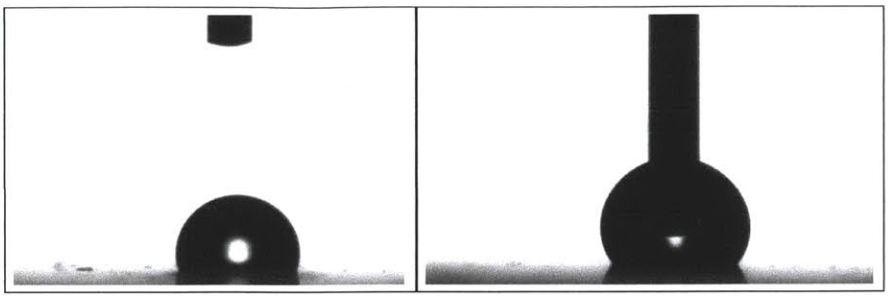

(a) Static Contact Angle (b) Advancing Contact Angle

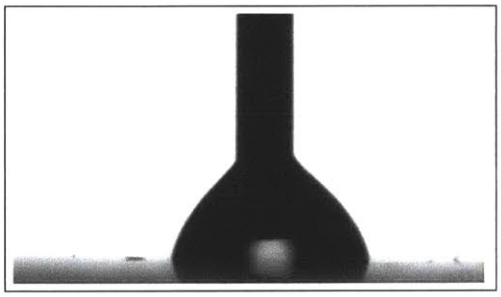

(c) Receding Contact Angle

Figure 5-18: Contact angle measurements for Rough Non-porous Hydrophobic surface.

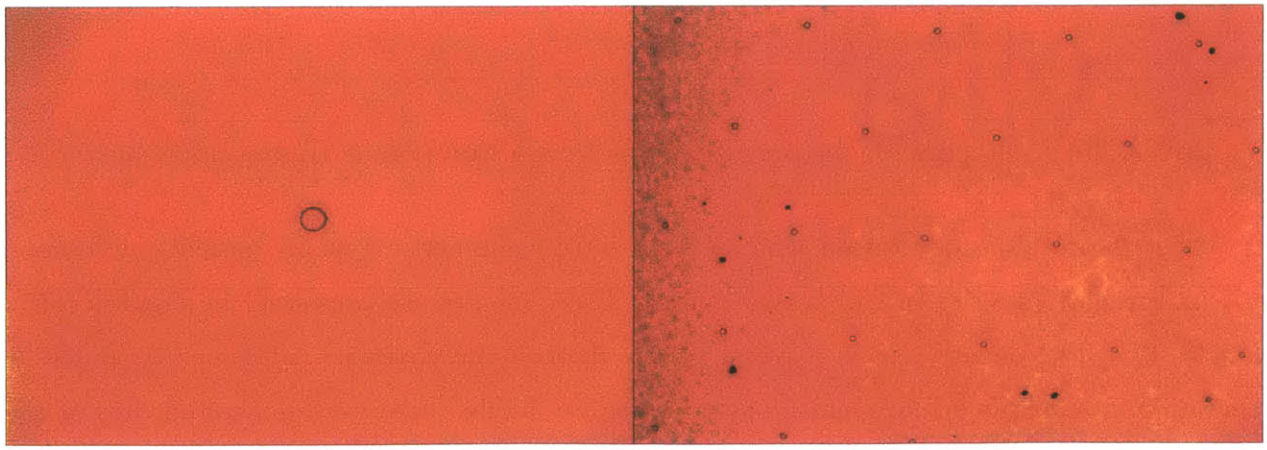

(a) Single Post (b) Array of Posts

Figure 5-19: Optical microscope images of posts on Rough Non-porous Hydrophobic heater after CVD fluorosilane process.

The average surface roughness values were measured to be $R_a = 2.59\mu m$ and $R_z = 15.22\mu m$. The complete list of surface roughness measurements made with the surface profiler is presented in Table 5.26.

Scan	$R_a(\mu m)$	$R_z(\mu m)$
Scan	Ra (um)	Rz (um)
Scan 1	2.67481	16.82892
Scan 2	2.26723	13.31616
Scan 3	2.70959	15.37344
Scan 4	2.68637	16.56404
Scan 5	2.63484	14.05912
Average	2.59457	15.22834
St. Dev	7.13%	10.06%

Table 5.26: Roughness measurements of Rough Non-porous Hydrophobic surface.

5.8.3 PBF Testing and Discussion

Pattern	CHF ($\frac{kW}{m^2}$)	Average CHF ($\frac{kW}{m^2}$)	St. Dev
Rough Non-porous Hydrophobic 1	1172	1067	15.29%
Rough Non-porous Hydrophobic 2	1150		
Rough Non-porous Hydrophobic 3	879		

Table 5.27: CHF values for Rough Non-porous Hydrophobic heaters.

The Rough Non-porous Hydrophobic surfaces had an average CHF of $1067\frac{kW}{m^2}$, with a standard deviation of 15.29%. The boiling curves were not as tightly grouped as other heaters tested; however a wider spread was more commonly observed wtih hydrophobic surfaces. This may be an affect of non-uniformities in the hydrophobic coating on a non-porous surface. It may also be a natural variance resulting from tendancy of the surface to repel water during boiling. Interestingly, however, this surface performed very similarly to the Smooth Non-Porous Hydrophobic surface, further implying that the post features have no effect on boiling. Likewise, the combination of roughness and hydrophobicity did not combine to have a significant effect on the boiling performance. This is again in contrast

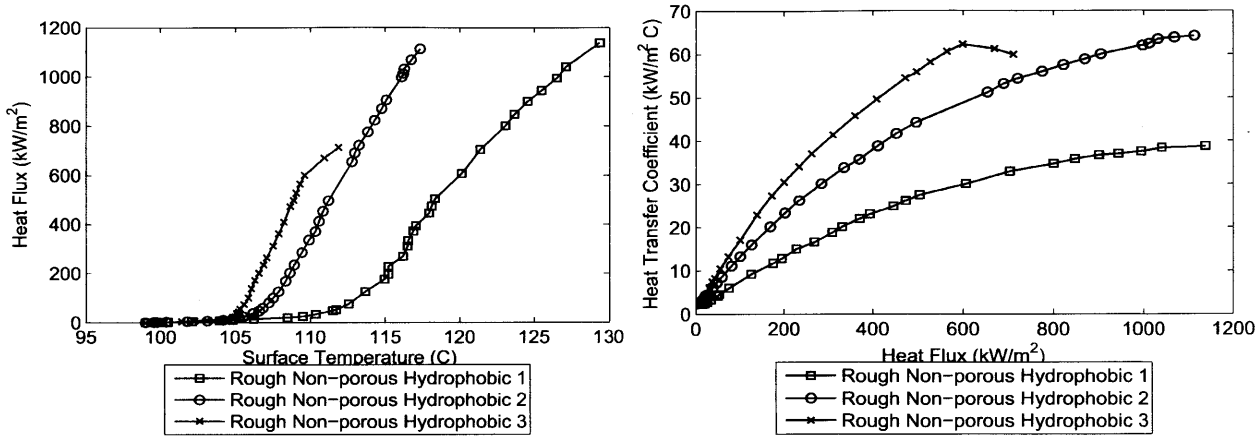

(a) Boiling Curve

(b) Heat Transfer Coefficient

Figure 5-20: Boiling Curve and Heat Transfer Coefficient for Rough Non-porous Hydrophobic heaters.

to the effect of combining porosity and hydrophobicity, which had markedly detrimental consequences.

5.9 Rough Porous Hydrophilic Surface

5.9.1 Surface Fabrication

First, posts with a diameter of $20\mu m$, height of $15\mu m - 20\mu m$ and spaced on a hexagonal pitch of 0.5 mm pitch were fabricated under the same conditions as in Section 5.7.1. Next, the heaters were coated with fifty layers of $50nm$ SiO_2 particles using the LBL procedure. Because the posts are significantly larger than the SiO_2 particles and spaced on a large pitch, the LBL layers were able to conform to the surface topology. As in previous test cases, the SiO_2 nanoparticles induced both porosity and hydrophilicity in the heater surface.

1. Fabricate surface posts via photolithography process.
2. LBL deposition with $50nm$ SiO_2 particles for fifty layers.

5.9.2 Surface Analysis

Immediately prior to PBF testing, the average static contact angle of the Rough Porous Hydrophilic heater was measured to be about 5°. This is similar to the wettability of the Smooth Porous Hydrophilic heater, implying that the post features do not affect the wettability of the surface.

Measurement	Contact Angle (Degrees)
Static 1	$\approx 5°$
Static 2	$\approx 5°$
Static 3	$\approx 5°$
Static 4	$\approx 5°$
Static 5	$\approx 5°$

Table 5.28: Contact angle measurements for Rough Porous Hydrophilic heater.

The surface roughness of the heater was characterized with the surface profilometer. On average, for the Rough Porous Hydrophobic heater, $R_a = 2.23\mu m$ and $R_z = 14.09\mu m$. The complete set of scans is presented in Table 5.29.

Additionally, SEM images of SiO_2 multilayers deposited on top of similar posts were acquired by *Truong (2011)*. Presented in Figure 5-22, this image demonstrates how the LBL

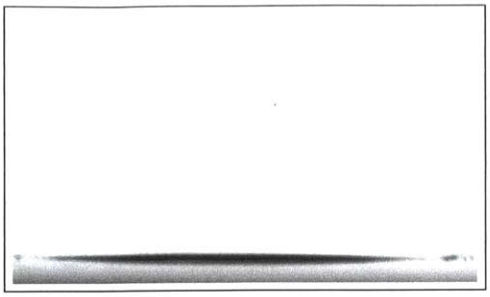

Figure 5-21: Contact angle measurements for Rough Porous Hydrophilic surface.

Scan	$R_a(\mu m)$	$R_z(\mu m)$
Scan 1	2.05625	13.65465
Scan 2	2.42532	14.79211
Scan 3	2.0321	15.09634
Scan 4	2.37961	13.30169
Scan 5	2.26319	13.59711
Average	2.23129	14.08838
St. Dev	8.11%	5.68%

Table 5.29: Roughness measurements for Rough Porous Hydrophilic heater.

coating conforms to the post extrusion.

5.9.3 PBF Testing and Discussion

Pattern	CHF ($\frac{kW}{m^2}$)	Average CHF ($\frac{kW}{m^2}$)	St. Dev
Rough Porous Hydrophilic 1	1594	1590	7.0%
Rough Porous Hydrophilic 2	1700		
Rough Porous Hydrophilic 3	1478		

Table 5.30: CHF values for Rough Porous Hydrophilic surface heaters.

The Rough Porous Hydrophilic heater was very well performing, with an average CHF of $1590\frac{kW}{m^2}$ and a standard deviation of 7.0%. This heater performed very similarly to the Smooth Porous Hydrophilic heater, thereby again implying that the post features had little effect on the boiling performance. In all likelyhood, the fact that the posts existed on the surface was moot and the heater's performance was simply driven by the porosity and hydrophilicty. These results continue to support the trend of roughness having little to

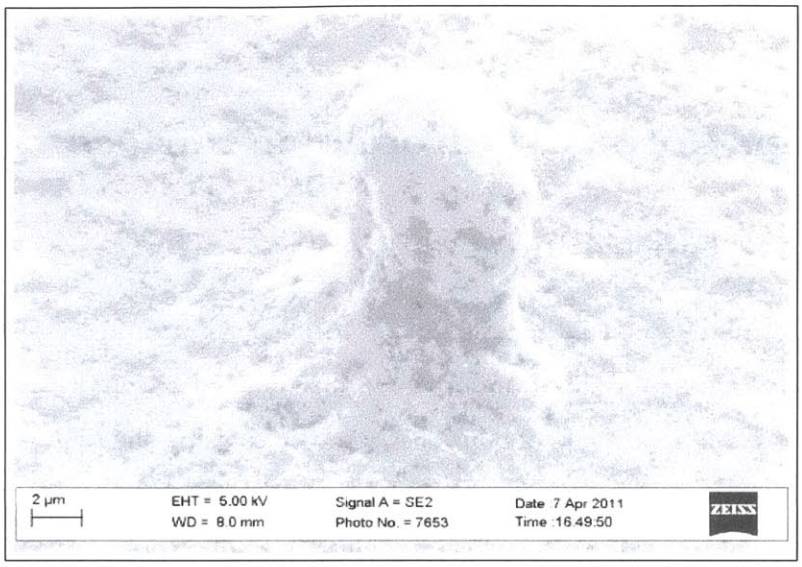

Figure 5-22: SEM image of SiO_2 multilayers conforming to post feature on surface (Acquired by *Troung (2011)*). [26]

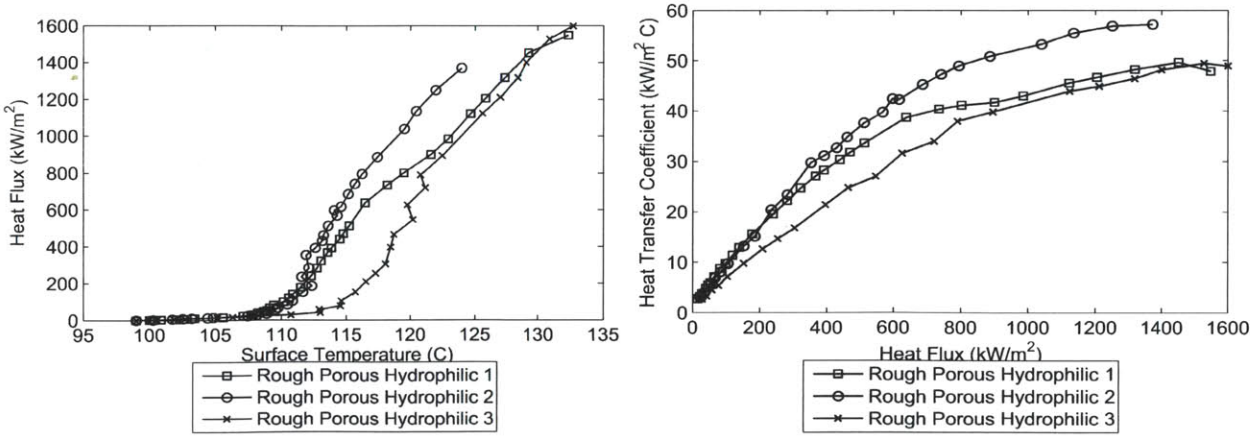

(a) Boiling Curve

(b) Heat Transfer Coefficient

Figure 5-23: Boiling Curve and Heat Transfer Coefficient for Rough Porous Hydrophilic heaters.

no effect on boiling performance, while the combination of porosity and hydrophilicity is particularly enhancing.

5.10 Rough Porous Hydrophobic Surface

5.10.1 Surface Fabrication

First, posts with a diameter of $20\mu m$, height of $15\mu m - 20\mu m$ and spaced on a hexagonal pitch of 0.5 mm pitch were fabricated under the same conditions as in Section 5.7.1. Next, the heaters were coated with fifty layers of $50nm$ SiO_2 particles using the LBL procedure. As with the Rough Porous Hydrophilic surfaces, the LBL layers were able to conform to the surface topology. Finally, the overall surface was converted to hydrophobic via the fluorosilane deposition process. Here, the shorter fluorosilane CVD exposure of thirty minutes was adequate for uniform coating.

1. Fabricate surface posts via photolithography process.

2. LBL deposition with $50nm$ SiO_2 particles for fifty layers.

3. Fluorosilane CVD with an exposure time of thirty minutes.

5.10.2 Surface Analysis

Contact Angle Measurement

The average static, advancing and receding contact angles were measured to be 139.8°, 149.4° and 103.6°. These values are consistent the with contact angle measurements of the Smooth Porous Hydrophobic heater. This confirms that the posts were spaced appropriately so as not induce any capillary action.

The surface roughness was characterized to be on average, $R_a = 1.96\mu m$ and $R_z = 13.25\mu m$.

Measurement	Contact Angle (Degrees)	Average Contact Angle (Degrees)	Standard Deviation
Static 1	139.1	139.8	1.79%
Static 2	142.6		
Static 3	135.6		
Static 4	143.1		
Static 5	139.9		
Advancing 1	156.7	149.4	3.02%
Advancing 2	163.9		
Advancing 3	163.7		
Advancing 4	171.8		
Advancing 5	167.4		
Receding 1	97.65	103.6	4.56%
Receding 2	98.2		
Receding 3	107.7		
Receding 4	106.8		
Receding 5	107.9		

Table 5.31: Contact angle measurements for Porous Rough Hydrophobic heater.

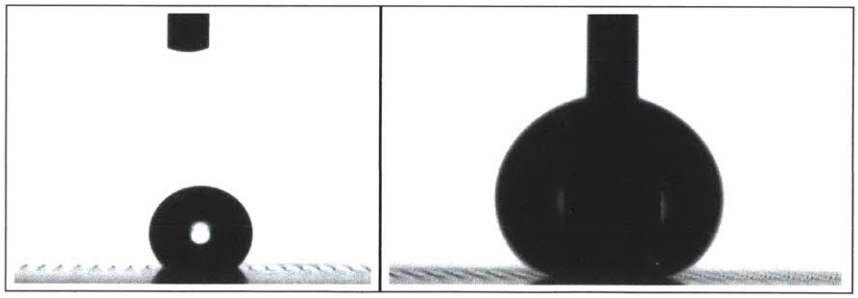

(a) Static Contact Angle (b) Advancing Contact Angle

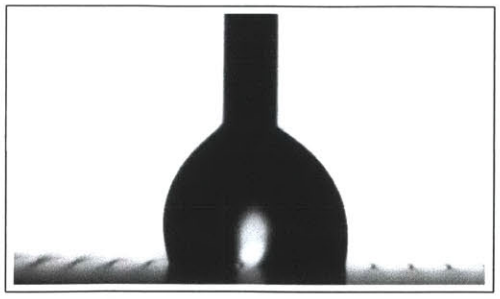

(c) Receding Contact Angle

Figure 5-24: Contact angle measurements for Rough Porous Hydrophobic surface.

Scan	$R_a(\mu m)$	$R_z(\mu m)$
Scan 1	1.95594	12.30319
Scan 2	1.82255	14.69225
Scan 3	1.8312	12.32826
Scan 4	1.96296	12.6162
Scan 5	2.2625	14.31527
Average	1.96703	13.25103
St. Dev	9.05%	8.74%

Table 5.32: Roughness measurements for Rough Porous Hydrophobic heater.

Pattern	CHF $(\frac{kW}{m^2})$	Burnout $(\frac{kW}{m^2})$	Avg. CHF $(\frac{kW}{m^2})$	St. Dev
Rough Porous Hydrophobic 1	20-40	815	-	-
Rough Porous Hydrophobic 2	40-60	700		
Rough Porous Hydrophobic 3	20-40	359		

Table 5.33: CHF and heater burnout values for Rough Porous Hydrophobic heaters.

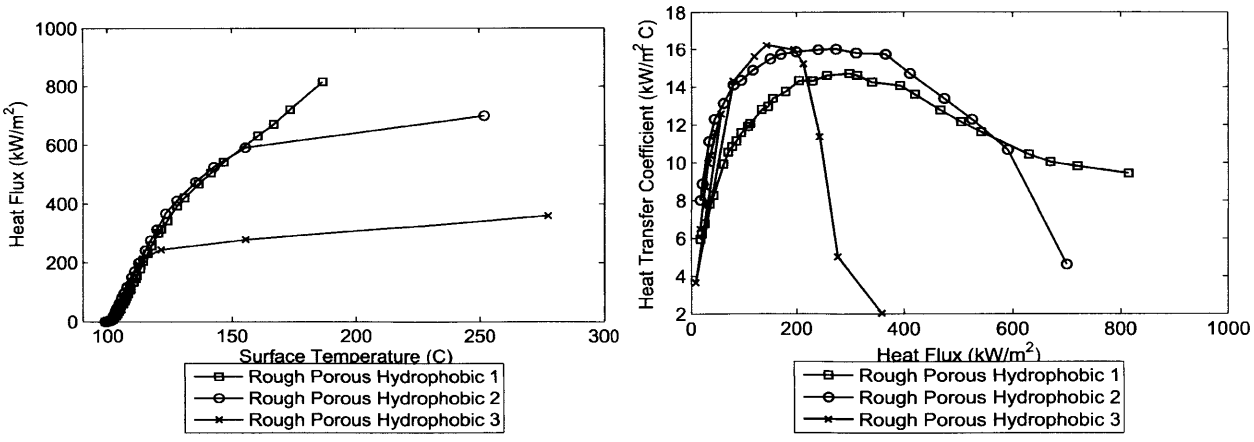

(a) Boiling Curve

(b) Heat Transfer Coefficient

Figure 5-25: Boiling Curve and Heat Transfer Coefficient for Rough Porous Hydrophobic Heaters

5.10.3 PBF Testing and Discussion

Overall, the Rough Porous Hydrophobic heaters were a poor surface for transferring heat, as exemplified in Figure 5-25. However, these heaters provide an interesting contrast in performance to the Smooth Porous Hydrophobic heaters. As seen in Section 5.5, the Smooth Porous Hydrophobic heaters have a markedly low CHF value, with an almost instant transition from natural convection to film boiling. As CHF occurred without heater burnout, CHF was called when the pixels on the IR signal saturated, indicating a region significantly hotter than the surrounding area. Two to three large vapor formations were typically witnessed at heat fluxes as low as $20\frac{kW}{m^2}$. Shortly thereafter, these separate vapor cushions coalesced create a single large vapor layer, which covered most of the heater surface.

Distinct regions of the Rough Porous Hydrophobic heaters achieved CHF at similarly low heat fluxes. However, unlike the Smooth Porous Hydrophobic heaters, these separate vapor cushions did not rapidly coalesce. As such, the distinction between CHF and burnout must be explicitly recognized. In most other tests, CHF and burnout - or heater destruction - occurred simultaneously. Here, CHF was achieved at a similar heat flux as Smooth Porous Hydrophobic heater. However, burnout typically occurred at a much higher heat flux. In many instances, the individual vapor formations maintained their integrity up to relatively moderate heat fluxes of between $400\frac{kW}{m^2}$ and $700\frac{kW}{m^2}$. During this time, surface temperatures in film boiling regions reached extremely high values, while the surface temperature in regions that appeared to be in the nucleate boiling regime were more moderate. This behavior leads one to believe that the roughness, induced by the surface posts, hindered lateral movement of the vapor cushions on the surface. By essentially corralling these vapor regions and preventing coalescence, the posts seem to have allowed the heater to be pushed to higher heat fluxes than were achievable with the Smooth Porous Hydrophobic heater.

For example in Figure 5-26, six distinct vapor regions, identified by their significantly higher temperatures, were present through the entire test. The upper two regions hit CHF around $50\frac{kW}{m^2}$, which is approximately consistent with CHF for the Smooth Porous Hydrophobic heaters. However, as the heat flux was continually increased, the vapor regions did not spread on the heater surface. Furthermore, the size of each vapor cushion did not

vary significantly, with little transient movement of the vapor boundary visible on the IR signal. It was not until around $815\frac{kW}{m^2}$ that the upper left vapor formation slide downward, coalesced with its neighbor and induced heater burnout shortly thereafter.

A similar behavior was witnessed in the second Rough Porous Hydrophobic heater. Here, two distinct regions of film boiling were created and sustained until heater burn out at approximately $700\frac{kW}{m^2}$. Again, however, it appears that CHF was achieved locally at some point between $44\frac{kW}{m^2}$ and $61\frac{kW}{m^2}$. The behavior of the vapor cushions can be observed in Figure 5-27. Again, it is remarkable how the post structures were able to contain the spreading of the film boiling region, even at relatively high heat fluxes. The size of the vapor cushion did not grow substantially until $700\frac{kW}{m^2}$.

The growth of the center vapor cushion at the point of heater burnout was captured on the IR signal. As can be seen in Figure 5-28, the larger center vapor formation expands and coalesces with the smaller vapor region. Following this merger, the vapor cushion engulfed the entire active heater area, leading to heater destruction.

Similar containment of localized film boiling was also observed in the third Rough Porous Hydrophobic heater. Here, two distinct vapor bubbles formed at opposite corners of the active heater. They maintained their isolation until a flux of around $350\frac{kW}{m^2}$, at which point the lower formation expanded to coalesce with the other region. While heater burnout occurred at a lower heat flux in this test case than with the previous two Rough Porous Hydrophobic heaters, the isolated behavior of the vapor formations was consistent. Additionally, local CHF seems to be achieved at a similarly low heat flux value as in previous tests.

The consistent localized film boiling on the three Rough Porous Hydrophobic heaters was relatively unstable. With a slight disturbance, one film cushion could overcome the pinning effect of the surface posts and move towards and adjacent film formation. This migration and subsequent coalescence almost always initiated a cascade effect on the heater surface. The rapidly growing film cushion would engulf the majority of the heater surface and burnout would occur shortly thereafter. That this surface is so unstable accounts for the larger variability in burnout heat flux values. However, in all instances, the achievement of CHF was around $40\frac{kW}{m^2}$ to $70\frac{kW}{m^2}$. The high level of hydrophobicity induced by both the surface chemistry and porosity serve inhibit surface rewetting, which is consistent with the

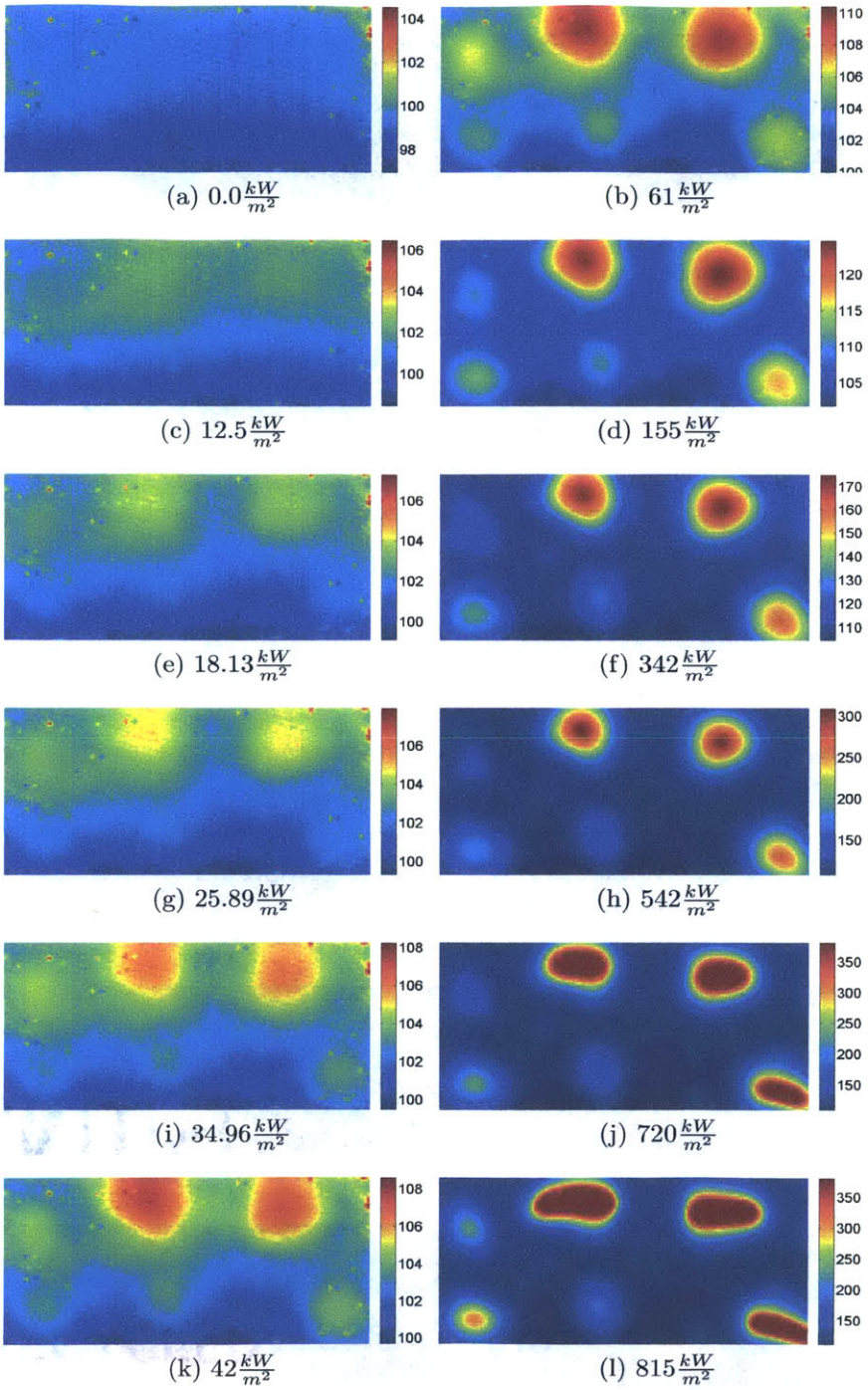

(a) $0.0\frac{kW}{m^2}$ (b) $61\frac{kW}{m^2}$

(c) $12.5\frac{kW}{m^2}$ (d) $155\frac{kW}{m^2}$

(e) $18.13\frac{kW}{m^2}$ (f) $342\frac{kW}{m^2}$

(g) $25.89\frac{kW}{m^2}$ (h) $542\frac{kW}{m^2}$

(i) $34.96\frac{kW}{m^2}$ (j) $720\frac{kW}{m^2}$

(k) $42\frac{kW}{m^2}$ (l) $815\frac{kW}{m^2}$

Figure 5-26: Surface temperature progression of Rough Porous Hydrophobic 1 heater. Note, how the local regions of film boiling maintain their position through the full range of heat flux levels.

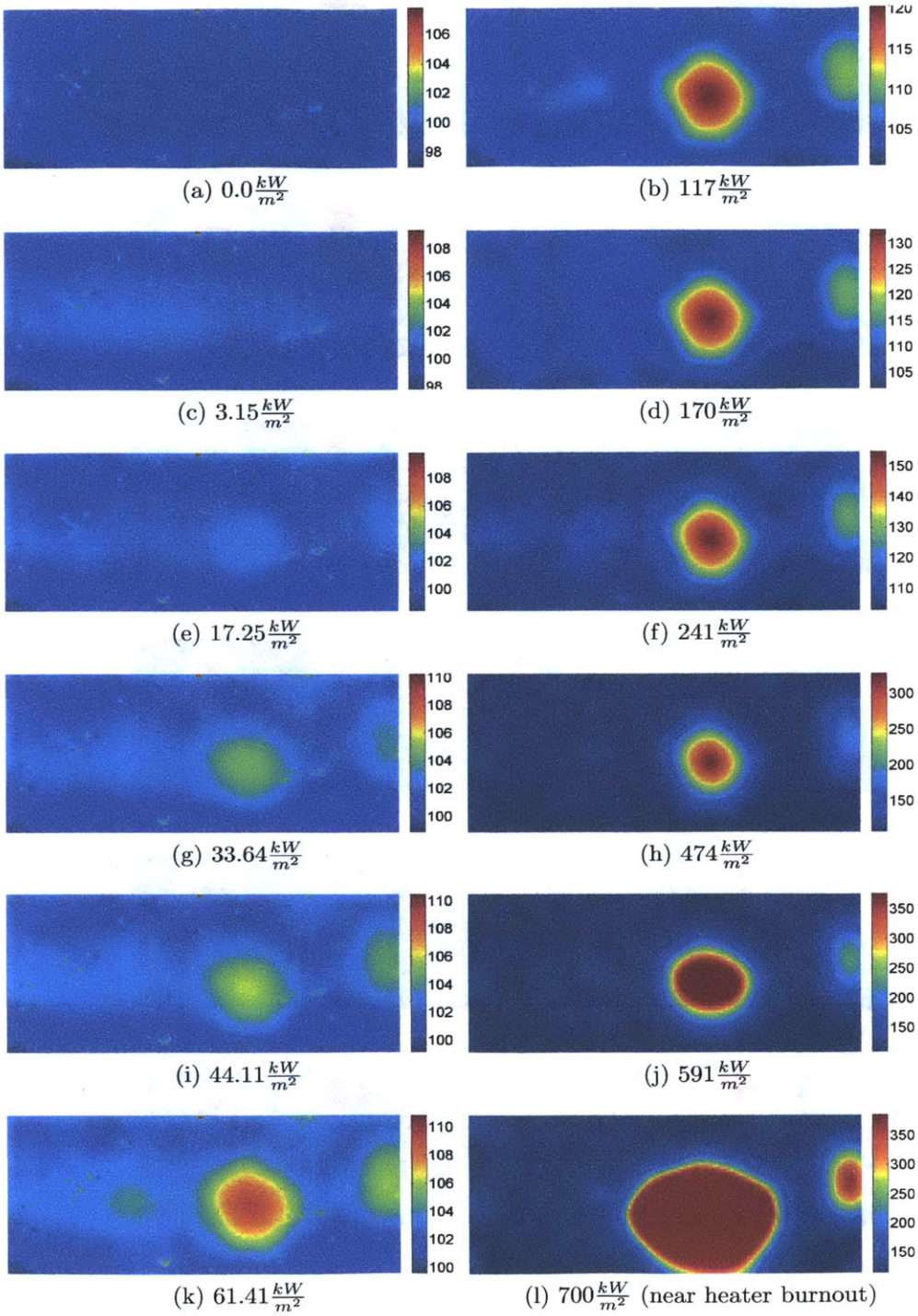

Figure 5-27: Surface temperature progression of Rough Porous Hydrophobic 2 heater.

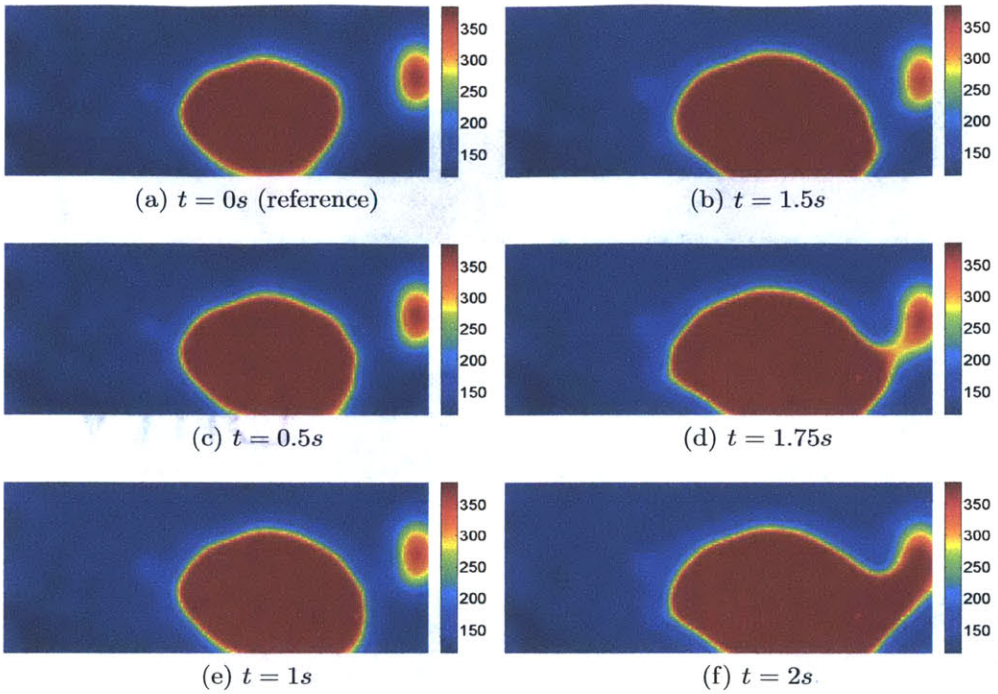

(a) $t = 0s$ (reference) (b) $t = 1.5s$

(c) $t = 0.5s$ (d) $t = 1.75s$

(e) $t = 1s$ (f) $t = 2s$

Figure 5-28: Vapor cushion growth on Rough Porous Hydrophobic 2 heater at $700\frac{kW}{m^2}$

Smooth Porous Hydrophobic surface.

The ability of the posts to contain CHF locally on the heater surface is inspiring. From these tests, it is evident that within a small heater surface (just $2cm^2$), drastically different boiling regimes can co-exist simultaneously. Potentially, this phenomena could be exploited, to create a heater surface which is actually divided up into multiple and independent cells. If these sub-surfaces can be created such that adjacent bodies are insulated from each other (perhaps through post like features), then local CHF may be tolerated briefly without global burnout. This could provide a defense in depth type margin of safety for boiling systems.

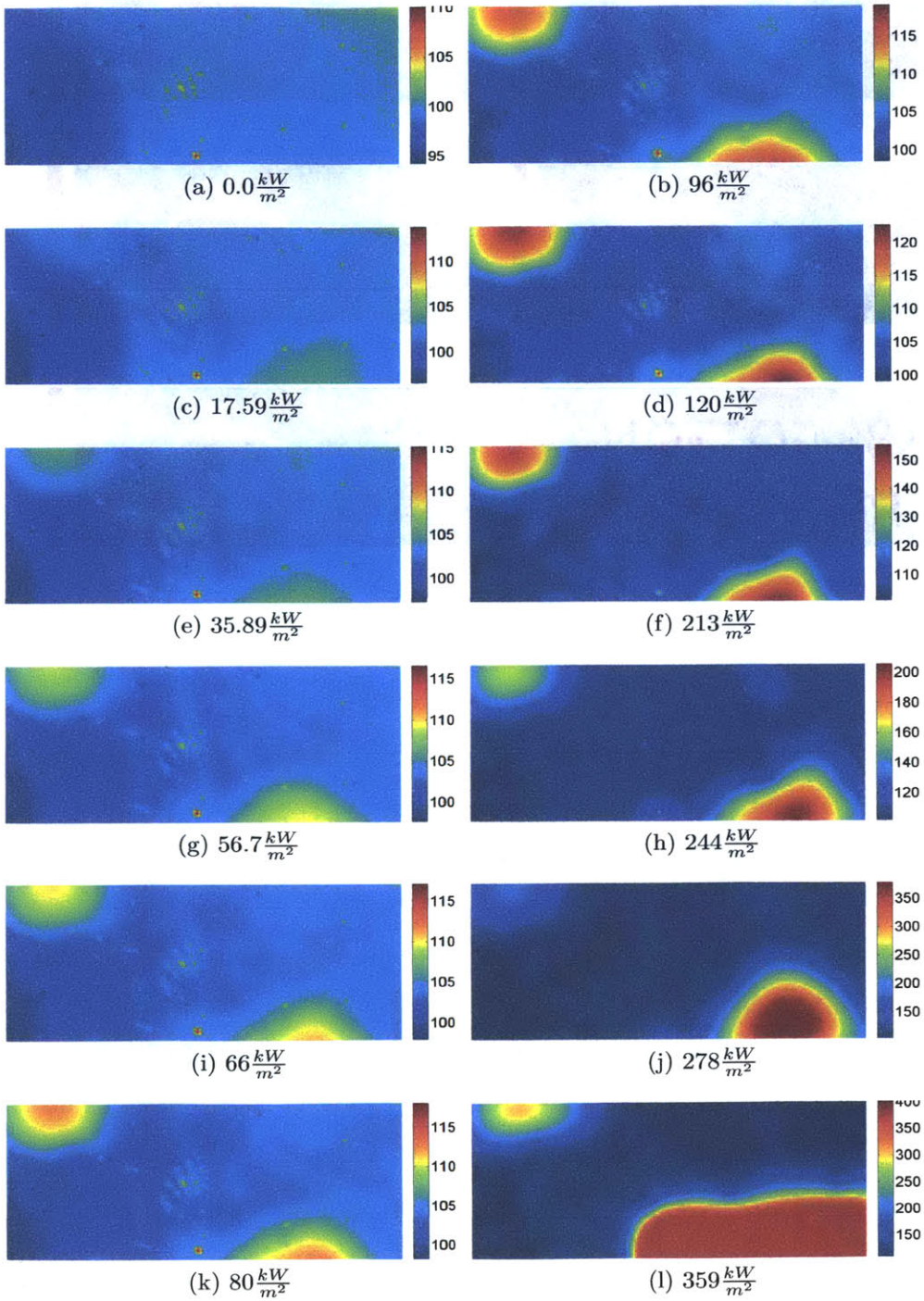

Figure 5-29: Surface temperature progression of Rough Porous Hydrophobic 3 heater.

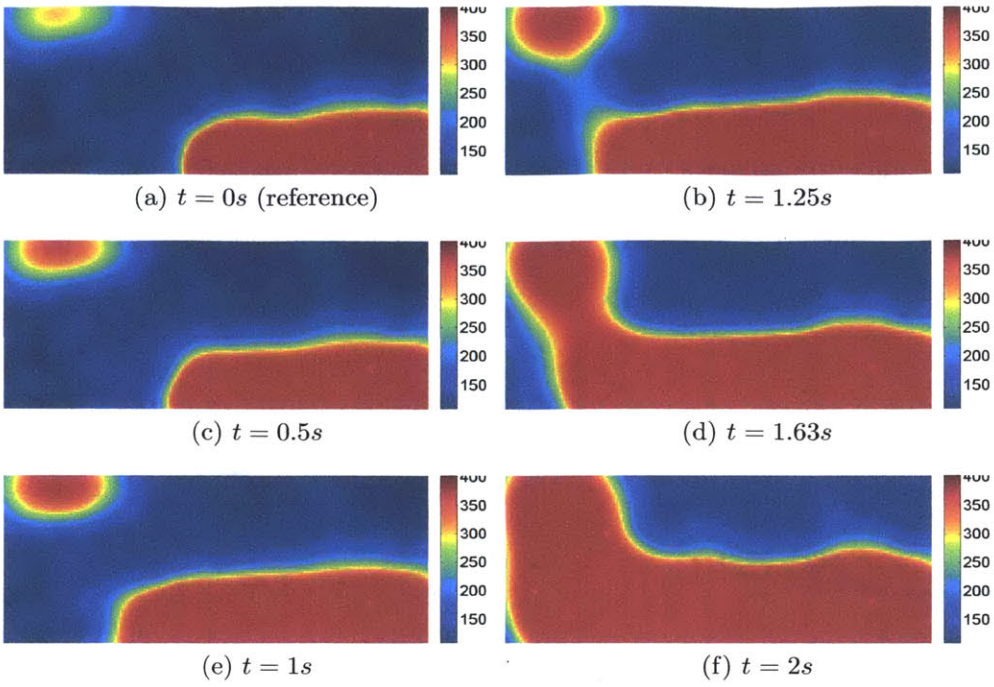

(a) $t = 0s$ (reference) (b) $t = 1.25s$

(c) $t = 0.5s$ (d) $t = 1.63s$

(e) $t = 1s$ (f) $t = 2s$

Figure 5-30: Vapor cushion growth on Rough Porous Hydrophobic 3 heater at $359\frac{kW}{m^2}$.

5.11 Surface Parameter Comparisons

In order to fully comprehend the separate effects of the different surface characteristics, it is helpful to simultaneously consider different boiling curves. This helps to bring an understanding of relative boiling performance between different surfaces.

5.11.1 Effect of Wettability

The effect of wettability can be considered by comparing four different sets of boiling surfaces. First are the Smooth Non-porous Hydrophilic and Smooth Non-porous Hydrophobic surfaces. Both of these surfaces were exceptionally smooth and non-porous. However, their static contact angles differed by about 105° ($< 5°$ for hydrophilic surface and $\approx 110°$ for hydrophobic surface). The average CHF values were $1009\frac{kW}{m^2}$ and $968\frac{kW}{m^2}$, for the hydrophilic and hydrophobic surfaces respectively. As can be seen in Figure 5-31, the boiling curves for the two surfaces are similar, though overall the Smooth Non-porous Hydrophobic boiling curves are slightly to the left of the Smooth Non-porous Hydrophilic curves. This results in

a marginally higher HTC for the Smooth Porous Hydrophobic heater at a given heat flux as compared to the Smooth Porous Hydrophilic heater. This may be a result of the hydrophilic coating deactivating nucleation sites on that surface, thereby lowering the overall HTC. However, the difference in boiling performance between these heater is not particularly pronounced, leading to the conclusion that wettability effects may only be minor for surfaces that lack distinct texture.

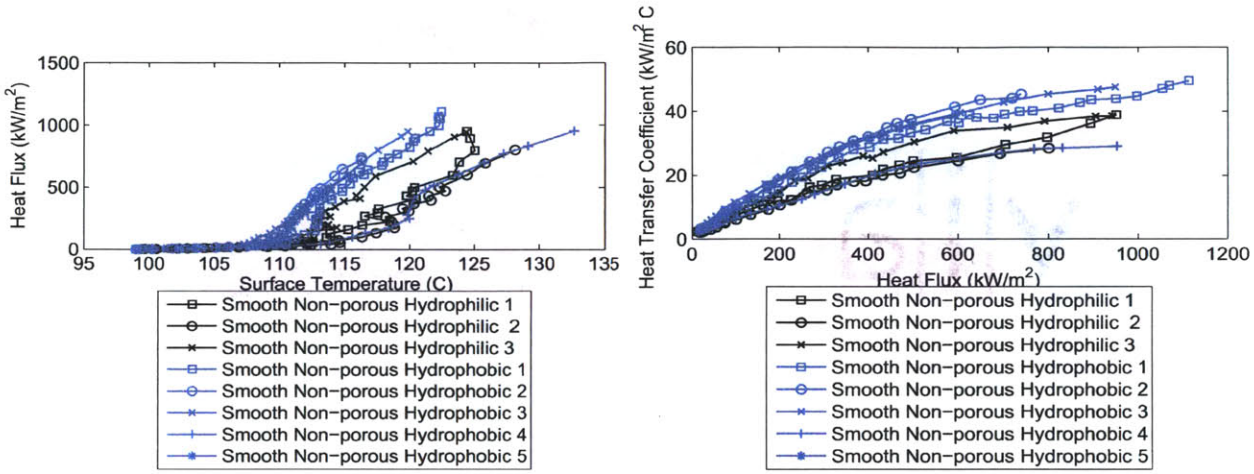

(a) Boiling Curve

(b) Heat Transfer Coefficient

Figure 5-31: Boiling Curve and Heat Transfer Coefficient for Wettability Comparison of Smooth, Non-porous surfaces.

Similar conclusions can be drawn from the comparison between the Rough Non-porous Hydrophilic and Rough Non-porous Hydrophobic surfaces, which had average CHF values of $1063\frac{kW}{m^2}$ and $1067\frac{kW}{m^2}$, respectively. Again, the boiling curves for these surfaces reveal that overall, the hydrophobic surface had enhanced HTC, especially at higher heat fluxes (while there is some overlap on the boiling curves, the overall trend holds true). This further implies that the hydrophobic surfaces were able to activate more nucleation sites than the hydrophilic surfaces. However, the CHF values for these two surfaces were nearly identical. Therefore, even when coupled with surface roughness, wettability seems not to have a significant effect on a non-porous surface.

The comparison of the Smooth Porous Hydrophilic and Smooth Porous Hydrophobic surfaces reveals a markedly different effect of wettability in the presence of porosity. The

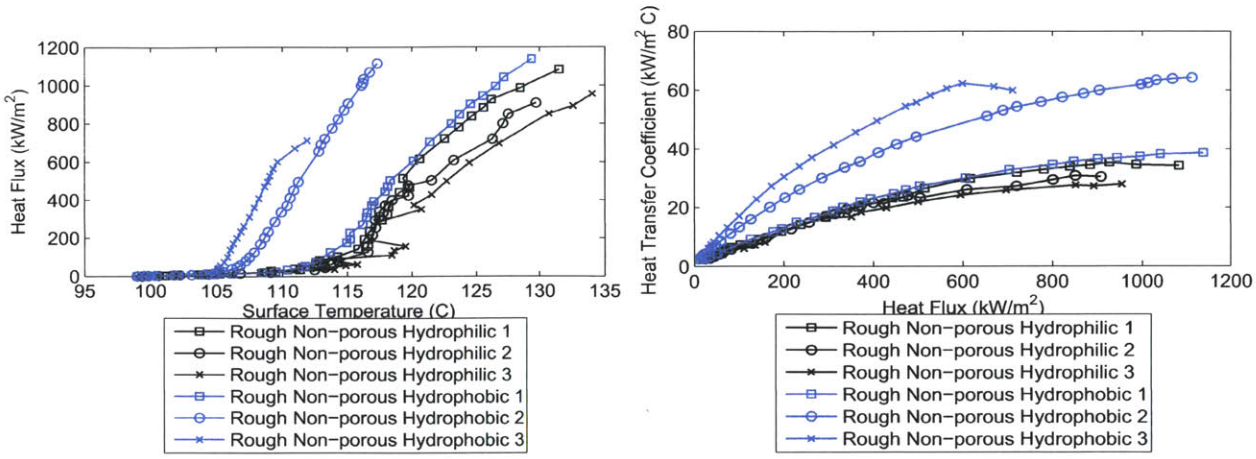

(a) Boiling Curve

(b) Heat Transfer Coefficient

Figure 5-32: Boiling Curve and Heat Transfer Coefficient for Wettability Comparison of Rough, Non-porous surfaces.

Smooth Porous Hydrophilic surface had the highest average CHF value in the investigation at $1617\frac{kW}{m^2}$. Conversely, the average CHF value of the Smooth Porous Hydrophobic surface was one of the lowest, at only $34\frac{kW}{m^2}$. Porosity and wettability changes compound to dramatically affect the performance of a boiling surface. This is evident from Figure 5-33, where the boiling curves for the two surfaces exhibit completely different trends. Zoomed in views of the boiling curves are also presented in Figure 5-33 to help fully illustrate the differences between these two surfaces.

CHF is achieved extremely early for the Smooth Porous Hydrophobic heaters, leading to the customary dramatic drop in HTC. At a heat flux of only about $75\frac{kW}{m^2}$, the Smooth Porous Hydrophobic HTC is nearly zero, while the Smooth Porous Hydrophilic HTC has only just begun to grow towards its maximum. Additionally, because the Smooth Porous Hydrophobic heaters reach CHF at such a low heat flux, burnout does not necessarily occur at the same time. Rather, the surface remains in the film boiling regime for a range of heat fluxes, with the heater surface reaching significant temperature values. Conversely, the achievement of CHF for the Smooth Porous Hydrophilic heaters occurs at a substantially higher heat flux and typically also results in instantaneous heater destruction.

The pronounced effect of wettability, when combined with porous surfaces is readily ev-

ident from these test results. This is an important contrast to the effect of wettability on non-porous surfaces, where it is essentially negligible. On the hydrophilic surface, the porosity provides a level of interconnectivity, allowing liquid to be transfered between nucleation sites. All the while, the hydrophilicity of the surface promotes rewetting. Any deactivation of nucleation sites by the hydrophilic coating (as was suspected on the hydrophilic non-porous surfaces) is likely countered by the abundance of nucleation sites created by the porous structure. On the hydrophobic surface, the presence of porosity further increases the contact angle. Additionally, the porous structure may help to store vapor, and thereby aid the transition to film boiling.

Finally, a similar behavior was discovered in the comparison between the Rough Porous Hydrophilic and Rough Porous Hydrophobic surfaces. Of these two, the hydrophilic surface had an average CHF of $1590\frac{kW}{m^2}$, while the hydrophobic surface had an average CHF of $20\frac{kW}{m^2} - 40\frac{kW}{m^2}$. Again, in considering the CHF values and boiling curve trends in Figure 5-34, there is large distinction between the surfaces with different wettabilities. While the Rough Porous Hydrophobic surfaces reached localized CHF very early, it seems that the posts helped to inhibit global heater burnout. As a result, the majority of the points on the Rough Porous Hyrdophobic boiling curves were obtained in the film boiling regime, which partially accounts for their markedly low, and decreasing values. Overall, this comparison again illustrates the effect of wettability on porous surfaces. The performance of these rough heaters was very similar to the identical, but smooth heaters. This leads to the conclusion that the post structures did not play a significant role in the performance of the heater. However, the effect of surface roughness will be considered explicitly in Section 5.11.3.

As these four comparisons attest to, the degree to which wettability affects a surface is largely dependent on surface porosity. In the absences of porosity, wettability did not significantly affect the performance of the heaters tested, including those with surface roughness. In engineering surfaces for heat transfer, it is important to recognize this fact.

5.11.2 Effect of Porosity

A first insight into the effect of porosity can be gained from comparing the Smooth Non-porous Hydrophilic and Smooth Porous Hydrophilic heaters. The boiling curves presented

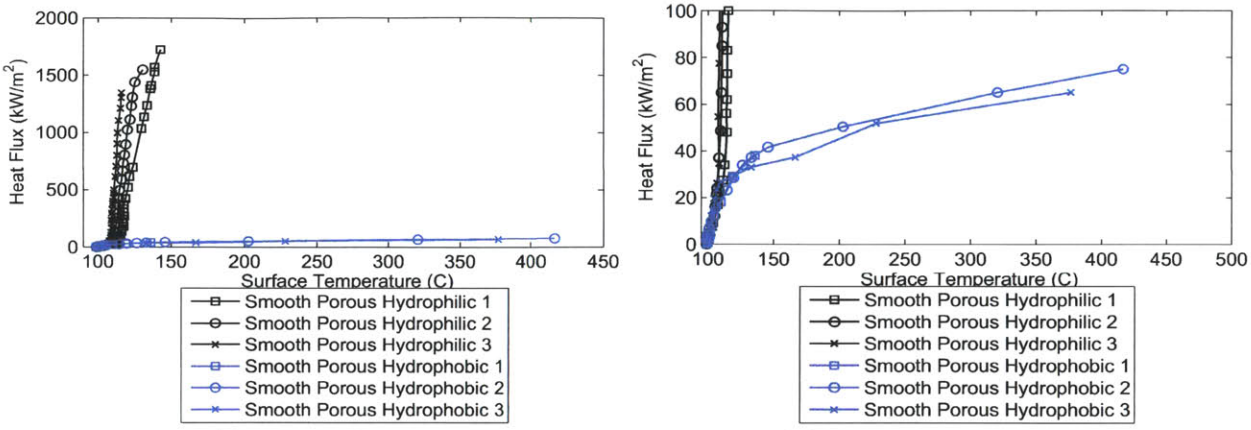

(a) Boiling Curve

(b) Boiling Curve Zoom In

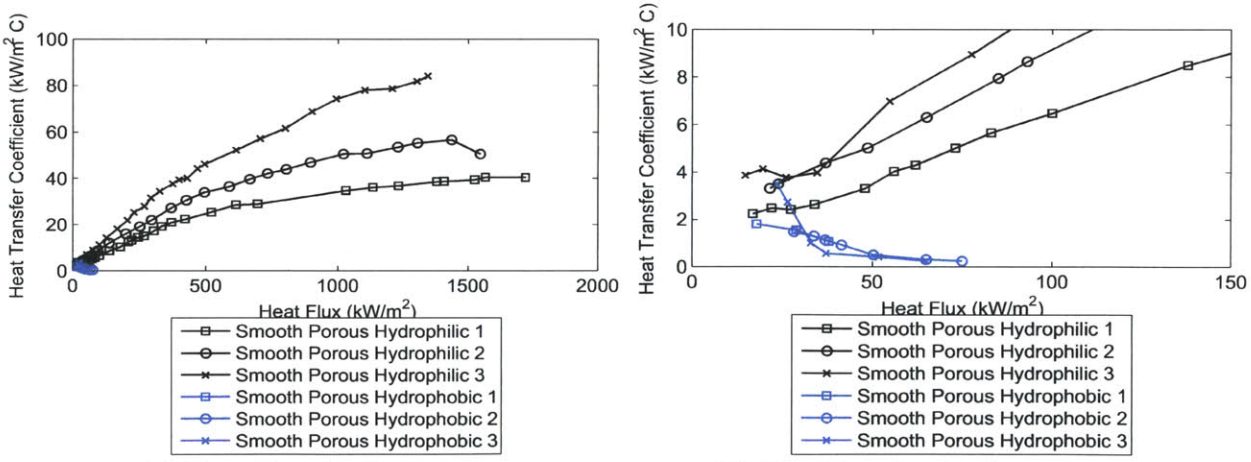

(c) Heat Transfer Coefficient

(d) Heat Transfer Coefficient Zoom In

Figure 5-33: Boiling Curve and Heat Transfer Coefficient for Wettability Comparison of Smooth, Porous surfaces.

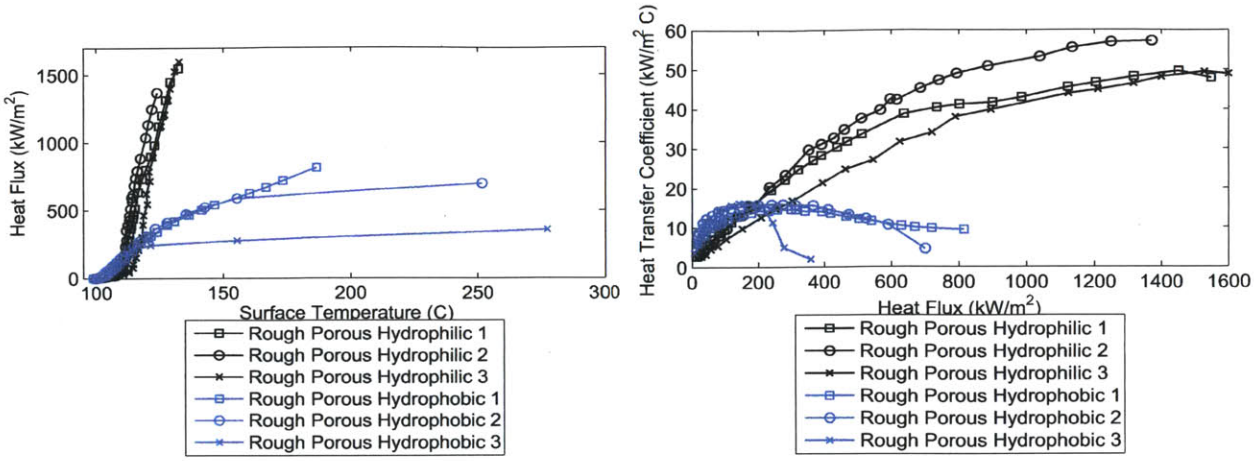

(a) Boiling Curve

(b) Heat Transfer Coefficient

Figure 5-34: Boiling Curve and Heat Transfer Coefficient for Wettability Comparison of Rough, Porous surfaces.

in Figure 5-35, demonstrate that the heaters with a porous structure have a slightly higher average overall HTC (though there is some overlap between the curves). This is likely a result of the porous structure providing nucleation sites. The larger contrast between these two surfaces comes in their CHF values. The Smooth Non-porous Hydrophilic and Smooth Porous Hydrophilic surfaces had an average CHF values of $1009\frac{kW}{m^2}$ and $1617\frac{kW}{m^2}$, respectively. Therefore, in the case of a smooth, hydrophilic surface, the addition of porosity lead to a 60.2% increase in CHF.

A similar effect was observed between the Rough Non-porous Hydrophilic and Rough Porous Hydrophilic surfaces. As has been alluded to previously, the inclusion of surface roughness seems not to have altered the heater performance. Therefore, the boiling curves of these rough heaters, presented in Figure 5-36 exhibit very similar trends as their smooth counterparts in Figure 5-35. The average CHF values for the Rough Non-porous Hydrophilic and Rough Porous Hydrophilic heaters were $1063\frac{kW}{m^2}$ and $1590\frac{kW}{m^2}$, respectively. As a result, in the case of rough, hydrophilic surfaces, porosity increased CHF by 49.5%.

Porosity also had a significant effect on smooth, hydrophobic surfaces. The Smooth Non-porous Hydrophobic and Smooth Porous Hydrophobic surfaces had average CHF values of $968\frac{kW}{m^2}$ and $34\frac{kW}{m^2}$, respectively. Of these surfaces, the non-porous heaters performed very

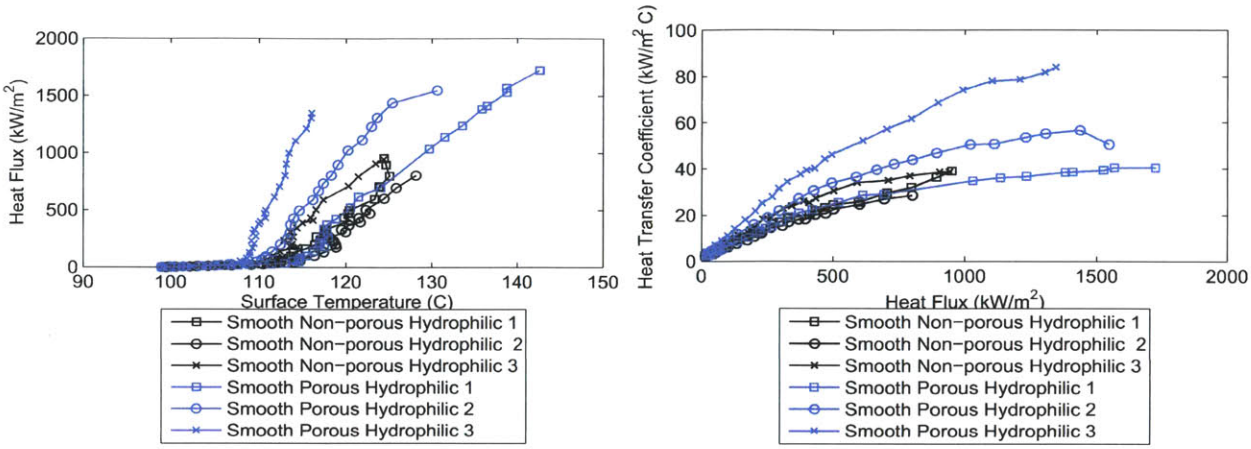

(a) Boiling Curve (b) Heat Transfer Coefficient

Figure 5-35: Boiling Curve and Heat Transfer Coefficient for Porosity Comparison of Smooth, Hydrophilic surfaces.

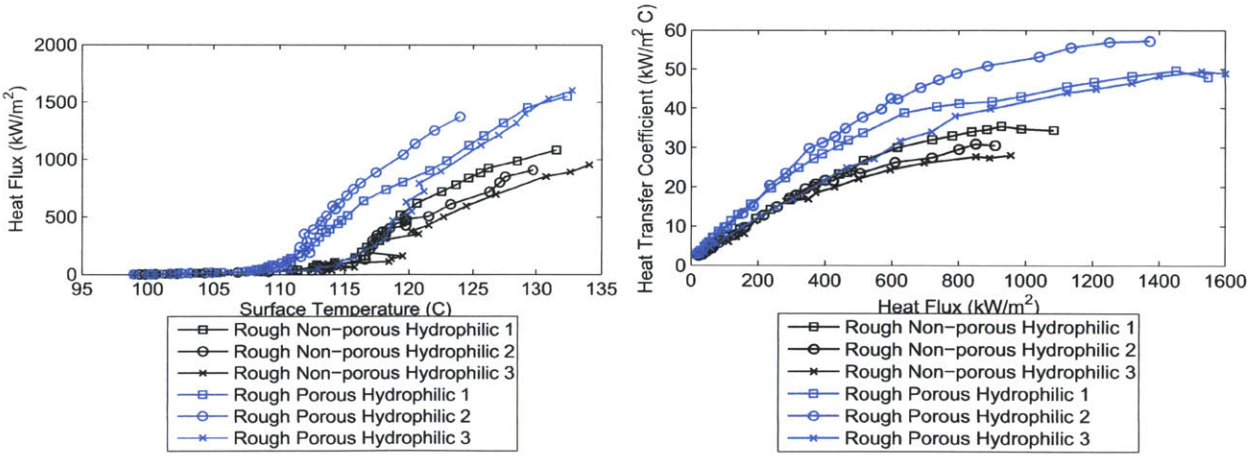

(a) Boiling Curve (b) Heat Transfer Coefficient

Figure 5-36: Boiling Curve and Heat Transfer Coefficient for Porosity Comparison of Rough, Hydrophilic surfaces.

similar to Uncoated Sapphire and even similar hydrophilic surfaces. However, the porous surface achieved CHF at a remarkably low heat flux value. The suspected factors behind this occurrence have already been discussed and will not be reiterated. Rather, it is simply important to recognize the major effect porosity can have on smooth, hydrophobic surfaces. The boiling curves for these two surfaces are presented in Figure 5-37, where zoomed in views are also included for clarity.

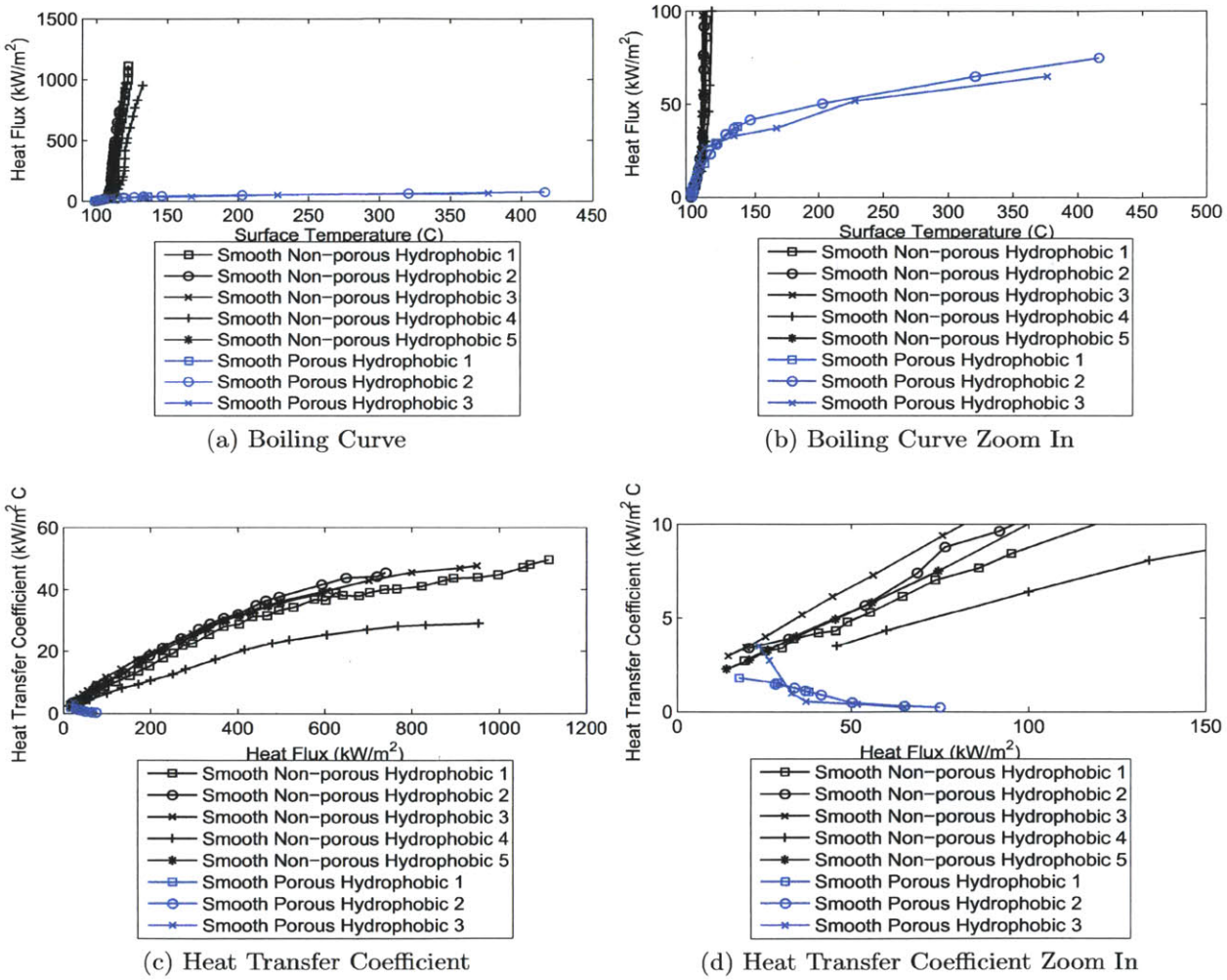

(a) Boiling Curve

(b) Boiling Curve Zoom In

(c) Heat Transfer Coefficient

(d) Heat Transfer Coefficient Zoom In

Figure 5-37: Boiling Curve and Heat Transfer Coefficient for Porosity Comparison of Smooth, Hydrophobic surfaces.

Finally, the Rough Non-porous Hydrophobic and Rough Porous Hydrophobic surfaces trended very similar to their smooth equals. The addition of porosity to the hydrophobic

surface dramatically reduced CHF to $20\frac{kW}{m^2} - 60\frac{kW}{m^2}$ for the Rough Porous Hydrophobic surface, as compared to to $1067\frac{kW}{m^2}$ for the Rough Non-porous Hydrophobic surface. Again, it seems that the surface posts had a negligible effect on the performance.

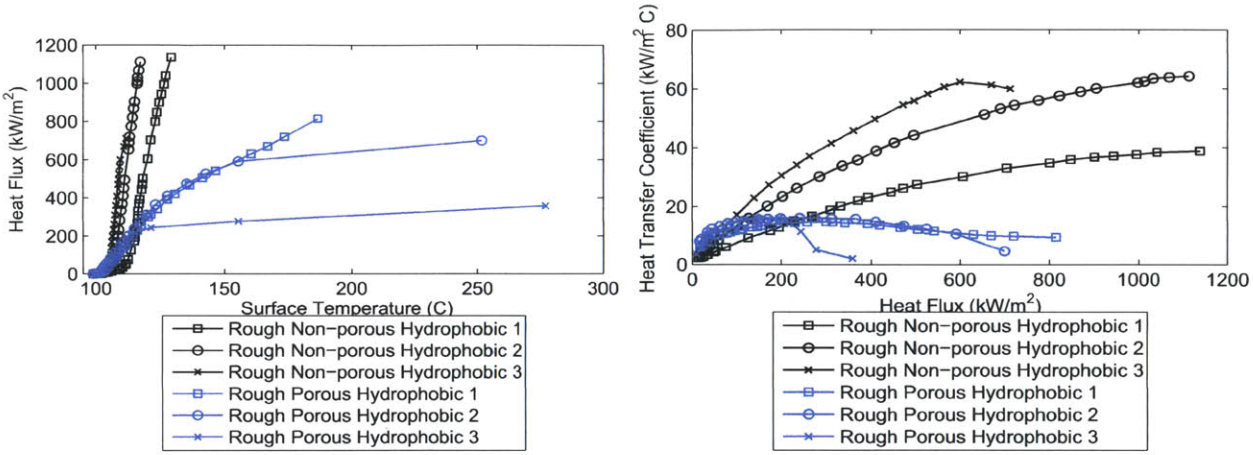

(a) Boiling Curve

(b) Heat Transfer Coefficient

Figure 5-38: Boiling Curve and Heat Transfer Coefficient for Porosity Comparison of Rough, Hydrophobic surfaces.

Form these results, it is important to recognize that porosity can significantly enhance the performance of hydrophilic surface. This is likely due to the fact that the pores help to pump liquid to the nucleation sites thus delaying the formation of hot/dry spots. Conversely, porosity can dramatically lower the CHF value of a hydrophobic surface. Of all the surface characteristics investigated, the relative effect of porosity on surfaces with different wettabilities is the most pronounced. An interesting next step would be to investigate the effect of porosity at a variety of discrete surface wettabilities, not just hydrophobic and hydrophilic. Understanding exactly how porosity affects a surface as a function of wettability could provide crucial knowledge for designing heat transfer surfaces. It would be particularly interesting to determine the point on the wettability spectrum where porosity changes from being beneficial to detrimental in terms of CHF.

5.11.3 Effect of Roughness

Roughness had the least effect on boiling of the surface characteristics examined. Smooth Non-porous Hydrophilic and Rough Non-porous Hydrophilic surfaces had very similar CHF values, $1009\frac{kW}{m^2}$ and $1063\frac{kW}{m^2}$, respectively. Additionally, as seen in Figure 5-39, the boiling curves for these two surfaces are almost entirely overlapped. This implies very similar performance regardless of surface roughness.

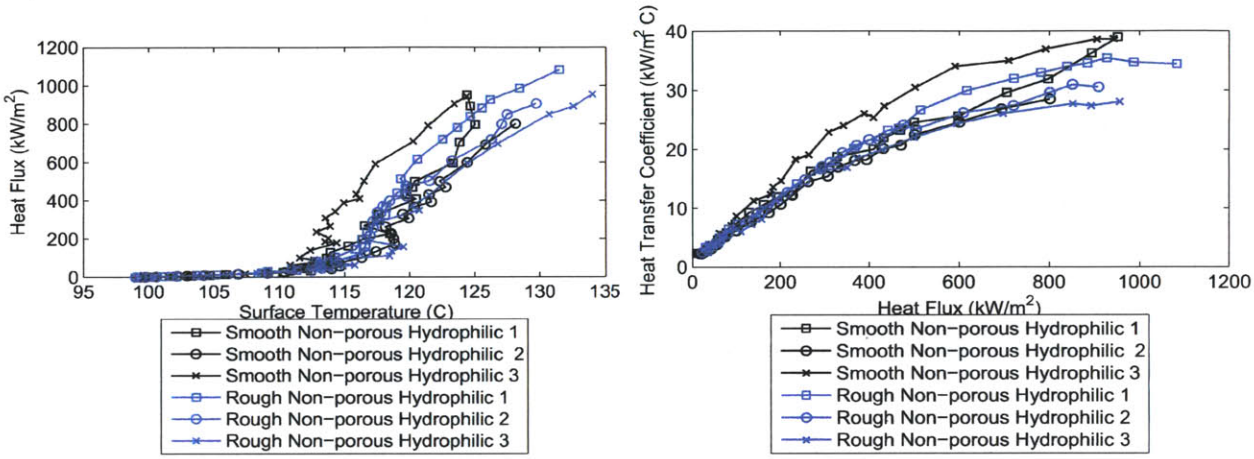

(a) Boiling Curve

(b) Heat Transfer Coefficient

Figure 5-39: Boiling Curve and Heat Transfer Coefficient for Roughness Comparison of Non-porous, Hydrophilic surfaces.

The Smooth Non-porous Hydrophobic and Rough Non-porous Hydrophobic comparison exhibited a similar trend, though there was more variation in the boiling curves. Overall, the boiling curves for the rough and smooth surfaces are intertwined, implying similarity in boiling performance. This can be observed in Figure 5-40. The larger grouping is likely a function of non-uniformity in the hydrophobic coating. Finally, the respective average CHF values for the smooth and rough heaters were $968\frac{kW}{m^2}$ and $1067\frac{kW}{m^2}$.

Roughness did not induce any major difference between the Smooth Porous Hydrophilic and Rough Porous Hydrophilic heaters. In Figure 5-41, the boiling curves for the two surfaces are quite overlapped. Additionally, the respective average CHF values for the smooth and rough surfaces were $1617\frac{kW}{m^2}$ and $1590\frac{kW}{m^2}$, which are nearly identical. Unlike, porosity, roughness does not appear to have a direct effect on CHF enhancement or boiling efficiency.

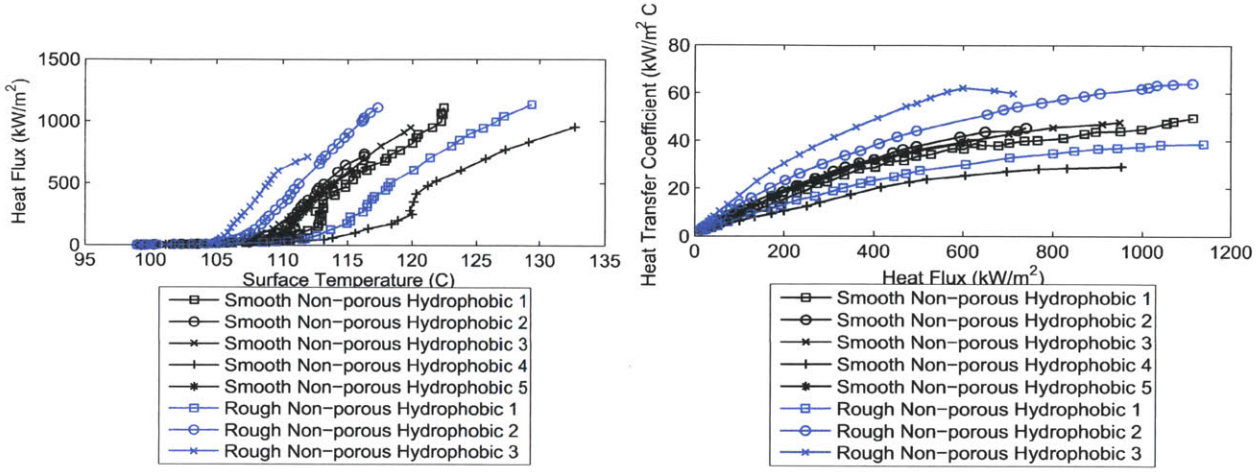

(a) Boiling Curve (b) Heat Transfer Coefficient

Figure 5-40: Boiling Curve and Heat Transfer Coefficient for Roughness Comparison of Non-porous, Hydrophobic surfaces.

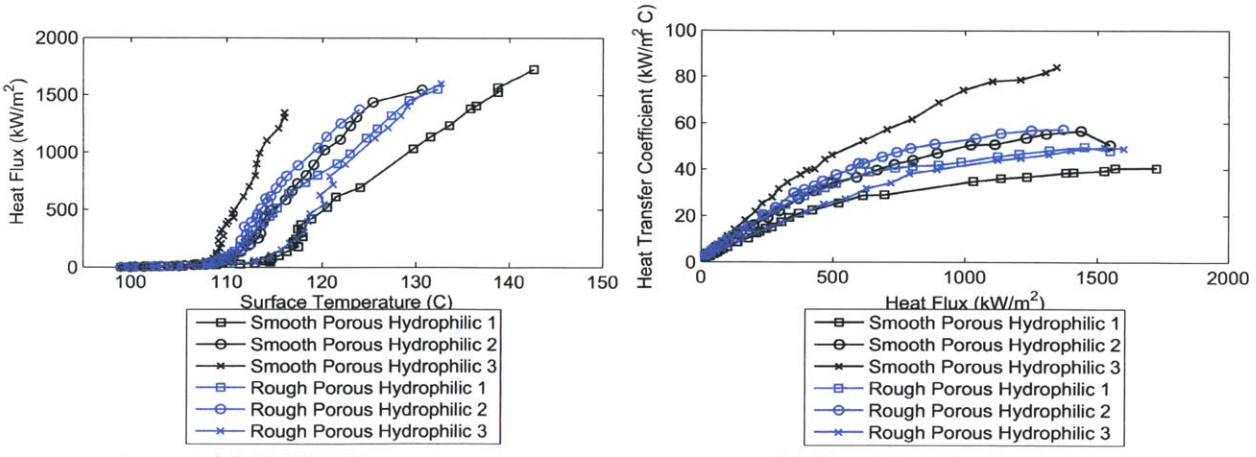

(a) Boiling Curve (b) Heat Transfer Coefficient

Figure 5-41: Boiling Curve and Heat Transfer Coefficient for Roughness Comparison of Porous, Hydrophilic surfaces.

The one instance in which roughness did play a role can be seen in the comparison between the Smooth Porous Hydrophobic and Rough Porous Hydrophobic surfaces. However, here roughness did not affect CHF. The average CHF for the Smooth Porous Hydrophobic surfaces was $34\frac{kW}{m^2}$. The average CHF value for the Rough Porous Hydrophobic surfaces was between $20\frac{kW}{m^2} - 40\frac{kW}{m^2}$. As such, surface roughness clearly did not affect the CHF values for porous hydrophobic surfaces. However, after local CHF, the post features helped to prevent heater burnout. This allowed the Rough Porous Hydrophobic heater to be driven to higher heat fluxes before catastrophic failure, as previously discussed. While this is an effect of the posts, it occurred after CHF.

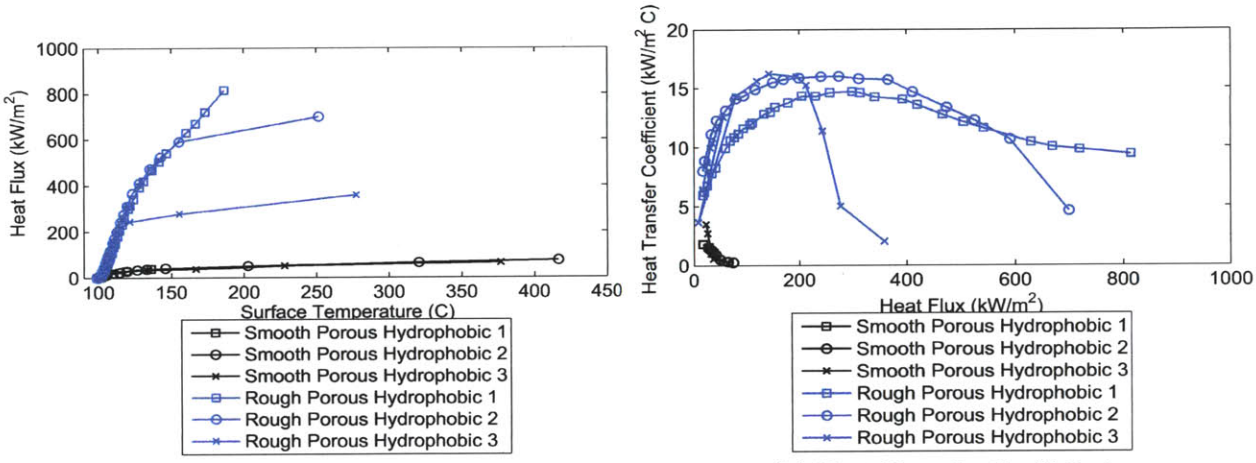

(a) Boiling Curve

(b) Heat Transfer Coefficient

Figure 5-42: Boiling Curve and Heat Transfer Coefficient for Roughness Comparison of Porous, Hydrophobic surfaces.

Overall, these results provide very clear evidence that surface roughness in the form of micro posts does not affect CHF or boiling performance in a major manner. In every instance, there was no significant difference between smooth and rough heater surfaces tested. This is in stark contrast to the effects of the other surface characteristics, which had distinct effects, especially in certain combinations. Surface roughness is commonly referred to as an enhancer of CHF. However, it might be the case that what is being referred to as roughness, is actually something different. Here, roughness was induced by widely spaced micro posts, designed to create a surface texture, but not cause any capillary effects. In other instances,

when roughness is being cited as performance enhancing, it might be that the surface texture has topography such that capillary action is induced. If such were the case, while the surface in question may or may not have distinct pores, the close proximity of surface features might pull liquid downwards towards the surface. Additionally, in some instances a surface texture might even form a quasi-porous structure, thus reaping the benefits of interconnected nucleation sites. Therefore, it is crucial to make the distinction between surface roughness and porosity in designing boiling surfaces.

5.12 Summary and Future Recommendations

The Separate Effect investigation characterized the effects of wettability, porosity, and roughness on CHF and HTC. Some effects were constant, while other were dependent on - and could even be completely reversed by - the presence of other surface properties. In summary:

1. Wettability had a limited effect on non-porous surfaces. However, it had prominent effects when combined with a porous structure.

2. Porosity dramatically altered a surface's boiling performance. However, the manner in which it affected a surface was largely dependent on the surface wettability. If a surface was hydrophilic, the porous structure was beneficial. If the surface was hydrophobic, the porous structure reduced CHF and harmed performance.

3. Surface roughness did not have an appreciable affect on CHF or boiling performance, regardless of the wettability or porosity.

The results of this examination open new opportunities for future research. Continued understanding of the mechanisms, which control boiling will help to accelerate the engineering of performance enhancing boiling surfaces. Opportunities for future work include, but are obviously not limited to:

1. Create multi-tiered porous structures, with pore size varying in the vertical direction. Fabricating surfaces with small particles on the bottom near the heater substrate could facilitate capillary action, helping to move liquid around the surface. Upper levels,

nearer the working fluid could be made of larger particles, creating pores nearer to the size of natural nucleation sites. Additionally, any number of distinct patterns of porosity levels could be imagined.

2. Create porous structures with items other than simple spherical particles. Deposition of ellipsoids, rods and particles with other geometries could create a porous structure that behaves differently.

3. Examine the effect of porosity over the spectrum of wettability from super hydrophilic to super hydrophobic. Specifically, identify the point at which porosity transitions from being beneficial to being detrimental to CHF.

4. Examine the exact nature of surface roughness structures reported by other researchers and determine if porosity-type effects could be present.

Chapter 6

Spot Patterning Heater Preparation, Testing, and Results

While the Individual Parameter investigation is primarily concerned with understanding the driving forces that control CHF and HTC the Spot Pattern investigation attempts to harness this knowledge to engineer optimal heater surfaces. Heaters for the Spot Pattern investigation were all nominally porous hydrophilic, patterned with porous hydrophobic spots. Previous research in MIT Reactor Hydraulics Laboratory had examined the effect of layer thickness, particle size and hydrophobic vs. hydrophilic spots on the boiling performance of similar patterned multilayer surfaces. [24] Here, the effect of varying pitch on which the hydrophobic spots were patterned was investigated. Additionally, the effect of varying the spot diameter and the ratio between the spot diameter and pitch was examined.

6.1 Surface Preparation

The nominally porous hydrophilic surface was prepared using the LBL procedure. In this investigation, surfaces with fifty layers of $50nm$ SiO_2 particles were exclusively used. Following LBL coating, a layer of fluorosilane was deposited per the procedure with an exposure time of thirty minutes. Finally, the spot patterns were created using the UVO procedure.

Multilayer Region	Average Static Contact Angle (Degrees)
Porous Hydrophilic	$< 5°$
Porous Hydrophobic	137.5°

Table 6.1: Contact angle measurements for hydrophilic and hydrophobic regions of the spot patterned multilayer surface.

6.2 Surface Analysis

Prior to boiling tests, the patterned multilayer surfaces were characterized in an effort to further quantify the test results. The contact angles for the porous hydrophilic and porous hydrophobic regions are identical to those determined during the analysis of homogeneous porous hydrophilic and porous hydrophobic surfaces in the Individual Parameter investigation. These contact angles are summarized in Table 6.1.

These surfaces had the same roughness and porosity characteristics as the Smooth Porous Hydrophilic and Hydrophobic surfaces in the Individual Parameter Investigation. As detailed in Section 5.4, these surface characteristics were examined by *Phillips (2011)*. On average, the surface roughness was determined to be, $R_a = 0.07\mu m$ and $R_z = 0.91\mu m$. The surface porosity was approximately 50% by volume.

6.3 PBF Test Results

For each pattern type, three individual heaters were prepared and tested. All tests were to CHF, and thus destructive. The primary purpose of this investigation is to determine the efficacy of the spot pattern on enhancing CHF and HTC. Therefore, it is important to compare the results of each pattern to the performance of an uncoated heater, as well as a heater coated with fifty layers of $50nm$ SiO_2 particles (but not patterned with hydrophobic spots). As seen in the Individual Parameter investigation, a porous hydrophilic surface coating is very effective at enhancing CHF. By benchmarking the patterned heaters against this homogeneous, porous hydrophilic surface, the performance of the spots can be isolated. The boiling curves and CHF results of these reference heaters are presented in Figure 6-1 and Table 6.2.

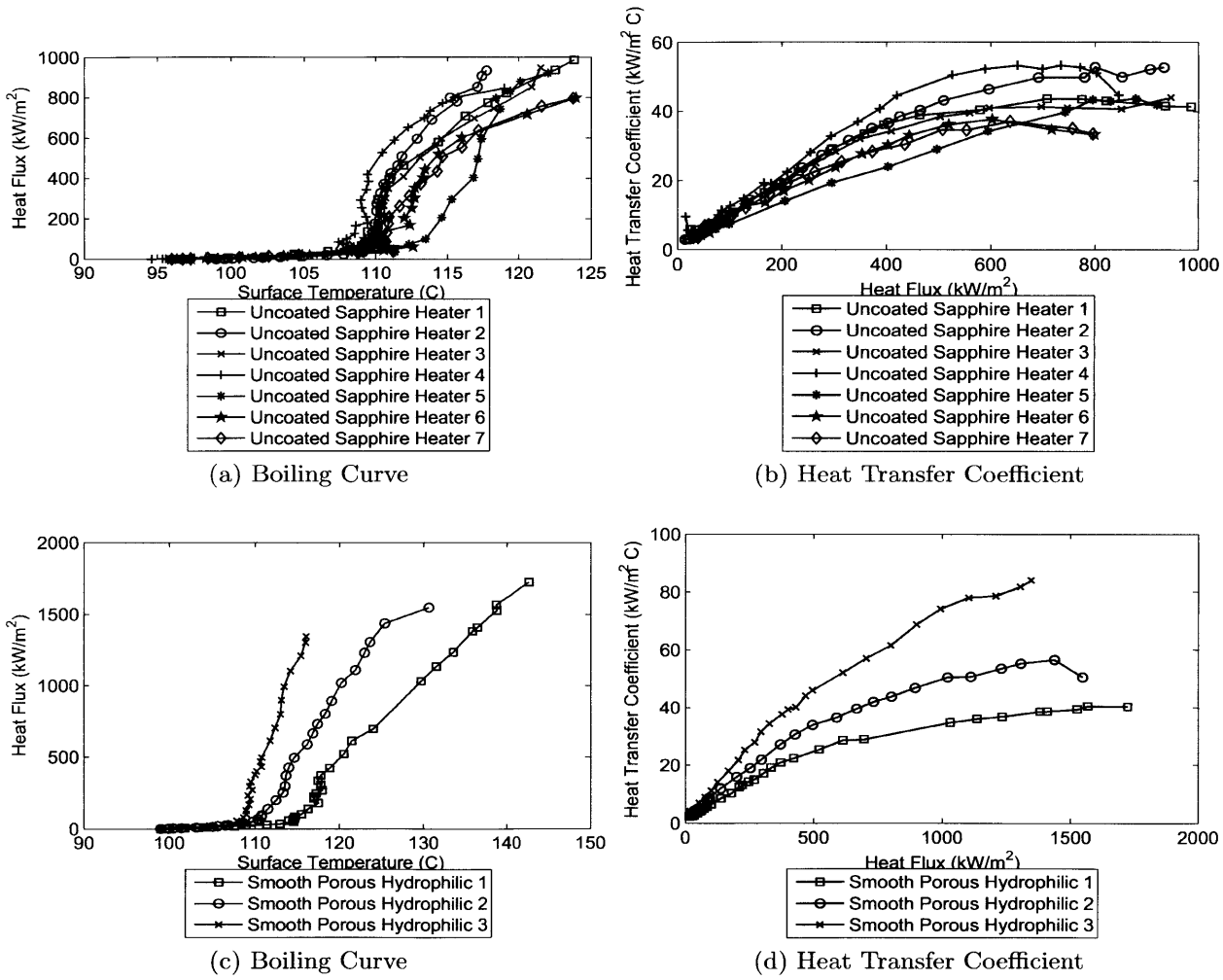

(a) Boiling Curve

(b) Heat Transfer Coefficient

(c) Boiling Curve

(d) Heat Transfer Coefficient

Figure 6-1: Reference Boiling Curves for Uncoated Sapphire and Smooth Porous Hydrophilic Heaters.

Pattern	CHF	Average CHF ($\frac{kW}{m^2}$)	St. Dev
Uncoated Heater 1	873	920	8.3%
Uncoated Heater 2	1032		
Uncoated Heater 2	920		
Uncoated Heater 3	986		
Uncoated Heater 4	799		
Uncoated Heater 5	885		
Uncoated Heater 6	947		
Smooth Porous Hydrophilic 1	1800	1617	10.9%
Smooth Porous Hydrophilic 2	1605		
Smooth Porous Hydrophilic 3	1446		

Table 6.2: Uncoated sapphire heater and smooth porous hydrophilic reference CHF values.

In analyzing the performance of the spot pattern heaters, it is convenient to group the surfaces into two groups. The first group, which includes Patterns A-D, offers insight into the effect of varying the spot pitch. The second group, Patterns E-H, includes surfaces on which the spot diameter is altered. Additionally, analysis of the heaters tested in this investigation can be supplemented by the results of *Phillips (2011)* investigation on other spot patterns.

6.3.1 Effect of Varying Spot Pitch (Patterns A-D)

As identified in the Individual Parameter investigation, an underlying Porous Hydrophilic surface is very well performing. In some instances, around 100% enhancement on CHF was achieved with a Porous Hydrophilic surface. The inclusion of hydrophobic spots patterned on these surfaces were intended to serve a distinct nucleation sites towards which the liquid would be channeled by the hydrophilic porous substrate. In analyzing the performance of Patterns A-D, CHF will be first considered and then HTC performance analyzed.

It was not expected that the hydrophobic spot patterns would enhance CHF and this hypothesis was confirmed. Remarkably, the the average percent CHF enhancement of Patterns A-D were all tightly grouped within a range of 5.87%. A complete list of CHF values for the different patterns tested in this group is presented in Table 6.3. These results imply that spot pitch has essentially no effect on CHF for these spot patterned heaters. The CHF improvement over an Uncoated Sapphire heater is likely a result of the underlying hydrophilic

porosity of the heaters. This performance is similar to that of the Smooth Porous Hydrophilic heater from the Individual Parameter investigation. The slightly decreased CHF values from a homogeneous porous hydrophilic surface is likely a by-product of the hydrophobic spots. While serving as nucleation sites, the hydrophobic regions would also prevent local rewetting. It is difficult to determine from the IR signal if the hot spots that eventually brought on CHF initiated on a hydrophobic spot. However, such a theory seems plausible.

Heater	CHF $\frac{kW}{m^2}$	Avg. CHF $\frac{kW}{m^2}$	St. Dev $\frac{kW}{m^2}$	Percent Enhancement	Avg. Percent Enhancement
A_1	1589	1660	88	72.71%	80.7%
A_2	1758			91.09%	
A_3	1634			77.61 %	
B_1	1666	1663	4	81.09%	79.24%
B_2	1661			80.54%	
B_d	1620			76.09%	
C_1	1571	1643	200	70.81%	78.56%
C_2	1869			103.15%	
C_3	1488			61.71%	
D_1	1696	1612	149	84.38%	75.24%
D_2	1440			56.55%	
D_3	1700			84.78 %	

Table 6.3: CHF Values for Patterns A-D.

While the hydrophobic spots were intended to enhance the overall HTC, such improvement was not realized during testing. In examining the boiling curves of Patterns A-D, it is evident that the HTC was not significantly enhanced on a consistent basis. In most instances, the HTC versus Heat Flux curve for each heater pattern tracked closely with both the Uncoated Sapphire and SiO_2 heater surface curves. Certain heaters from patterns B and C exhibit enhanced HTC over the reference curves. However, this improvement is not consistent and not illustrated by sister patterns. It seems that these quasi-outliers are either a result of variability in the fluorosilane spot patterning or - more likely - simply a product of the stochastic nature of the boiling phenomenon. Only translation of the boiling curves for all heaters in a series definitively to the left would indicate true HTC improvement.

The ability of a surface to transfer heat is a function of the bubble departure diameter (how much heat vapor and thus latent is removed per nucleation), the bubble departure

frequency (how quickly each unit nucleation occurs), and the nucleation site density (representing the total number of nucleation sites per unit area on the surface). In order to understand the HTC results of the spot patterning investigation, each specific factor must be considered. Bubble departure diameter is primarily a function of the boiling environment (specifically, pressure and contact angle) and thus is not assumed to vary with spot pitch.

Theoretically, the nucleation site density should have varied between with heaters, if one were to assume that the hydrophobic spots were the only bubble departure sites. The theoretical nucleation site density can be determined by calculating the number of hydrophobic spots present on the active heater for each pitch. These values are presented in Table 6.4.

Pitch (mm)	Theoretical Number of Sites	Theoretical Nucleation Site Density ($\frac{sites}{cm^2}$)
0.2	12,500	6250
0.5	2000	1000
0.75	888	444
1.25	320	160
1.5	222	111
2	125	62

Table 6.4: Theoretical number of nucleation sites for various pitches employed.

From the IR signals of the heater surfaces (Figure 6-2), it is evident that the spot pattern succeeded in dictating the exact bubble nucleation sites on the heater surface. From the distinctive spot patterns on the IR signal, it is confirmed that nucleation was in fact occurring at the hydrophobic spots. The clearly ordered, dark spots represent cooler regions on the heater surface, which are indicative of point at which heat is being removed through bubble nucleation. However, this ordered pattern of nucleation typically did not fully develop until moderate heat fluxes in the range of $800\frac{kW}{m^2}$ to $1000\frac{kW}{m^2}$. Prior to this threshold, nucleation occurred at largely random locations across the heater surface. Once the spot pattern of nucleation was established, it maintained most of its integrity through CHF. Even as hot spots of local dryout became present near CHF, the underlying hexagonal pitch pattern of nucleation spots was clearly discernible. The presence of this distinct pattern right up until heater burnout at CHF implies that the fluorosilane spot pattern layer maintained its integrity through the PBF testing. Figure 6-2 offers a visualization of the spot pattern in

the IR signal.

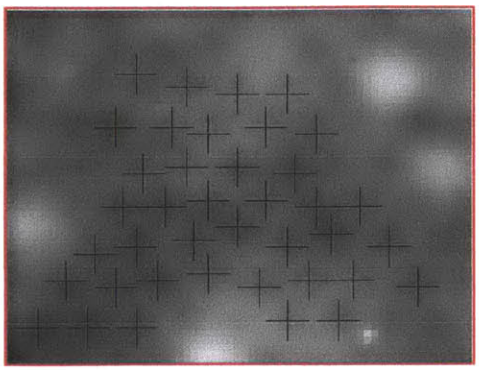

(a) Zoom of area bound by red box

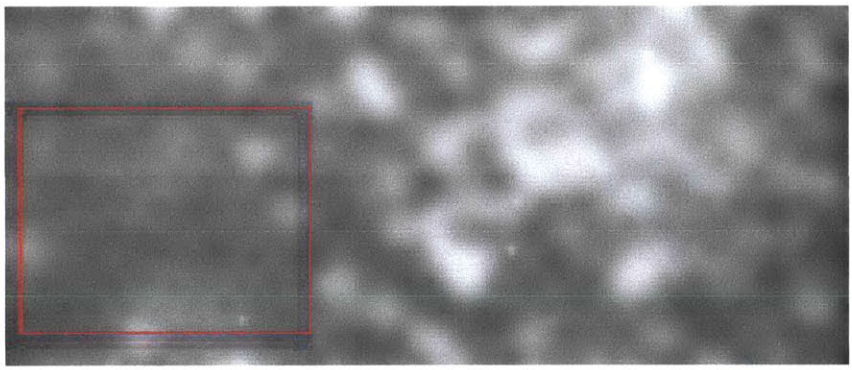

(b) $1554kW/m^2$

Figure 6-2: Spot pattern visible at $1554kW/m^2$. Nucleation sites are marked in zoomed image of area bound by red box. The bright white areas to the right of the image are hot spots present near CHF. Note, many more nucleation sites exist than those marked.

The spot patterns with tighter pitches ($0.5mm$ and $0.75mm$) were harder to recognize, and consistent spot patterns could not be consistently discerned. The difficulty in identifying these patterns may have been a result of local bubble coalesce during nucleation. This would have laterally distributed the vapor bubble during formation, thereby pulling heat from a wider region of the surface. If such bubble coalescence was occurring, it did not consistently enhance HTC, as attested to by the boiling curves in Figure 6-3. However, while most of the heater groups had highly repeatable boiling curves, the traces for Pattern A ($260\mu m$ spot, $0.5mm$ pitch) were more spread out. The variance in these boiling curves seems slightly beyond the natural stochastic behavior of boiling and implies that perhaps a degree of coalescence on the surface was leading to unrepeatable boiling behavior. There

is much room for further investigation of the effects of bubble coalescence on spot pattern performance. Specifically, imaging with a high speed camera could help determine the exact behavior of the bubbles on the surface.

However, when considered as a whole, the boiling curves for all heaters tested in this first set of heaters are tightly grouped together. Figures 6-3 through 6-7 demonstrate the small variance in HTC for heaters in Patterns A-D. This is somewhat counterintuitive as nucleation site density should vary with pitch. If bubble departure diameter is assumed to be unchanged, then either nucleation site density *did not* vary between patterns, bubble frequency was pitch dependent, or nucleation site density and bubble departure frequency varied in a manner such that their cumulative effect was relatively small.

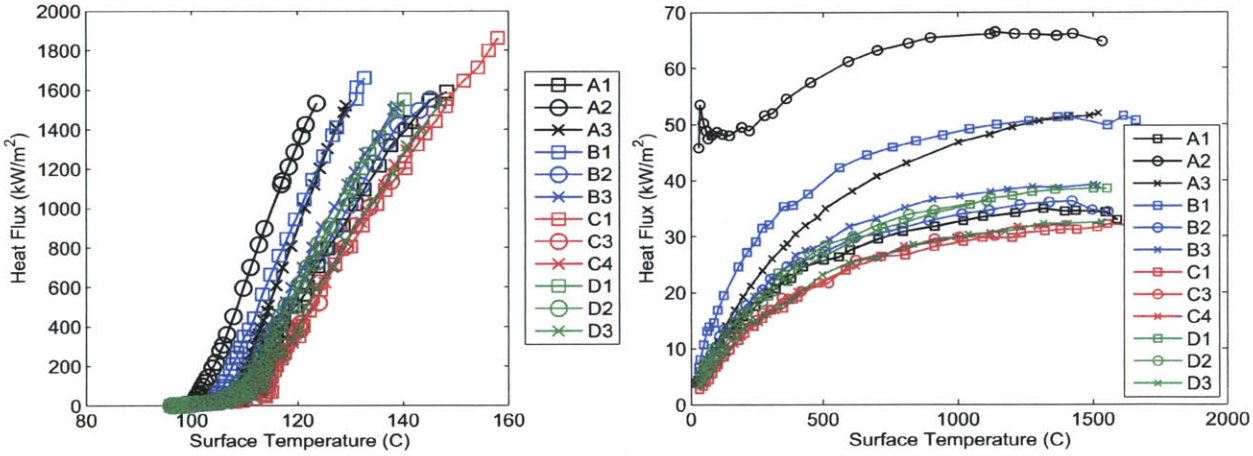

(a) Boiling Curve (b) Heat Transfer Coefficient

Figure 6-3: Boiling Curve and Heat Transfer Coefficient for Patterns A-D

In considering bubble departure frequency, is it appropriate to start with *Calka and Judd's (1985)* analysis of the effect of adjacent nucleation sites on bubble frequency, as described in Section 2.1.4. Recall that the researchers analyzed the relationship between bubble departure diameter, d_d, and intersite spacing, a, establishing three categories of site interaction [12]:

1. For $\frac{a}{d_{departure}} < 1$, the interaction between sites is attractive.

2. For $1 < \frac{a}{d_{departure}} < 3$, the interaction between sites is repulsive.

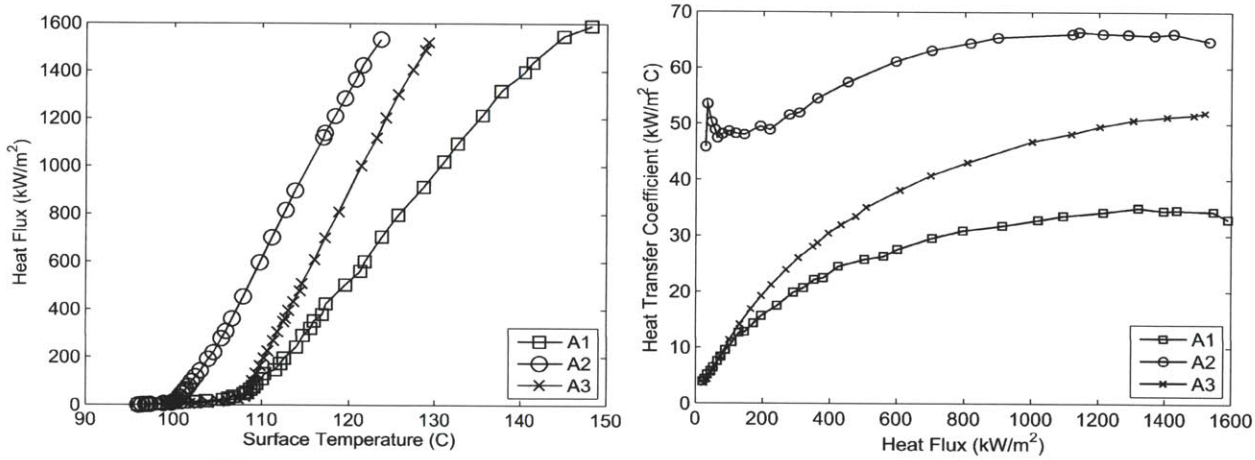

(a) Boiling Curve

(b) Heat Transfer Coefficient

Figure 6-4: Individual Boiling and Heat Transfer Coefficient Curves for Pattern A ($260\mu m$ spot, $0.5mm$ pitch).

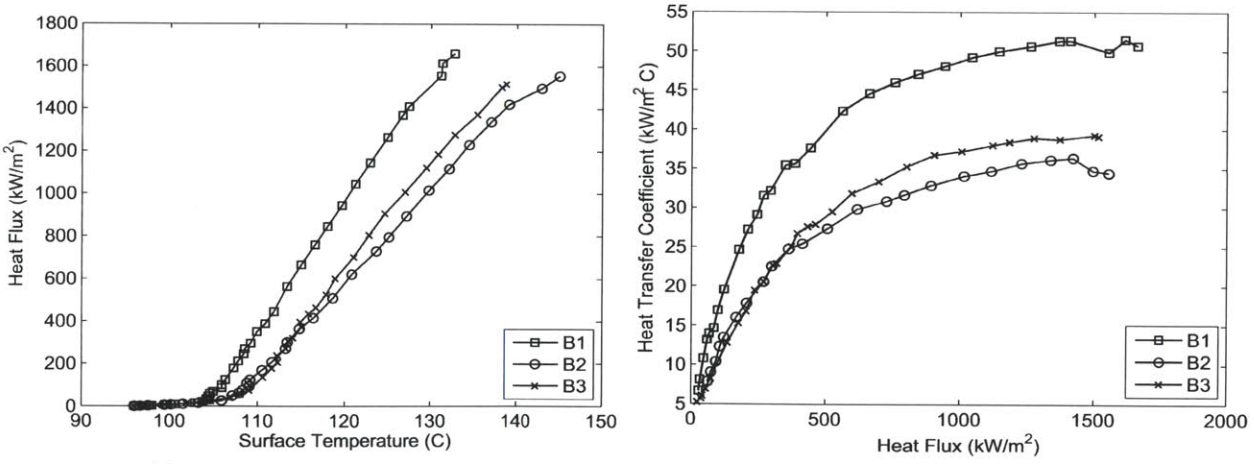

(a) Pattern B Boiling Curve

(b) Pattern B Heat Transfer Coefficient

Figure 6-5: Individual Boiling and Heat Transfer Coefficient Curves for Pattern B ($260\mu m$ spot, $0.75mm$ pitch).

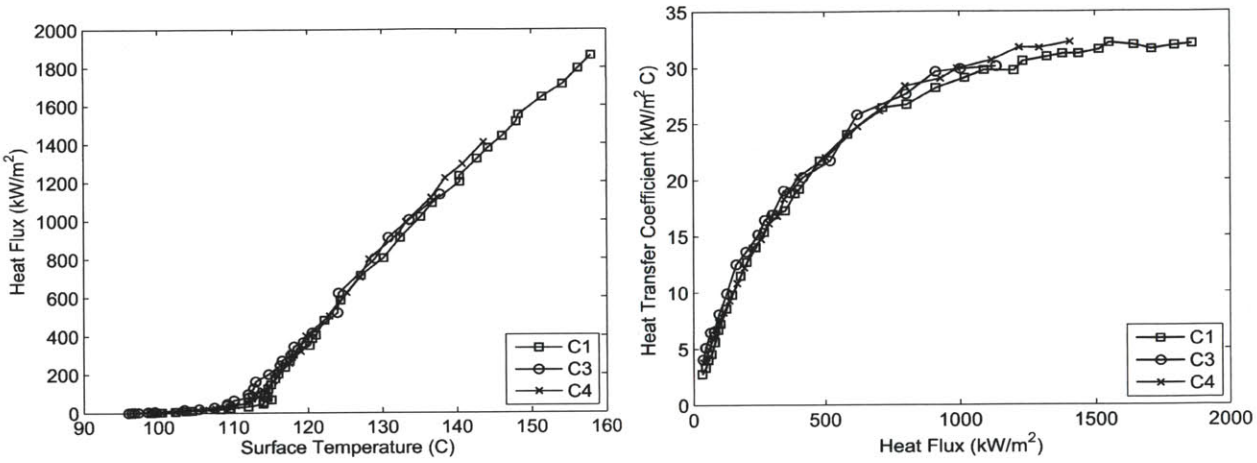

(a) Pattern C Boiling Curve

(b) Pattern C Heat Transfer Coefficient

Figure 6-6: Individual Boiling and Heat Transfer Coefficient Curves for Pattern C ($260\mu m$ spot, $1.25mm$ pitch).

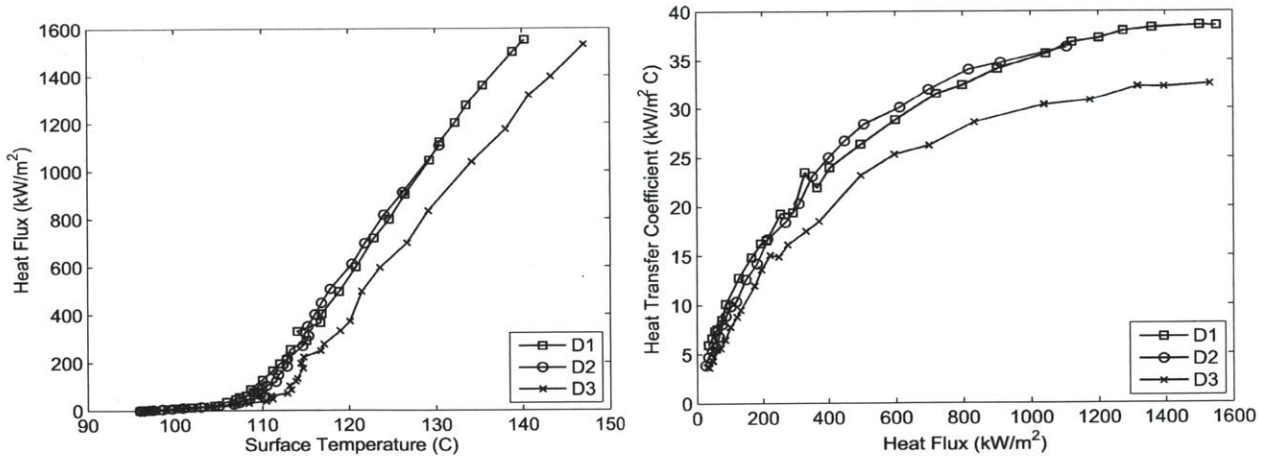

(a) Pattern D Boiling Curve

(b) Pattern D Heat Transfer Coefficient

Figure 6-7: Individual Boiling and Heat Transfer Coefficient Curves for Pattern D ($260\mu m$ spot, $1.5mm$ pitch).

3. For $3 < \frac{a}{d_{departure}}$, the sites are independent.

While this analysis was validated by the researchers for a test surface with only two sites, it serves as starting point for considering the performance of the patterned spot surfaces. As the hydrophobic spots are spaced uniformly, the basic spacing analysis can be applied. The bubble departure diameter is assumed to be $d_{departure} = 1mm$ and the bubble size to intersite spacing ratios for each pattern is presented in Table 6.5.

Pattern	$\frac{a}{d_d}$ [dimensionless]	Regime
A	0.5	Attractive
B	0.75	Attractive
C	1.25	Repulsive
D	1.5	Repulsive

Table 6.5: Bubble departure diameter to intersite spacing ratios for Patterns A-D.

As such, it seems that the spacing of Patterns A and B would enhance bubble departure frequency as the coalescence resulting from a given site would help to seed other sites with vapor. Conversely, per this reasoning, the bubble departure frequency of Patterns C and D should have suffered. The bubble departure frequency was measured at low heat fluxes (around $100\frac{kW}{m^2}$) was measured using Fast Fourier Transform (FFT) analysis of the IR signal. While this analysis did not show any appreciable difference in bubble departure frequency, this heat flux was substantially below the threshold at which ordered nucleation from the spot patterns truly developed. A lack of clarity in the IR signal at higher heat fluxes near CHF prevented similar FFT analysis once the spot pattern was present. Measuring bubble departure accurately would most likely be accomplished with side imaging the boiling surface with a high speed video camera, an apparatus outside the scope of this investigation. Therefore, the nature of the bubble departure frequency must be hypothesized based on knowledge of intersite behavior. Overall, it is possible that the intersite spacing caused there to be a difference in bubble departure frequency, though it is unclear if the change in frequency was appreciable.

It is also important to consider the relationship between nucleation site density and spot pitch. While nucleation clearly occurred at the hydrophobic spots, it seems likely that these

were sites of encouraged, not exclusive nucleation. It is hypothesized that nucleation still occurred over the entire active heater in the standard stochastic nature of pool boiling. However, nucleation at the hydrophobic spots occurred more frequently than at other areas, significantly cooling the surrounding surface and allowing it to be visible on the IR signal. Because all of the HTC curves for the different patterns were tightly grouped, it seems likely that nucleation site density did not in fact vary by surface as much as pattern pitch would suggest. More likely, nucleation also occurred at points other than the hydrophobic spots, but simply to a lesser extent.

Interestingly, these observations of HTC performance contrast those of other researchers also examining hydrophobic spots patterned on a hydrophilic surface. As described in Section 2.4.3, *Betz (2010)* found such similar spot patterns to enhance CHF and HTC by by 65% and 100%, respectively over a nominally hydrophilic surface. [37] As hypothesized in this investigation, *Betz* and her colleagues intended the hydrophobic spots to increase nucleation site density, which appears to have occurred. However, a critical difference between the *Betz* investigation and this one is porosity. The surfaces fabricated by *Betz (2010)* had a roughness below $5nm$ and were not porous. Therefore, it is very unfavorable for nucleation to occur at a non-hydrophobic site. Here, the spot patterned surfaces were uniformly porous, as fabricated by the LBL process with $50nm$ SiO_2 particles. While the hydrophobic spots certainly promoted nucleation at those points, it seems that the porosity of the entire surface could also have promoted nucleation in hydrophilic regions. It is established that porosity can aid nucleation by providing interconnected voids. As such, nucleation site density of a given surface would have tended towards the natural optimum rather than the theoretical number of hydrophobic spots. This would account for the small variance in HTC between the spot patterned surfaces and the homogenous porous hydrophilic heater.

As this investigation focused on the overall performance of the heaters, it is difficult to infer an understanding of the local bubble dynamics. However, it seems reasonable to conclude that across different patterns: bubble departure diameter was constant, bubble frequency may have varied slightly, but not significantly, and nucleation site density adjusted itself naturally, with nucleation not exclusively occurring at the hydrophobic spots. Cumulatively, these effects served to maintain HTC within a close band across different spot patterns.

The results of testing Patterns A-D raised a few questions. First, it was hypothesized that the growing bubble may become temporarily pinned at the hydrophobic/hydrophilic interface of the spot. This could result in a decrease of the bubble departure frequency (for all Patterns A-D, as all had spots of $260\mu m$). The interface could present a barrier to bubble growth. Moreover, this perimeter might be encountered later in the bubble cycle, when growth is less energetic. As such, it was decided to create heaters with comparably pitches as previously tested, but with smaller spot diameters. Ideally, the growing bubble would encounter the hydrophobic/hydrophilic interface earlier, in the more energetic (faster) period of bubble growth. Additionally, the ratio between spot size and pitch was significantly higher in *Betz's (2010)* test matrix than in this investigation. Therefore, a spot pattern with dimensions more similar to those used by *Betz (2010)* was also fabricated. This pattern would help to isolate whether the difference in results in fact stemmed from the porosity of the surface.

6.3.2 Effect of Varying Spot Size and Dimension Ratio (Patterns E-H)

Again, CHF and the overall HTC of each spot pattern must be considered to characterize its performance. As with the first spot pattern text matrix, Patterns E-H offered CHF enhancement over an Uncoated Sapphire heater, but less improvement than simply a homogeneous porous hydrophilic surface. The variance of average CHF values between different spot patterns was relatively small, with the range spanned being only 12.85%. A complete list of CHF values for Patterns E-H is presented in Table 6.6.

In considering the boiling curves of these spot patterns, it is again evident that the HTC curves tracked very closely to the references. The three iterations of Pattern E tracked almost exactly with the homogeneous porous hydrophilic heater (except for slight improvement at high heat fluxes). This implies that the $90\mu m$ hydrophobic spots had little to no effect on the performance of the surface, other than to decrease CHF. Moreover, this pattern is similar to one tested by *Betz (2010)*, which saw HTC improvement. Because no improvement was seen here, it seems likely that the porosity of the surfaces - both Pattern E and the reference

Heater	CHF $\frac{kW}{m^2}$	Avg. CHF $\frac{kW}{m^2}$	St. Dev $\frac{kW}{m^2}$	Percent Enhancement	Avg. Percent Enhancement
E_1	1472	1503	62	60.01%	63.32%
E_2	1461			58.82%	
E_3	1574			71.13%	
F_1	1428	1509	143	55.18%	63.97%
F_2	1424			54.76%	
F_3	1674			81.97%	
G_1	1454	1315	196	58.01%	76.84%
G_2	1177			71.42%	
G_3	1177			101.09%	
H_1	1597	1462	158	73.59%	58.91%
H_2	1501			63.15%	
H_3	1288			39.99%	

Table 6.6: CHF Values for Patterns E-H.

porous hydrophilic heater - overshadow the hydrophobic spots in capability to seed nucleation sites. Additionally, it was not possible to identify this spot pattern on the IR signal. It seems that the spots were simply too small and tightly spaced for individual recognition.

Patterns F-H on the whole realized similar and in most cases slightly decreased HTC performance than the reference surfaces. While on heater tested with Pattern G performed recognizably higher than its peers and references, this behavior was not repeatable. That these surfaces did not perform better than their counterparts with larger spot diameters disproves the hypothesis that the bubbles were being pinned at the hydrophobic/hydrophilic interface. Reducing the spot diameter had negligible effect of the HTC of the surface. As with Pattern E, it was very difficult to identify these spot patterns on the IR signal. At higher heat fluxes and with close examination it was possible to begin to make out the pattern. However, the contrast between the spots and the surrounding area was not nearly as sharp as witnessed with Patterns A-D. This does not imply that nucleation did not occur at these sites, rather the phenomena occurred at a scale smaller than unaided visual recognition.

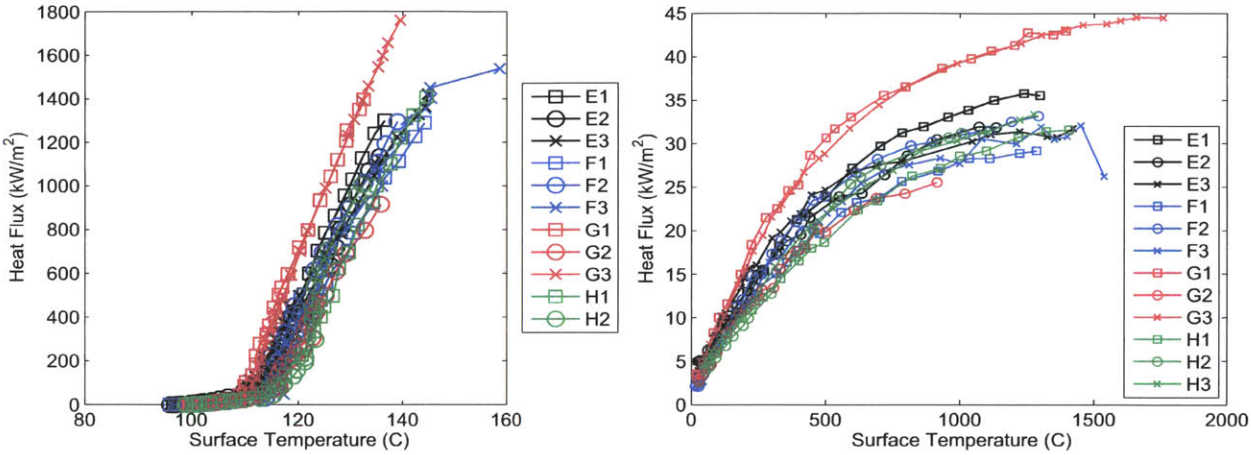

(a) Boiling Curve (b) Heat Transfer Coefficient

Figure 6-8: Boiling Curve and Heat Transfer Coefficient for Patterns E-H.

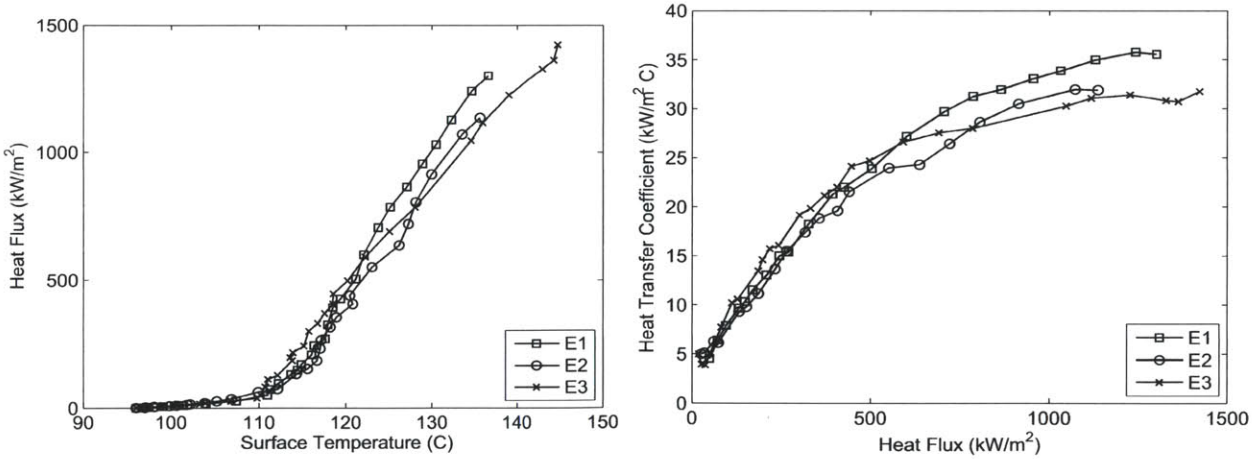

(a) Pattern E Boiling Curve (b) Pattern E Heat Transfer Coefficient

Figure 6-9: Individual Boiling and Heat Transfer Coefficient Curves for Pattern E ($90\mu m$ diameter, $0.2mm$ pitch).

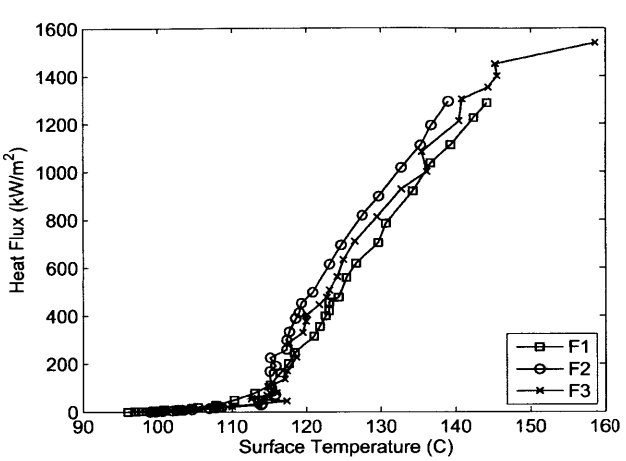

(a) Pattern F Boiling Curve

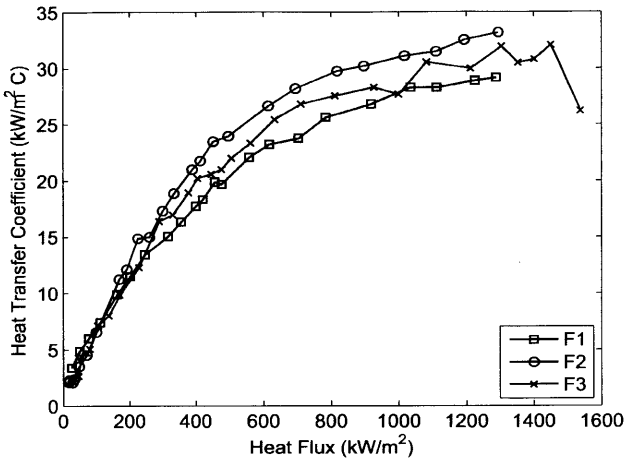

(b) Pattern F Heat Transfer Coefficient

Figure 6-10: Individual Boiling and Heat Transfer Coefficient Curves for Pattern F ($120\mu m$ diameter, $0.75mm$ pitch).

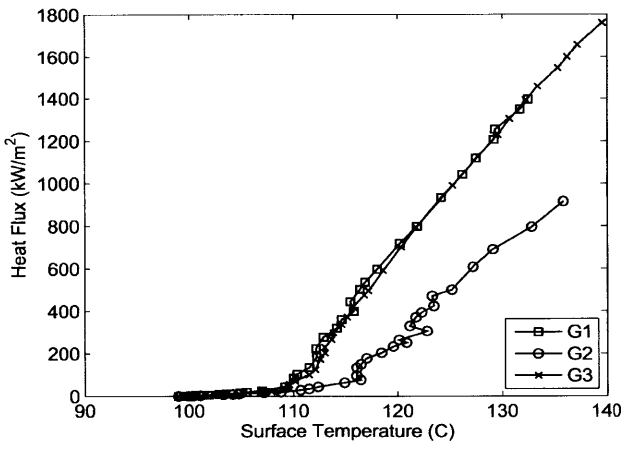

(a) Pattern G Boiling Curve

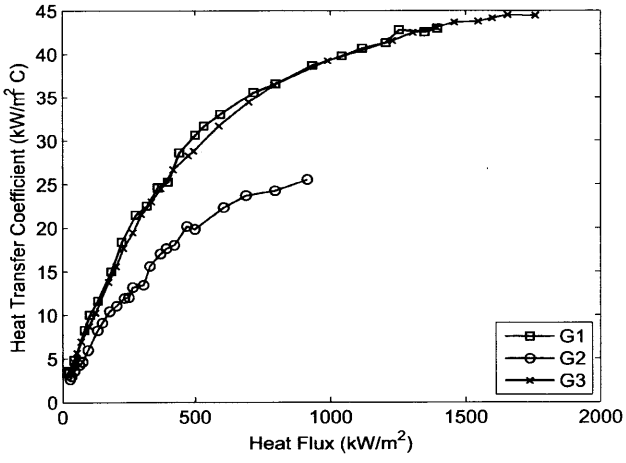

(b) Pattern G Heat Transfer Coefficient

Figure 6-11: Individual Boiling and Heat Transfer Coefficient Curves for Pattern G ($120\mu m$ diameter, $2mm$ pitch).

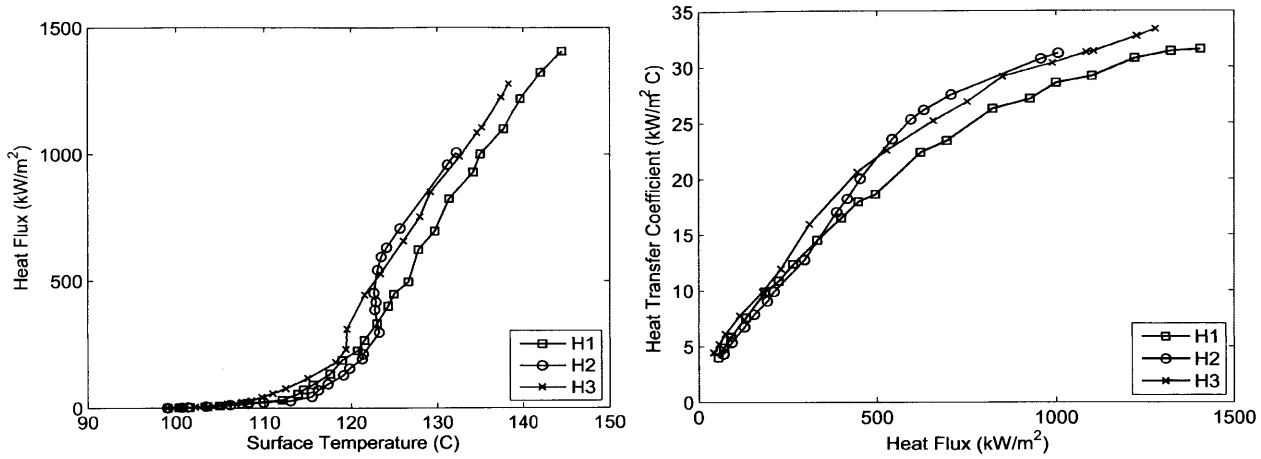

(a) Pattern H Boiling Curve

(b) Pattern H Heat Transfer Coefficient

Figure 6-12: Individual Boiling and Heat Transfer Coefficient Curves for Pattern H ($120\mu m$ diameter, $0.2mm$ pitch).

6.4 Summary and Future Recommendations

Overall, it does not appear that networks of porous hydrophobic spots on a porous hydrophilic surface offer improvement over a homogeneous porous hydrophilic surface. Any CHF improvement over an uncoated heater is a function of the porous hydrophilicity and is only decreased by the inclusion of the hydrophobic spots. The IR signals confirmed that nucleation did in fact occur at the hydrophobic spots, at least with enough propensity to reduce the temperature of the spot as compared to the surrounding region. However, as the HTC of the different surface did not vary significantly, it seems that the nucleation site densities of the surfaces were also similar. This contrasts the theoretical variance in nucleation site densities as predicted by the spot pitches. Therefore, it seems that nucleation likely also occurred outside the hydrophobic spots, just with less frequency and in a more stochastic nature than at the engineered sites. As such, the nucleation site density of all surfaces would have tended towards a naturally selected optimum, thereby equalizing the HTC curves for all of the heaters. Because of the ability of a porous surface to seed nucleation sites seems to overshadow that of engineered hydrophobic spots. As a result, engineered nucleation sites may have more impact if patterned on surfaces that are non-porous.

This investigation continued previous spot patterning work by *Phillips (2011)* and there

is still room for continued research. The following suggestions offer some insight into the potential direction of future work:

1. Investigate the effect of spot patterns on non-porous surfaces. Without a porous structure to seed nucleation, spot patterns may have more of an effect on HTC.

2. Only circle spots were examined here and by *Phillips (2011)*. The use of non-circular shapes might have more of an effect on HTC (e.g squares, starts, lines).

3. Apply the spot patterning techniques to applications were distinct regions of boiling are required, such as in microfluidic devices. While the spots have had limited effect on CHF and HTC, they are capable of providing precisely located and distinct nucleation sites. This could be beneficial in complex, small scale boiling systems.

4. Examine the manufacturability of the spot patterns.

Chapter 7

Conclusion

Two distinct investigations into boiling performance were carried out: a Separate Effect investigation and a Spot Patterning effort. The Separate Effect investigation characterized the separate effects that surface wettability, porosity, and roughness have on CHF and boiling performance. The effect of wettability on the surface was dependent on the presence of porosity. For non-porous surfaces, wettability appeared to have no appreciable effect on either CHF or HTC. Porous hydrophilic surfaces tended to enhance CHF, while porous hydrophobic surfaces were extremely poor performing. Porosity had powerful effects on the boiling surface and was beneficial for hydrophilic surfaces and quite detrimental for hydrophobic surfaces. Surface roughness did not play an appreciable role in dictating the performance of the boiling surface, even when combined with other surface parameters. In summary, contrary to common beliefs, intrinsic wettability and surface roughness per se have very little effect on CHF and HTC, while the combination of porosity and wettability can determine CHF changes by an order of magnitude.

In the Spot Patterning portion of the project, different arrays of hydrophobic spots were patterned on a nominally porous hydrophilic surface in an attempt to engineer nucleation sites. While nucleation was achieved at the prescribed sites, the patterns tested did not significantly enhance CHF or HTC over a nominally porous hydrophilic surface. Therefore, while patterning techniques are effective at locally directing boiling phenomena, they did not enhance overall performance. However, the patterning techniques employed could be beneficial in an application where specific boiling areas are required (for example, in microfluidic

boiling devices).

The results of this investigation can be used as tools to engineer more effective and better performing heat transfer surfaces. Understanding the exact nature of how different surface features can work in unison to promote boiling can be important for a design engineer. The Separate Effect investigation also lays the foundation for further characterization of surface parameter CHF effects. Additionally, the various micro and nanoengineering techniques employed offer starting points for the fabrication of such boiling surfaces. Engineering of boiling surfaces is a long lived field of science and the advent of nanoscale engineering capability only further extends this discipline. Moving forward, it will be important to continue strengthening the understanding of how surface parameters effect boiling, but also to begin reducing this knowledge for practical application in industry. This includes selecting the optimal set of parameters for an application, modifying surface coatings to ensure their long-lasting durability, and finally creating manufacturing processes for large scale production.

Bibliography

[1] N.E. Todreas and M. Kazimi. *Nuclear Systems I: Thermal Hydraulic Fundamentals.* Taylor and Francis, New York, 1 edition, 1993.

[2] W.M. Rohsenow, J.P. Hartnett, and Y.I. Cho. *Handbook of heat transfer.* McGraw-Hill handbooks. McGraw-Hill, 1998.

[3] J. Buongiorno L.W. Hu S.J. Kim, I.C. Bang. Surface wettability change during pool boiling of nanofluids and its effect on critical heat flux. *International Journal of Heat and Mass Transfer*, 50:4105 – 4116, 2007.

[4] P.J. Berenson. Experiments on pool-boiling heat transfer. *International Journal of Heat and Mass Transfer*, 5:985–999, 1962.

[5] Lord Rayleigh. On the pressure developed in a liquid during the collapse of a spherical cavity. *Phil. Mag*, 34:94–98, 1917.

[6] V. MIzo S. Kandlikar and M. Cartwright. Investigation of bubble departure mechanism in subcooled flow boiling of water using high speed photography. In John C. Chen, editor, *Convective Flow Boiling.* Taylor & Francis Group, 1996.

[7] M.S. Plesset and S.A. Zwick. The growth of vapor bubbles in superheated liquid. *Journal of Applied Physics*, 25:493–500, 1954.

[8] B. B. Mikic, W. M. Rohsenow, and P. Griffith. On bubble growth rates. *International Journal of Heat and Mass Transfer*, 13(4):657 – 666, 1970.

[9] A. Bejan and A. Kraus. *Heat Transfer Handbook.* Wiley-Interscience, 2003.

[10] R. Cole and W.M. Rohsenow. Correlation of bubble departure diameters for boiling of saturated liquids. *Chem. Eng. Prog. Symp*, 92:211213, 1969.

[11] J.G. Collier and J.R. Thome. *Convective Boiling and Condensation, Third Ed.* Oxford University Press, 1994.

[12] A. Calka and R.L. Judd. Some aspects of the interaction among nucleation sites during saturated nucleate boiling. *International Journal of Heat and Mass Transfer*, 28(12):2331–2342, 1985.

[13] L. Zhang and M. Shoji. Nucleation site interaction in pool boiling on the artifical surface. *International Journal of Heat and Mass Transfer*, 46:513–522, 2003.

[14] Y.A. Buyevich and B.W. Webbon. The isolated bubble regime in pool nucleate boiling. *International Journal of Heat and Mass Transfer*, 40(2):365–377, 1996.

[15] C.Y.Han and P. Griffith. The mechanism of heat transfer in nucleate pool boiling. *International Journal of Heat and Mass Transfer*, 8:887–904, 1965.

[16] S.Cioulachtjian S.Siedel and J. Bonjour. Experimental analysis of bubble growth, departure and interactions during pool boiling on artificial nucleation sites. *Experimental Thermal and Fluid Science*, 32:1504–1511, 2008.

[17] A. Mukherjee and V.K. Dhir. Study of lateral merger of vapor bubbles during nucleate pool boiling. *Journal of Heat Transfer*, 126:1023–1039, 2004.

[18] T.V. Vorburger and J. Raja. Surface finish metrology tutorial. U.S. Department of Commerce, National Institute of Standards and Technology, June 1990.

[19] S. Liter. Pool-boiling chf enhancement by modulated porous-layer coating: theory and experiment. international journal of heat and mass transfer. *44*, 22:4287–4311, 2001.

[20] S. Li M. Toprak R. Furberg, B. Palm and M. Muhammed. The use of a nano- and microporous surface layer to enhance boiling in a plate heat exchanger. *Journal of Heat Transfer*, 131, 2009.

[21] Theodore L. Bergman Frank P. Incropera, David P. Dweitt and Adrienne S. Lavine. *Fundamentals of Heat and Mass Transfer 6th ed.* John Wiley & Sons, 2007.

[22] J.Y. Chang and S.M. You. Enhanced boiling heat transfer from micro-porous surfaces:effects of a coating composition and method. *International Journal of Heat and Mass Transfer*, 40(18):4449–4460, 1997.

[23] V. Srinivassan Z. Wang H.H.Cho R. Chen, M.C. Lu and A. Majumdar. Nanowires for enhanced boiling heat transfer. *Nano Letters*, 9:548–553, 2009.

[24] B.Phillips. Nano-engineering the boiling surface for optimal heat transfer rate and critical heat flux. Master's thesis, Department of Nuclear Science and Engineering, Massachusetts Institute of Technology, 2011.

[25] Y.V. Polezhaev and S.A. Kovalev. Modeling heat transfer with boiling on porous structures. *Thermal Engineering*, 12:617–620, 1990.

[26] B.Truong. *Effects of Surface parameters on Boiling Heat Transfer Phenomena.* PhD thesis, Department of Nuclear Science and Engineering, Massachusetts Institute of Technology, 2011.

[27] H. Honda and J.J. Wei. Enhanced boiling heat transfer from electronic components by use of surface microstructures. *Experimental Thermal and Fluid Science*, 28(2):159–169, January 2004.

[28] P.J. Berenson. *On Transition Boiling Heat Transfer from a Horizontal Surface.* PhD thesis, MIT, 1960.

[29] J.P.O'Connor and S.M. You. A painting technique to enhance pool boiling heat transfer in saturated fc-72. *Journal of Heat Transfer*, 117:387–393, May 1995.

[30] M. Toprak B. Palm S. Li, R. Furberg and M.Muhammed. Nature-inspired boiling enhancement by novel nanostructured macroporous surfaces. *Advanced Functional Materials*, 18:2215–2220, 2008.

[31] V. Sathyamurthi H.S. Ahn and D. Banerjee. Pool boiling experiments on a nanostructured surface. *IEEE Transactions on Components and Packaging Technologies*, 32:156–165, 2009.

[32] J. B. Kim H. D. Kim and M. H. Kim. Effect of nanoparticles on chf enhancement in pool boiling of nano-fluids. *Int. J. Heat Mass Transfer*, 49:5070–5074, 2006.

[33] H.D Kim and M.W Kim. Effect of nanoparticle deposition on capillary wicking that influences the critical heat flux in nanofluids. *Applied Ph*, 91:014104, 2007.

[34] R. Jumar H. Moon S. You S. Kwark, G. Moreno. Nanocoating characterization in pool boiling heat transfer of pure water. *International Journal of Heat and Mass Transfer*, 53:4579–4587, 2010.

[35] J. Buongiorno S.J. Kim, I.C. Bang and L.W. Hu. Effects of nanoparticle deposition on surface wettability influencing boiling heat transfer in nanofluids. *Applied Physics Letters*, 89:153107, 2006.

[36] S. H. Kang M.H. Kim. H.S. Ahn, H.J. Jo. Effect of liquid spreading due to nano/microstructures on the critical heat flux during pool boiling. *Applied Physics Letters*, 98:071908, 2010.

[37] H. Qiu D. Attinger A.R. Betz, J. Xu. Do surfaces with mixed hydrophilic and hydrophobic areas enhance pool boiling? *Applied Physics Letters*, 27(141909), 2010.

[38] P. Marty S. Collason H.T. Phan, N. Caney and J. Gavillet. Surface wettability control by nanocoating: The effects on pool boiling heat transfer and nucleation mechanism. *International Journal of Heat and Mass Transfer*, 52:5459–5471, 2009.

[39] M. F. Rubner D. Lee and R. E. Cohen. All-nanoparticle thin-film coatings. *Nano Letters of American Chemical Society*, 6(10):2305–2312, 2006.

[40] R.E. Cohen D.Lee, D.Omolade and M. F. Rubner. ph-dependent structure and properties of tio2/sio2 nanoparticle multilayer thin films. *Chemical Materials, American Chemical Society*, 19:1427–1433, 2007.

[41] Z. Wu R. Cohen M. Rubner J. Bravo, L. Zhai. Transparent superhydrophobic films based on silica nanoparticles. *Langmuir*, 23(13):7293–7298, 2007.

[42] M. F. Rubner D. Lee, Z. Gemici and R. E. Cohen. Multilayers of oppositely charged sio2 nanoparticles: Effect of surface charge on multilayer assembly. *Langmuir,*, 23:8833–8837, 2007.

[43] L. Zhai R.E. Cohen F. Cebeci, Z. Wu and M.F. Rubner. Nanoporosity-driven superhydrophilicity: A means to create multifunctional antifogging coatings. *Langmuir*, 22:2856–862., 2006.

[44] Material saftey data sheet. 1h,1h,2h,2h-perfluorodecyltriethoxysilanefluorosilane. cas 101947-16-4. updated june, 2008.

[45] E. Forrest. *Nanoscale Modification of Key Surface Parameters to Augment Pool Boiling Heat Transfer and Critical Heat Flux in Water and Dielectric Fluids.* PhD thesis, Massachusetts Institute of Technology, 2009.

[46] S. Baunack and A. Zehe. A study uv/ozone cleaning procedure for silicon surfaces. *Phys. sat sol.*, 115:223–227, 1989.

[47] W.E. Wallace K. Efimenko and J. Genzer. Surface modification of sylgard-184 poly(dimethyl siloxane) networks by ultraviolet and ultraviolet/ozone treatment. *Journal of Colloid and Interface Science*, 254:306–315, 2002.

[48] Jelight Company. Uvo cleaner - ozone cleaning device. Online, 2009. Accessed: 25 September 2011.

[49] H.J. Osten and G. Lippert. In situe cleaning of si surfaces by uv/ozone. *Journal of Crystal Growth*, 127:476–478, 1993.

[50] K.J. Lee W.R. Childs, M. J. Motala and R.G. Nuzzo. Masterless soft lithography: Patterning uv/ozone-induced adhesion on poly(dimethylsiloxane) surfaces. *Langmuir*, 21:10096–10105, 2005.

[51] S. Kim J. T. Han and A. Karim. Uvo-tunable superhydrophobic to superhydrophilic wetting transition on biomimetic nanostructured surfaces. *Langmuir*, 23:2608–2614, 2007.

[52] Ullrich Heisig Siegfried Schiller and Siegfried Panzer. *Electron beam technology.* Wiley, 1995.

[53] V. Prabhu I.Fuke and S.Baek. Computational model for predicting coating thickness in electron beam physical vapor deposition. *Journal of Manufacturing Processes*, 7:140–152, 2005.

[54] Donald M. Mattox. *Handbook of Physical Vapor Deposition (PVD) Processing.* Noyes Publications, 1998.

[55] D.G. Braun C. Haynam T. Meier T.M. Anklam, L.V. Berzins and M.A. McClelland. Evaporation rate and composition monitoring of electron beam physical vapor deposition processes. *Surface and Coatings Technology*, 76-77:681–686, 1995.

[56] Micro Chem. *SU-8 2000 Permanent Epoxy Negative Photoresist Professing Guidelines, version 4.* Newton, MA. Available at: www.microchem.com.

[57] *Dektak 150 Surface Profiler User's Manual. P/N 980-294. Revision B. Veeco Instruments Inc. 2009.*

[58] C. Gerardi. *Investigation of the Pool Boiling Heat Transfer Enhancement of Nano-Engineered Fluids by means of High-Speed Infrared Thermography.* PhD thesis, Department of Nuclear Science and Engineering, Massachusetts Institute of Technology, 2009.

[59] *Omega Revised Thermocouple Reference Tables.*

[60] Flir systems. thermovision(r) sc4000/sc6000 user's guide, version 200. september 26, 2007.

[61] J. Genzer and K.Efimenko. Creating long-lived superhydrophobic polymer surfaces through mechanically assembled monolayers. *Science*, 290:2130–2133, 2000.

[62] L.B. Boinovich and A.M. Emelyanenko. Hydrophobic materials and coatings: principles of design, properties and applications. *Russian Chemical Reviews*, 77:583–600, 2008.